EPRI | ELECTRIC POWER RESEARCH INSTITUTE

Benchmarks for Quantifying Fuel Reactivity Depletion Uncertainty—Revision 1

2017 TECHNICAL REPORT

Benchmarks for Quantifying Fuel Reactivity Depletion Uncertainty—Revision 1

All or a portion of the requirements of the EPRI Nuclear Quality Assurance Program apply to this product.

YES  NO

EPRI Project Manager
A. Hakkurt

ELECTRIC POWER RESEARCH INSTITUTE

3420 Hillview Avenue
Palo Alto, CA 94304-1338
USA

PO Box 10412
Palo Alto, CA 94303-0813
USA

800.313.3774
650.855.2121

askepri@epri.com

www.epri.com

3002010613
Final Report, October 2017

DISCLAIMER OF WARRANTIES AND LIMITATION OF LIABILITIES

THE FOLLOWING ORGANIZATIONS, UNDER CONTRACT TO EPRI, PREPARED THIS REPORT:

Massachusetts Institute of Technology (MIT)

Studsvik Scandpower, Inc.

NOTE

For further information about EPRI, call the EPRI Customer Assistance Center at 800.313.3774 or e-mail askepri@epri.com.

Acknowledgments

The following organization, under contract to the Electric Power Research Institute (EPRI), prepared this report:

Massachusetts Institute of Technology (MIT)
77 Massachusetts Ave.
24-221
Cambridge, MA 02139

Principal Investigator
K. Smith

Studsvik Scandpower, Inc.
309 Waverley Oaks Road
Suite 406
Waltham, MA 02452

Principal Investigators
S. Tarves
T. Bahadir
R. Ferrer

This report describes research sponsored by EPRI.

This publication is a corporate document that should be cited in the literature in the following manner:

Benchmarks for Quantifying Fuel Reactivity Depletion Uncertainty—Revision 1.
EPRI, Palo Alto, CA: 2017.
3002010613.

Abstract

Analytical methods, described in this report, are used to systematically determine experimental fuel assembly sub-batch reactivity as a function of burnup. Fuel sub-batch reactivities are inferred using more than 600 in-core pressurized water reactor (PWR) flux maps taken during 44 cycles of operation at the Catawba and McGuire nuclear power plants. The analytical methods systematically search for fuel sub-batch reactivities that minimize differences between measured and computed fission rates, using Studsvik Scandpower's CASMO-5 and SIMULATE-3 reactor analysis tools. More than eight million SIMULATE-3 core calculations are used to reduce one million measured fission rate signals to a set of ~3000 experimental fuel sub-batch reactivities over the range of 0 to 55 gigawatt-days per metric ton (GWd/T) burnup.

Experimental biases derived for the CASMO-5 lattice physics code were used to develop a series of experimental benchmarks that can be used to quantify fuel assembly reactivity decrement biases and uncertainties of other code systems used in spent-fuel pool (SFP) and cask criticality analyses. Specification of eleven experimental lattice benchmarks, covering a range of enrichments, burnable absorber loading, boron concentration, and lattice types are documented in this report.

This report provides a basis for quantification of combined nuclide inventory and cross-section uncertainties in computed reactivity burnup decrements. Final 95/95 tolerance limits for the measured reactivity decrements are shown to be less than 3.05% of the fuel assembly depletion reactivity.

Results support reactivity decrement tolerance limits that are smaller than the 5% assumption that has historically been applied in SFP criticality analysis, and this assumption has now been demonstrated to be both valid and conservative for CASMO-5 based fuel depletion analyses.

Keywords
Cask criticality
Depletion uncertainty
Experimental benchmarks
Nuclear criticality
Reactivity depletion
Spent fuel pool criticality

Deliverable Number: 3002010613

Product Type: Technical Report

Product Title: Benchmarks for Quantifying Fuel Reactivity Depletion Uncertainty—Revision 1

PRIMARY AUDIENCE: Nuclear criticality safety analysts at nuclear power plants and regulators

SECONDARY AUDIENCE: Nuclear criticality safety analysts at research organizations and vendors

KEY RESEARCH QUESTION

What are the magnitudes of the bias and uncertainty in analytical computations of depleted fuel reactivity for burnup credit analysis that arises from depletion during nuclear plant operation? By using the eleven benchmark lattices presented in this report, applicants can provide the technical justification for the biases and uncertainties in depleted fuel reactivity needed in spent fuel criticality licensing applications.

RESEARCH OVERVIEW

Experimentally measured flux map data from forty-four cycles of operation of the Duke Energy Catawba and McGuire plants has been used to infer the hot full power (HFP) bias and uncertainty of CASMO-5 computed lattice depletion reactivity decrements. TSUNAMI module of the SCALE code system has been used to extend the HFP uncertainties to cold spent fuel pool (SFP) rack conditions. The measured depletion reactivity decrements for eleven pressurized water reactor (PWR) benchmark lattices are tabulated and provided to spent fuel criticality analysts so that they can quantify the biases and uncertainties of their specific lattice depletion and criticality analysis computational tools.

KEY FINDINGS

- CASMO-5 HFP reactivity burnup decrement biases are less than 200 pcm over the burnup range from 10 to 60 GWd/T.
- Cold reactivity burnup decrement uncertainties are approximately 350 pcm at 10 GWd/T and 900 pcm at 60 GWd/T.
- Reactivity decrement tolerance limits are smaller than the 5% historical assumption (Kopp Memo) traditionally applied in SFP criticality analysis.
- The 95/95 tolerance limits for the measured reactivity decrements are shown to be less than 3.05% of fuel assembly depletion reactivities.

WHY THIS MATTERS

Use of the eleven benchmark lattices provided in this report provides a more straightforward path to determining the biases and uncertainties in spent fuel depletion analysis. Furthermore, quantification of reactivity decrement biases and uncertainties for spent fuel analysis tools provides technical justification for the validity of the historical Kopp Memo 5% criterion, as this analysis demonstrated that historical Kopp memo recommendation is conservative.

HOW TO APPLY RESULTS

Spent fuel criticality analysts can compute the eleven experimental benchmarks provided in this report and deduce biases and uncertainties for their specific nuclide depletion and criticality analysis codes. These biases and uncertainties can be combined with other uncertainties to establish 95/95 tolerance limits on computed spent fuel criticality eigenvalues for depleted fuel assemblies in their licensing submittals.

LEARNING AND ENGAGEMENT OPPORTUNITIES

- This report, along with companion report (3002010614, Utilization of the EPRI Depletion Benchmarks for Burnup Credit Validation – Revision 1) has been developed for criticality analysts working on burnup credit.
- In addition to these two reports, NEI 12-16, Guidance for Performing Criticality Analyses of Fuel Storage at Light-Water Reactor Power Plants, provides additional resources for complete spent fuel criticality analysis.

EPRI CONTACTS: Hatice Akkurt: Senior Project Manager, Used Fuel and HLW Management Program, hakkurt@epri.com

PROGRAM: Used Fuel and HLW Management Program, Program 41.03.01

IMPLEMENTATION CATEGORY: Reference

Electric Power Research Institute
3420 Hillview Avenue, Palo Alto, California 94304-1338 • PO Box 10412, Palo Alto, California 94303-0813 USA
800.313.3774 • 650.855.2121 • askepri@epri.com • www.epri.com

Acronyms

BOC	Beginning of Cycle
CMS	Core Management System
EFPD	Effective Full Power Days
EOC	End of Cycle
EFPD	Effective Full Power Days
EOFP	End of Full Power
EPRI	Electric Power Research Institute
HFP	Hot Full Power
HZP	Hot Zero Power
IFBA	Integral Fuel Burnable Absorbers
LPB	Lumped Burnable Poisons
NEI	Nuclear Energy Institute
NRC	Nuclear Regulatory Commission
OFA	Optimized Fuel Assembly
OLS	Ordinary Least Square
ORNL	Oak Ridge National Laboratory
PWR	Pressurized Water Reactor
RAI	Request for Additional Information
RFA	Robust Fuel Assembly
SFP	Spent Fuel Pool
WABA	Wet Absorber Burnable Poisons
WLS	Weighted Least Square

Table of Contents

List of Figures

List of Tables

Section 1: Product Description

Methods for treating burnup credit in spent fuel pool criticality analysis commonly made use of the Nuclear Regulatory Commission (NRC) 1998 "Kopp Memo [1]," which allows analysts to use 5% of the computed fuel depletion Δk to compensate for reactivity decrement uncertainties (see Figure 1-1) which might arise from uncertainties in computed nuclide number densities and/or neutron cross sections.

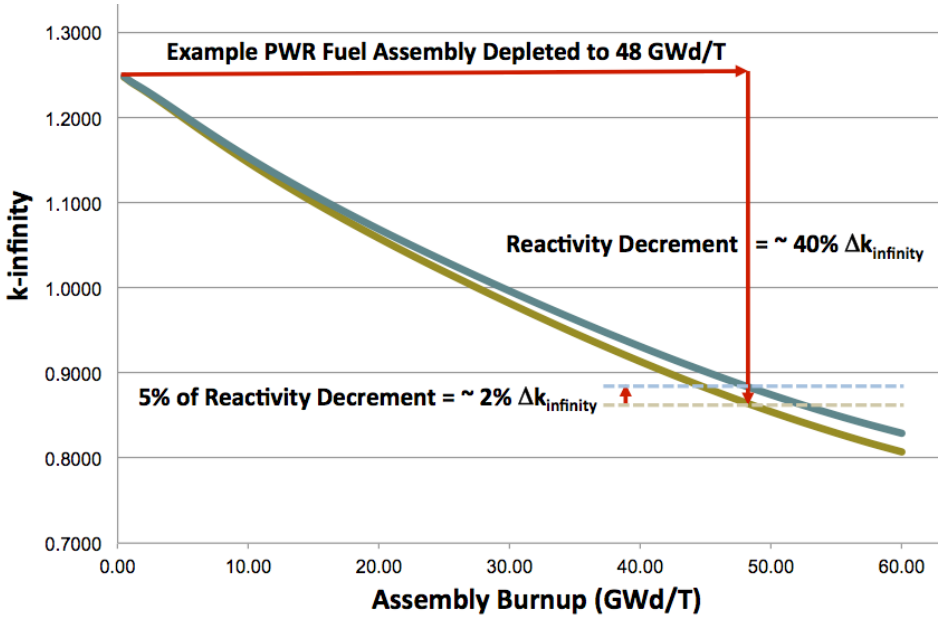

Figure 1-1
Reactivity Decrement Example

The guidance in the "Kopp Memo" provided regulatory clarity and stability for many years. Starting in 2005, regulatory staff positions on acceptable criticality analysis methods evolved through interactions with licensees, and the basis for the guidance in the Kopp Memo was portrayed as being insufficient in light of operational/licensing changes being sought by utilities. In 2010, the NRC requested that applicants supply quantification and/or justification for the 5% reactivity decrement uncertainty assumption.

This report provides experimental quantification of pressurized water reactor (PWR) fuel reactivity burnup decrement biases and uncertainties obtained through extensive analysis of in-core flux map data from operating power

reactors. Analytical methods, described in this report, are used to systematically determine experimental fuel sub-batch reactivities that best match measured fission rate distributions and to evaluate biases and uncertainties of computed lattice physics fuel reactivities.

1.1 Analytical Methods

Forty-four 18-month cycles of flux map data from Duke Energy's Catawba (Units 1 and 2) and McGuire (Units 1 and 2) plants have been analyzed with Studsvik Scandpower's CASMO-5 [2] and SIMULATE-3 [3] reactor analysis codes. By systematically searching for fuel sub-batch reactivities that best match measured fission rate distributions, biases and uncertainties of computed reactivity decrements are experimentally determined. These analyses employ more than 8 million SIMULATE-3 nodal core calculations to extract approximately 3000 measured sub-batch reactivities from flux map data. The individual estimates of the reactivity decrement bias (measured minus calculated reactivity decrement) form a large data set plotted here as a function of sub-batch burnup in Figure 1-2.

Note: positive reactivity decrement bias implies that the calculated reactivity decrement (a negative quantity) is too negative, and the calculated lattice eigenvalue change with depletion is being non-conservatively over-predicted.

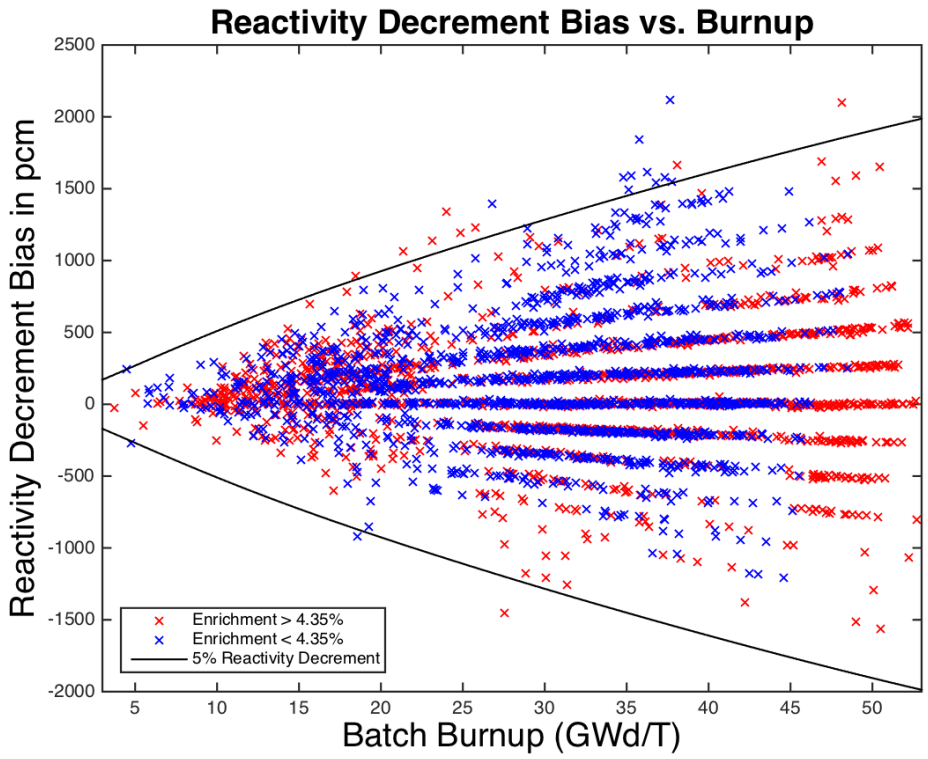

Figure 1-2
CASMO-5 HFP Reactivity Decrement Bias vs. Sub-Batch Burnup

1.2 Summary of Results

Differences between predicted and measured assembly reactivities, illustrated in the preceding figure, are caused by a number of factors: fission rate measurement uncertainties, modeling approximations in the nodal core simulator, uncertainties in fuel burnups, and uncertainties in assembly reactivities as a function of burnup.

The objective of this report is to quantify the latter component of uncertainty – even though scatter in the data is dominated by other components. Regression analysis is used to determine best-estimate biases and tolerance limits of CASMO-5's computed HFP reactivity decrements, and it is shown that biases are less than 200 pcm and uncertainties are approximately 800 pcm at 60 GWd/T, as summarized in Table 1-1.

Table 1-1
Measured CASMO-5 ***HFP*** *Reactivity Decrement Biases and Tolerance Limits*

Burnup (GWd/T)	**10.0**	**20.0**	**30.0**	**40.0**	**50.0**	**60.0**
CASMO-5 Bias (pcm)	66	101	106	80	22	-64
95/95 Tolerance Limit (pcm)	207	386	537	655	745	803

Analysis demonstrates that the bias and uncertainties are independent (within experimental uncertainties) of fuel assembly design, core boron concentration, and cycle burnup.

Analysis with TSUNAMI module of SCALE code system [4], developed by Oak Ridge National Laboratory (ORNL), is used to extend HFP results to cold conditions. It is shown that extremely high correlation of reactivities between hot and cold conditions results in additional uncertainties from HFP to cold conditions, and final biases and tolerance limits are summarized in Table 1-2 in units of pcm and percentage of depletion reactivity.

Table 1-2
Measured CASMO-5 ***Cold*** *Reactivity Decrement Biases and Tolerance Limits*

Burnup (GWd/T)	**10.0**	**20.0**	**30.0**	**40.0**	**50.0**	**60.0**
CASMO-5 Bias (pcm)	66	101	106	80	22	-64
95/95 Tolerance Limit (pcm)	348	537	654	752	831	888
CASMO-5 Bias (% of depletion reactivity)	0.58	0.50	0.38	0.23	0.05	-0.13
95/95 Tolerance Limit (% of depletion reactivity)	3.05	2.66	2.33	2.12	1.95	1.81

1.3 Experimental Benchmarks

The experimental biases derived for the CASMO-5 lattice reactivities are used to develop a series of experimental benchmarks that can be used to quantify reactivity decrement biases and uncertainties for other code systems used in lattice depletion and criticality analysis. Specification of eleven experimental

lattice benchmarks, covering a range of enrichments, burnable absorber loading, boron concentration, and lattice types are documented in this report.

Results demonstrate that experimental benchmarks are not sensitive to the cross-section library or code version used to reduce the experimental data.

Interested parties can use these experimental benchmarks and their analysis tools to generate reactivity decrement biases and tolerance limits that are specific to those tools.

1.4 Summary of Conclusions

Results presented in this report provide quantification of combined nuclide inventory and cross-section uncertainties in reactivity burnup decrement which support a smaller reactivity decrement uncertainty than the 5% criterion often used in historical SFP analysis. The data presented in this report demonstrate that the 95/95 tolerance limit on CASMO-5 depletion reactivity decrements is less than 3.05% of depletion reactivity.

Experimental reactivity decrement biases derived from flux map data are also shown to be similar to those derived from changes in biases of reactor soluble boron concentration from beginning (BOC) to end of cycle (EOC).

1.5 Significant Changes from Previous (Rev 0) Document

This report contains many significant changes from the initial EPRI report [5] published in 2011. The previous analysis was also published in Reference [6]. Changes address issues raised in both NRC request for additional information (RAIs) and face-to-face meetings, and the most significant changes are:

- Using weighted least square (WLS) regression models with weights to treat the reactivity decrement heteroscedasticity in both burnup and measurement sensitivity.
- Collapsing burnup decrement bias data to one point per sub-batch/cycle, to eliminate the correlation effects between successive flux map data points within each cycle of operation.
- Eliminating all post-minimization screening of sensitivity and cycle burnup data points that had been previously used to eliminate some low sensitivity data.
- Determining 95/95 tolerance limits of measured reactivity decrements by using statistical methods to replace the “perturbed library” engineering approach that was previously used.
- Using 1-sided 95/95 tolerance limits (and normality testing) to replace the 2-sigma uncertainties of the original report.
- Replacing **burnup-independent** uncertainties with **burnup-dependent** tolerance limits, to more appropriately model the increasing uncertainty of measured burnup decrements with sub-batch burnups.

Section 2: Introduction

2.1 Background

Criticality analysis of spent fuel pools and casks is performed using large-scale Monte Carlo or multi-group transport eigenvalue calculations for various loadings of spent fuel racks. These calculations have two fundamental sources of uncertainty: the nuclide inventory of the fuel assemblies, and neutron cross-section data. For racks loaded with fresh fuel, these uncertainties can be quantified directly by making extensive comparisons of calculations with the many cold critical measurements that have been performed in rack geometries. Such analyses provide quantification of calculational uncertainties as a function of fuel assembly design, fuel pin enrichments, rack geometries, coolant temperature, coolant boron concentration, etc. Such uncertainties include contributions from: the nuclide inventory of the fuel assemblies, basic neutron cross-section data, and analytical methods.

Since experimental criticals do not exist for depleted fuel assemblies, storage rack criticals provide no quantification of uncertainties arising from changes in nuclide concentrations and/or uncertainties in cross-section data for nuclides produced by depletion (for example, production of transuranic nuclides and fission products). The difficulty and expense of performing depleted fuel criticals makes it clear that such data will not be available in the near future – so direct quantification of depletion uncertainties is not easily achieved.

The application of burnup credit in spent fuel pool and cask criticality analysis involves defining a large sequence of conservative calculations that cover all anticipated loadings and uncertainties in those analyses. Conservative assumptions and/or uncertainties are applied to compensate for lack of complete knowledge, for quantities such as: maximum fuel temperature, maximum moderator temperature, uncertainty in soluble boron concentration, maximum burnable absorber usage, most limiting axial burnup distribution, maximum error in the declared burnup. This report provides data that can be used for validation of lattice physics code predictions of commercial spent nuclear fuel nuclide concentrations and assembly burnup reactivities that include the uncertainties of fundamental nuclear cross sections.

2.2 Historical Approaches

In order to compensate for the lack of depleted criticals, current methods for treating burnup credit in spent fuel pool criticality analysis often made use of the NRC 1998 "Kopp Memo [1]," which allowed analysts to use 5% of the fuel depletion Δk (computed using criticality tools) to compensate for reactivity decrement uncertainties which might arise from uncertainties in computed nuclide number densities and/or neutron cross sections. The guidance in the "Kopp Memo" provided regulatory clarity and stability for many years. Starting in 2005, regulatory staff positions on acceptable criticality analysis methods evolved through interactions with licensees, and the basis for the guidance in the Kopp Memo was portrayed as being insufficient in light of operational/licensing changes being sought by utilities. In 2010, the NRC requested applicants to supply quantification and/or justification for the historical 5% uncertainty assumption.

Figure 2-1 displays a CASMO-5 k-infinity curve versus burnup computed for a typical 17x17 fuel assembly without burnable absorbers. By comparing the computed k-infinity at any burnup with k-infinity at zero burnup, the computed reactivity decrement can be evaluated. In this figure, at a burnup of about 48 GWd/T, the reactivity decrement is about -40% delta-k. The Kopp Memo instructs one to assume that the reactivity decrement is only 95% of the computed reactivity decrement, which in this example, is equivalent to assuming that the fuel is approximately 2% Δk more reactive than computed.

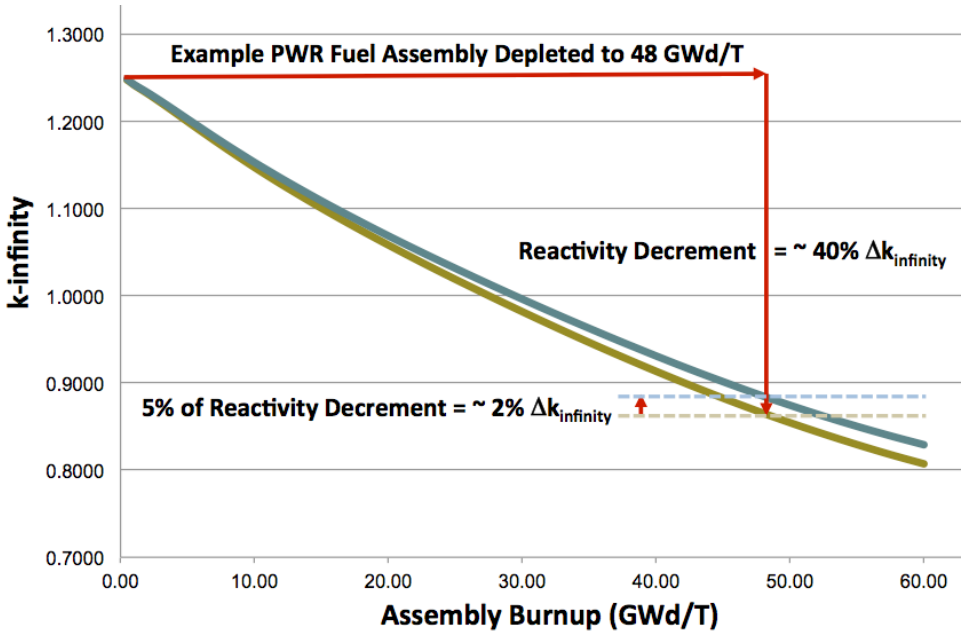

Figure 2-1
CASMO-5 Reactivity Decrement

For cask criticality analysis, chemical assays have been used to validate the isotopic content, and MOX and UO_2 critical experiments have been used to validate actinide worths. Various approaches have been used for validating fission product worths. The approach presented in this report simplifies the current approach for burnup credit by simultaneously addressing nuclide inventory and nuclide reactivity biases.

2.3 Project Outline

The remainder of this document details a direct approach to quantifying fuel depletion uncertainties by using operational reactor data and corresponding reactor analysis tools. Comparisons of computed fuel depletion effects and measured core depletion effects are available from every operating reactor on a near continuous basis. One way of viewing reactor data is that they provide a great many instances of the "depleted fuel criticals" that we desire. These power reactor configurations include:

- many assembly lattice types
- many burnable absorber types
- a spectrum of assembly burnups
- impacts of numerous minor fuel depletion effects, including:
  - fuel stack elongation
  - fuel pellet cracking
  - fuel pellet swelling
  - cladding corrosion/crud buildup
  - fuel rod bowing

Challenges in using measured reactor data and computed reactor models to quantify the uncertainty in reactivity decrements arise because of the need to:

- Extract uncertainties for each fuel assembly enrichment/absorber type in cores containing many different fuel types.
- Determine the burnup dependence of assembly reactivity decrement biases and uncertainties.
- Account for differences in assembly reactivity uncertainties at hot operating conditions (~900K fuel temperature, ~550K coolant temperature) and the cold conditions that normally exist in spent fuel pools and casks.

The next section of this report provides an overview of the procedure used to experimentally quantify fuel reactivity decrement uncertainties. Subsequent sections provide:

- Specific details of the implementation of this procedure.
- An application of this analysis procedure to 44 cycles of measured reactor data from four Duke Energy PWRs.

- Documentation of derived biases and tolerance limits in CASMO-5 reactivity burnup decrements.
- A set of experimental benchmarks that can be used to quantify reactivity burnup decrement biases and uncertainties for any lattice physics code/criticality analysis tool.

Section 3: Summary of Analysis Approach

3.1 Overview

In-core flux maps taken as a routine part of PWR operation (usually every 30 days) provide measured data that can be used to quantify the accuracy of computed assembly "power distributions." This data are routinely used to determine 95/95 confidence intervals on predicted assembly and pin power distributions needed for NRC licensing of core designs.

The analytical methods employed in this project use the same measured flux map data and core analysis tools to deduce errors in assembly reactivities at each flux map and to determine the assembly depletion decrement bias and uncertainty. In order to use power reactor data to develop depletion decrement biases and uncertainties for each type of fuel assembly (for example, lattice pitch, fuel enrichment, burnable absorber type), one needs to separate the reactivity contributions of each fuel type in the core. Section 3 of this report outlines the analytical procedures used to determine depletion decrement biases and uncertainties, and Section 6 provides in-depth details of the procedure - as it has been implemented.

3.2 Flux Map Measurements

At each flux map measurement, several (usually 5 or 6) traversing ^{235}U fission chambers are passed axially through instrumentation tubes at the center of approximately 50 instrumented fuel assemblies. By collecting detector signals from all fission chambers as they are passed through a common instrument tube, an inter-calibration of the detector signals is performed and all 50 measured signals are re-normalized to provide a measured 3D spatial distribution of fission rates throughout the reactor core. The fission rates are typically integrated axially into 61 discrete intervals (~6 cm), which are later collapsed to correspond to the 24 axial nodes (~15 cm) that are typically used in reactor analysis models. This type of measurement is performed routinely, and measured fission rate distributions are used to monitor technical specification compliance of core power distributions.

3.3 Relationship of Flux Map Errors to Fuel Reactivity

The concept of using flux maps to deduce errors in sub-batch fuel reactivities is motivated by the fact that the distribution of fission rates errors is sensitive to errors in the burnup dependence of computed fuel reactivity. If analysis models have errors in fuel reactivity that are independent of the fuel depletion, the spatial

shape of flux map errors would not be sensitive to errors in fuel reactivity. Such space-independent errors would be similar to those observed when the boron concentration is altered in a computational model – the reactivity change is nearly the same at all core locations, and differences between computed and measured fission rates are very insensitive to errors in boron concentration.

However, errors in fuel reactivity arising from imperfect predictions of nuclide concentrations or errors in neutron cross-section data will necessarily change (usually increase) with assembly burnup. Since reactors are loaded with fuel having a large range of burnups, any depletion-induced errors in fuel reactivity will necessarily have a spatial dependence across the reactor core. Consequently, the accuracy of computed fission rate distributions is sensitive to the spatial distribution of these reactivity errors. This core characteristic makes it possible to deduce the magnitude of errors in reactivity of each fuel sub-batch by determining the spatial distribution of fuel reactivities that produces the best agreement with measured fission rate distributions.

3.4 Flux Map Perturbation Calculations

The analysis technique employed here uses the SIMULATE-3 reactor analysis nodal code to perform a series of exact perturbation calculations to minimize the global root-mean-square deviation between measured and computed detector signals for each fuel sub-batch (assembly type, enrichment, and burnable absorber configuration, and burnup batch) in the reactor core. In this approach, sub-batch reactivity is altered by re-evaluating all nuclear lattice parameters (cross sections, discontinuity factors, detector response functions, etc.) at a new sub-batch nodal burnup. The computed sub-batch nodal burnup, which is used as the interpolant in the nuclear data library, is systematically altered by a factor, M_B. The spatial distribution of fission rates is very sensitive to the fuel sub-batch reactivity, as is depicted in Figure 3-1 for three values of the sub-batch burnup multiplier (0.90, 1.0 and 1.10) applied to the highlighted assemblies. From this figure, it can be seen that the root mean square (r.m.s.) difference between calculated and measured radial fission rates (at the instrumented locations) are 4.2, 1.2, and 3.3%, for these cases. Individual assembly fission rates are more sensitive, with differences as large as 8.4% being observed for M_B =0.9.

	R	P	N	M	L	K	J	H	G	F	E	D	C	B	A
1							-0.005 0.008 0.020			-0.023 0.000 0.022					
2			-0.046 -0.020 0.006			-0.045 -0.006 0.032		0.012 0.004 -0.003							
3								0.032 0.020 0.007		-0.017 0.012 0.039		-0.042 0.012 0.064		-0.039 -0.012 0.013	
4		-0.056 -0.017 0.020	-0.051 0.003 0.055					0.061 -0.008 -0.062							
5					0.032 0.010 -0.010				0.069 -0.001 -0.066		0.027 0.005 -0.015		-0.042 0.007 0.055		
6	-0.013 0.004 0.026		-0.018 0.011 0.038			0.038 -0.001 -0.040									
7				0.039 0.011 -0.014			0.031 -0.011 -0.053			0.064 0.011 -0.039			-0.011 -0.004 0.002		
8	-0.008 -0.003 0.001		0.025 0.013 0.001		0.080 0.008 -0.059		0.042 0.002 -0.037					0.057 -0.002 -0.056	0.029 0.017 0.005	0.009 0.001 -0.007	
9		-0.009 0.007 0.022							0.048 0.006 -0.036		0.084 0.014 -0.051				-0.017 -0.004 0.009
10												-0.005 -0.002 0.001			
11	-0.039 -0.018 0.003				0.005 -0.017 -0.037			0.092 0.020 -0.047			0.026 0.004 -0.016				-0.036 -0.015 0.005
12						-0.015 -0.012 -0.009			0.037 0.009 -0.016			-0.048 -0.003 0.040			
13			-0.057 0.000 0.054		-0.068 -0.018 0.029			0.025 0.013 0.001						-0.041 -0.014 0.011	
14			-0.052 -0.026 0.000				0.002 0.018 0.033			-0.036 0.003 0.041		-0.070 -0.031 0.006			
15					-0.033 -0.012 0.008			-0.005 -0.001 0.003						r.m.s. diff M_B=0.9 4.2% M_B=1.0 1.2% M_B=1.1 3.3%	

Figure 3-1
Computed Fission Rate Errors With 3 Sub-batch Burnup Multipliers Applied to One Sub-batch (yellow boxes)

The reason for choosing a sub-batch burnup multiplier is that if there are errors in reactivity predictions of the lattice depletion code, the errors would be seen by all assemblies in the sub-batch. For example, if fission rates predicted in all assemblies of a sub-batch were either consistently low or consistently high, this would be a strong indication of lattice code depletion errors (e.g., nuclide concentration errors, cross-section data errors, resonance modeling approximations, approximations in solving neutron transport equations, approximations in solving the nuclide depletion equations, approximations in modeling of boron history, etc.) The data often show, however, that fission rate differences vary in both sign and magnitude within a sub-batch. This indicates that most of the differences in fission rates are due to factors not directly related to errors in reactivity predictions with burnup.

3.5 Measured Sub-batch Reactivity Errors

If the sub-batch burnup multiplier M_B is driven through a range of values, one can determine the value of M_B that minimizes the r.m.s. deviation between measured and computed detector signals, as depicted in Figure 3-2. One can see that the set of M_B values creates a smooth function, the minimum of which is the burnup multiplier (M_{min}) that leads to the most accurate prediction of radial fission rates for this flux map. In this example, the M_B value of ~1.01 produces the most accurate prediction of fission rates. SIMULATE-3 edits of batch k-infinities for each value of M_B are then used to construct an **estimate of the reactivity error [defined as k-infinity (M_B=M_{min}) minus k-infinity (M_B=1.0)]** for this fuel sub-batch at its sub-batch burnup.

By applying this procedure to many cycles of flux maps, one can estimate the reactivity error for each sub-batch as a function of burnup. Figure 3-3 displays plots of the r.m.s. differences between measured and computed fission rates (on the left axis) vs. computed batch burnup x M_B, for one sub-batch of fuel as it progresses through three successive cycles of reactor operation. The values of M_{min} are also plotted as symbols (on the right axis). By measuring sub-batch reactivity errors for every flux map in every reactor cycle, one can construct estimates of the error in sub-batch reactivity and the corresponding shapes of sub-batch reactivity error vs. sub-batch burnup. Note that the burnup multiplier has been plotted against the computed sub-batch-averaged burnup (not including the multiplier), so the minimum points for the two sets of data are slightly misaligned.

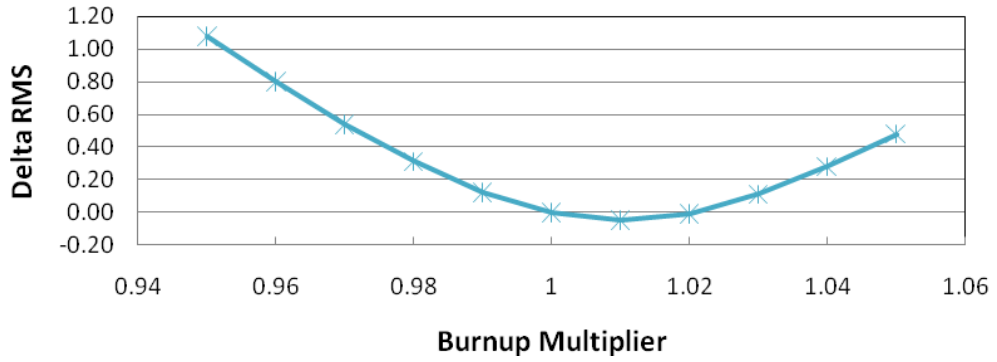

Figure 3-2
Change in r.ms. Fission Rate Error vs. Sub-batch Multiplier

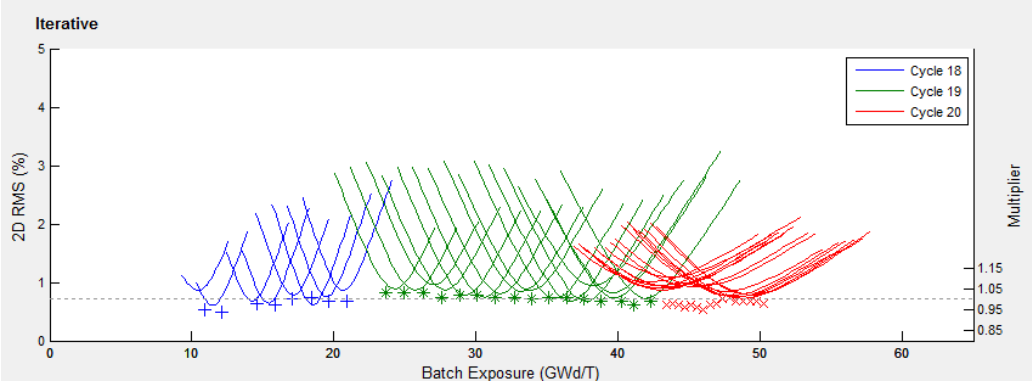

Figure 3-3
Determination of Sub-batch Burnup Multiplier as a Function of Burnup

3.6 Simultaneous Determination of All Sub-batches Reactivities

At any one time, the reactor core contains many sub-batches of fuel (typically 10 to 15), and it is important that M_{min} be determined simultaneously for all sub-batches such that the global r.m.s. differences between computed and measured fission rates are minimized. This is achieved by performing a local search in a succession of passes over all sub-batches to determine the local minimum. The plots in Figure 3-4 show the minimized r.m.s fission rate differences and optimal values of M_{min} for one sub-batch between the zero pass (upper plot) and final iterative pass (lower plot). Several things can be observed from these plots:

1. for high sensitivity cases (e.g., end of cycle 16 and all of cycle 17), the iterative results are not very sensitive to the iteration,

2. for cases with low sensitivities to the sub-batch burnup multiplier, the zero pass results (independent perturbations of each sub-batch in the core) can be far from the converged results, and

3. the iteratively converged results display more consistent burnup trends than zero pass results. Thus, the iterative approach is preferable to the non-iterative approach.

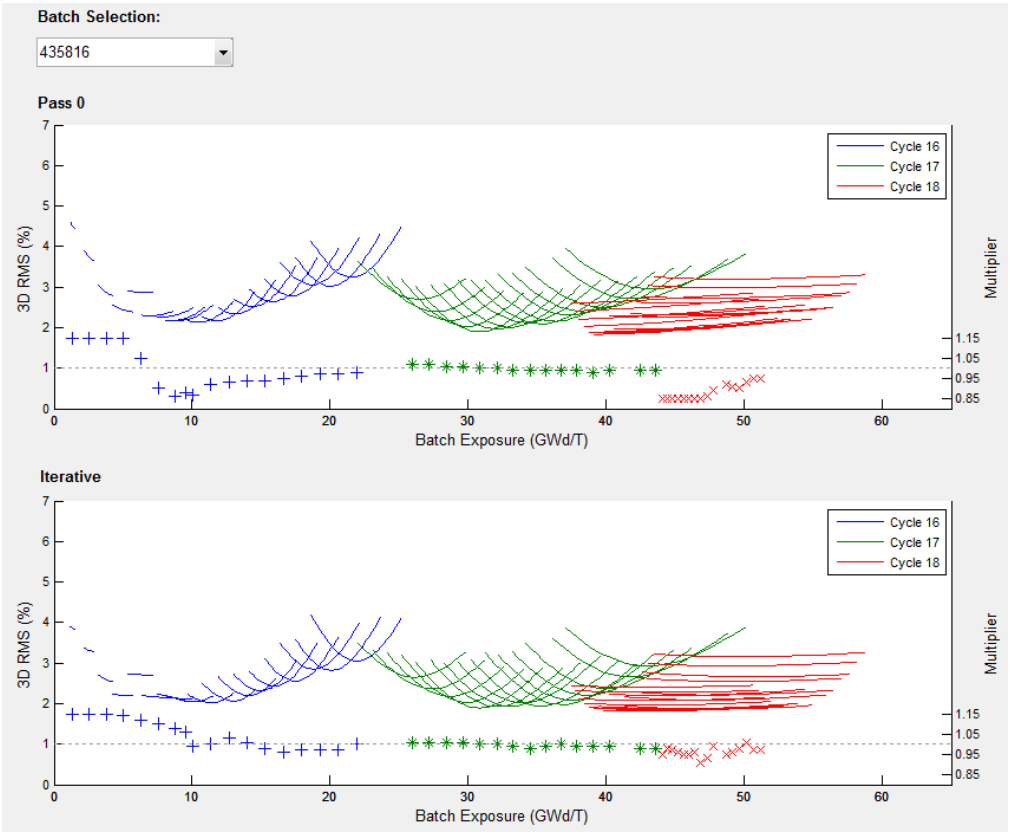

Figure 3-4
Nodal (3D) r.m.s. Differences for One Sub-batch

Note that if sub-batch multipliers could reduce the r.m.s. to zero, then it could be argued that each sub-batch assembly is experiencing the same discrepancy, which would be indicative of depletion errors. The data, however, shows that although r.m.s. differences are reduced with sub-batch multipliers, the reduction is a small fraction of the total deviation, and therefore, residual deviations must be caused by factors other than sub-batch reactivity (and hence are not indicative of depletion errors).

One normally considers the core radial fission distribution to be more sensitive to batch reactivities than the axial shape, which would lead one to conclude it might be preferable to minimize the radial (2D) r.m.s deviations rather than the nodal (3D) r.m.s deviation. Figure 3-5 displays plots of the radial r.m.s. deviations (both searches were performed to minimize the 3D differences), and one can observe that there is little difference between the minimum points of the 2D r.m.s. values and the 3D r.m.s. values of Figure 3-4. However, 2D r.m.s differences are more sensitive (i.e., display bigger changes) to the burnup multipliers.

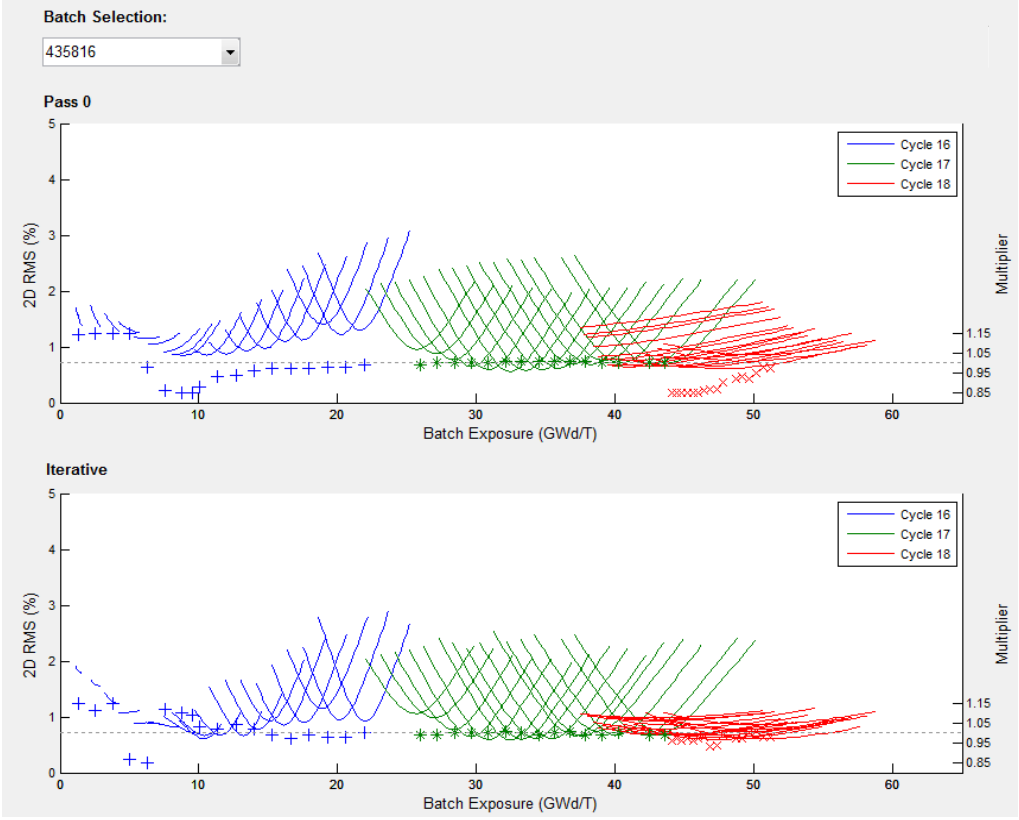

Figure 3-5
Radial (2D) r.m.s. Differences for One Sub-batch

Section 5 provides a detailed description of the final algorithm implemented to solve the many sub-batch minimizations. It should be noted that this method of determining errors in computed assembly reactivities from flux map data has one unique characteristic – **this analytical method is completely independent of errors in core-wide reactivity predictions (for example, k-eff, critical boron, etc.).** Thus, the proposed analysis method is completely complementary to reactivity-based methods normally used for quantifying errors in computational models (for example, critical assembly analysis, reactor startup criticals, shutdown margin measurements, and boron letdown comparisons).

Section 4: Analysis Codes: Studsvik CMS

The Studsvik Core Management System (CMS) is routinely used to perform the neutronic and thermal-hydraulic analysis needed for design, optimization, and safety analysis of nuclear reactor cores. While the CMS suite of codes is capable of performing steady-state and transient (dynamic) analysis of reactor cores, the methods described in this document are restricted to the CMS codes needed to perform steady-state and pseudo steady-state core analysis.

4.1 Code System Overview

The CMS code system consists of five separate codes that are used as a package to perform reactor core analysis. The five codes are:

- **INTERPIN-4** [7] for analyzing the 1-D fuel temperatures for an individual fuel pin, as a function of:
- Fuel pin design (e.g., enrichment, gas pressurization, etc.)
- Linear heat loading
- Fuel burnup
- **CASMO-5** [2, 8] for analyzing the 2-D neutronic behavior of an individual fuel assembly, as a function of:
- Lattice design (e.g., pin enrichment layout, burnable absorber design, etc.)
- Local conditions (e.g., fuel temperature, coolant density, boron content, etc.)
- Fuel burnup
- Control rod insertion
- **CMSLINK** [9] for generating a library of tabularized CASMO-5 data for a collection of fuel assemblies and reflector types, as a function of:
- Fuel burnup
- Thermal hydraulic conditions
- Control rod insertion
- Fuel history effects
- **SIMULATE-3** [3, 10-19] for analyzing the detailed 3-D reactor core neutronic and thermal hydraulic behavior over the reactor core lifetime, as a function of:
- Reactor power

- Coolant flow rate and inlet temperature
- Fuel burnup
- Control bank insertion

INTERPIN-4 and CMSLINK are often considered as auxiliary codes in the CMS suite. On the other hand, CASMO-5 and SIMULATE-3 are very large (many hundreds of thousands of lines of FORTRAN) codes that perform the bulk of the physics modeling in CMS. Appendix A details the physics models and methods of these codes that are important for understanding how CASMO-5 and SIMULATE-3 are used for this project.

Section 5: Duke Energy's Reactor Models

5.1 Overview

Data from four of Duke Energy's PWR units [20] have been used to determine measured fuel burnup reactivity decrement biases and uncertainties. All units are 4-loop Westinghouse reactors containing 17x17 fuel assemblies. Duke Energy provided complete specifications for the reactor, the fuel, and operational data so that CASMO-5/SIMULATE models could be independently constructed for this project. Detailed flux map data for all cycles of operation were included in the data package, thus enabling application of the previously outlined reactivity decrement methodology. Reactor cycle parameters are summarized in Table 5-1.

Table 5-1
Reactor and Fuel Data

Unit	Cycles	Cycle Length (EFPD)	Enrichment Range (%)	HZP Boron (ppm)	Maximum LBP #	Maximum IFBA #	Maximum WABA+IFBA #
McGuire-1	10 to 21	363–514	3.40–4.95	1576–2000	24	128	24 + 128
McGuire-2	10 to 20	429–518	3.64–4.90	1690–2037	24	128	24 + 128
Catawba-1	9 to 19	407–522	3.45–4.75	1501–2104	24	128	16 + 128
Catawba-2	8 to 17	451–527	3.50–4.90	1819–2109	24	128	20 + 128

5.2 Fuel Types

The fuel assemblies loaded into the Duke reactors for these cycles were of two distinct mechanical types: Areva's MarkBW with lumped burnable poisons (LBPs) and Westinghouse's robust fuel assembly (RFA) fuel with wet annular burnable absorbers (WABAs) and/or integral fuel burnable absorbers (IFBAs). The MarkBW fuels used a range of LBP enrichment spanning from 1% to 4% by weight B_4C. As the reactors moved to 18-month cycles, the core loadings became more complex with the introduction of split enrichment feeds and many different burnable poison combinations. As evident from the fuel descriptions presented in Table 5-2, each cycle contains feed fuel divided into 5 to 12 sub-batches (for example, different combinations of enrichment and/or burnable absorbers). The number of fuel assembly types exceeds 100 for the analyzed cycles of each of the four units.

Table 5-2
Feed Fuel Characteristics

Cycle	Enrichment (%)	# of sub batches	Cycle	Enrichment (%)	# of sub batches
McGuire-1			**McGuire-2**		
10	3.40	4	10	3.85 / 3.95	7
11	3.40 / 3.55	9	11	3.90 / 4.15	7
12	3.67	9	12	3.78	6
13	3.92	8	13	4.09 / 4.39	11
14	4.14 / 4.50	7	14	3.77 / 4.33	7
15	4.40 / 4.75	6	15	4.16 / 4.56	12
16	3.92 / 4.35	7	16	4.37 / 4.67	8
17	4.45 / 4.74	9	17	4.35 / 4.75	8
18	4.01 / 4.64	5	18	4.05 / 4.70	6
19	4.00 / 4.68	7	19	3.90 / 4.80	8
20	4.00 / 4.85	9	20	3.65 / 4.90	9
21	3.60 / 4.95	10			
Catawba-1			**Catawba-2**		
9	3.86	8	8	3.98	6
10	3.65 – 3.92	6	9	4.32 / 4.42	9
11	4.02	6	10	4.54	5
12	4.50	6	11	3.90 / 4.20	6
13	3.81 / 4.31	6	12	4.35 / 4.66	8
14	4.19 / 4.46	9	13	4.00 / 4.75	8
15	4.18 / 4.53	10	14	4.45 /4.75	8
16	4.42 / 4.67	10	15	3.80 / 4.73	11
17	3.88 / 4.51	9	16	4.38 / 4.90	8
18	4.05 / 4.51	8	17	3.80 / 4.82	9
19	3.96 / 4.75	7			

CASMO-5 lattice calculations were performed for each unique axial layer (for example, burnable poison zone, cutback burnable poison zone, axial blanket, etc.) of each fuel type. Complete CASMO-5 PWR case matrices of data were generated spanning the full range of hot to cold reactor conditions with burnups up to 80 GWd/T. Depletion histories were performed for boron, moderator temperature, and fuel temperature so that the effects from variable reactor boron concentrations and local power density could be modeled directly in SIMULATE-3.

CASMO-5 reflector cases (for lower, upper, radial with baffle, and radial with both baffle and barrel) were executed to generate equivalent reflector data as a function of moderator temperature and boron concentration for use in SIMULATE-3 reflector nodes.

5.3 CMS Code Versions

The analysis in this project used the following QA production code versions for all cycle depletion analysis:

- INTERPIN-4 Version 4.01
- CASMO-5 Version 2.00.00
- CMSLINK Version 1.27.00
- SIMULATE-3 Version 6.09.22_PWR_1

A special branch version of SIMULATE-3 was created to perform the automated perturbation cases described in Section 6. That version is designated:

- SIMULATE-3 Version 6.09.22_EPRI

5.4 Core Follow Summary Results

SIMULATE-3 core follow calculations were performed for each reactor cycle, using the core loading patterns and the operational reactor history. The as-measured core power, core coolant flow, coolant inlet temperature, and control rod positions were used as boundary conditions for the SIMULATE-3 calculations, and a boron search to critical was performed at each depletion step. The SIMULATE-3 model used a four-node-per-assembly radial nodalization, 24 axial nodes over the active fuel height (356.76 cm), and one homogenized reflector node at the top and at the bottom of the fuel stack. Each cycle was divided into fine depletion steps (30-100 depletion points per cycle) so fluctuations in reactor conditions faithfully followed the history of reactor operations.

The accuracy of SIMULATE-3 depletion calculations was checked by comparing computed and measured boron concentrations at points where measured plant chemistry boron data and measured ^{10}B isotopic data were available. A typical comparison between plant boron data (corrected to natural ^{10}B /^{11}B ratio) and computed SIMULATE-3 critical boron concentrations are displayed in Figure 5-1. From the data in this figure, it can be observed that the

gross core reactivity is well predicted, including the early-cycle burnout of the strongly self-shielded burnable poisons.

Comparisons of calculated and measured hot zero power (HZP) critical boron concentrations, as well as beginning of cycle (BOC) ~25 effective full power days (EFPD) and end of cycle (EOC), extrapolated to zero ppm boron concentrations, are summarized for all four units in Tables 5-3 to 5-6. Of particular interest are any trends from BOC to EOC in the mean differences of calculated and measured boron, which can be seen to be less than 26 ppm for all four units.

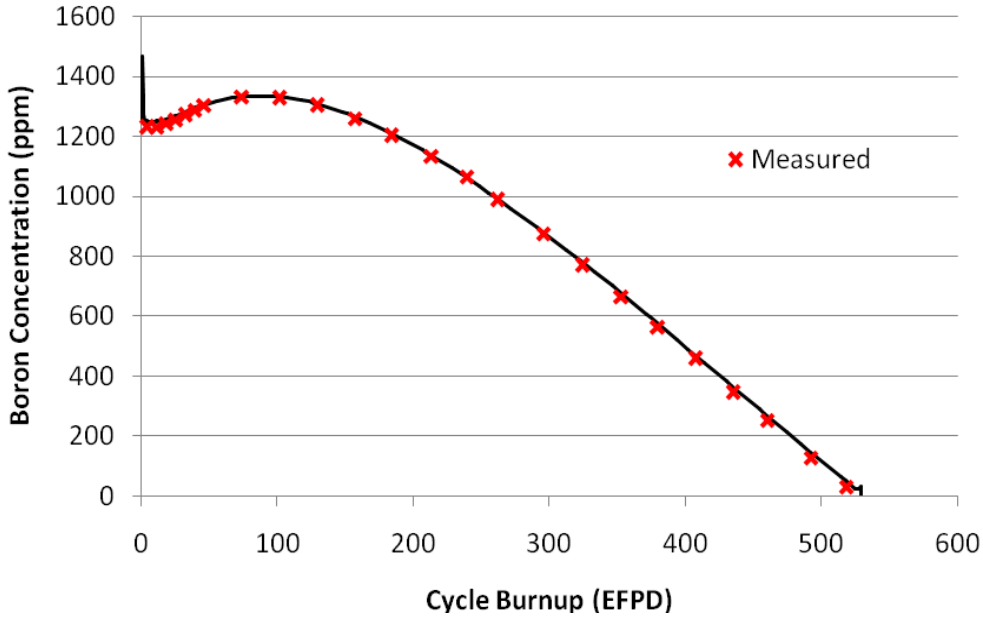

Figure 5-1
Comparison of SIMULATE and Measured Boron

Table 5-3
McGuire Unit-1 Boron Comparisons

Cycle	Cycle Length at end of HFP, 0 ppm = EOC	Measured Boron (ppm)			Calculated – Measured Boron (ppm)		
		HZP BOC	HFP		HZP BOC	HFP	
			BOC	EOFP		BOC	EOC
10	383.4	---	1142	86	---	12	-28
11	363.2	1746	1107	45	27	8	-22
12	380.0	1803	1150	154	28	5	-24
13	442.5	2000	1328	50	19	-6	-26
14	465.5	1955	1252	59	5	4	-36
15	492.7	1576	906	49	9	-9	-24
16	501.9	1920	1299	91	10	-4	-22
17	514.0	1975	1337	135	-3	-10	-37
18	505.0	1973	1331	109	-4	-7	-28
19	487.5	1899	1279	149	-2	-25	-35
20	478.2	1942	1267	93	8	-6	-52
21	---	1840	1161	---	12	-7	---
				Average	10	-4	-30

Table 5-4
McGuire Unit-2 Boron Comparisons

Cycle	Cycle Length at end of HFP, 0 ppm = EOC	Measured Boron (ppm)			Calculated – Measured Boron (ppm)		
		HZP BOC	HFP		HZP BOC	HFP	
			BOC	EOFP		BOC	EOC
10	431.8	1839	1177	13	20	-2	-41
11	429.0	1906	1248	106	13	-17	-17
12	423.9	2037	1359	41	26	3	-11
13	446.2	1896	1189	15	-10	-30	-35
14	486.4	1691	1090	141	18	-13	-35
15	517.8	1919	1301	25	13	-1	-38
16	502.6	1887	1241	26	-13	-19	-33
17	511.9	1908	1238	114	2	-14	-34
18	494.8	1818	1146	158	26	6	-44
19	475.8	1817	1117	4	23	2	-30
20	---	1713	1035	---	5	-23	---
				Average	11	-10	-32

Table 5-5
Catawba Unit-1 Boron Comparisons

Cycle	Cycle Length at end of HFP, 0 ppm = EOC	Measured Boron (ppm)			Calculated – Measured Boron (ppm)		
		HZP BOC	HFP		HZP BOC	HFP	
			BOC	EOFP		BOC	EOC
9	421.1	1876	1214	43	27	-1	2
10	407.6	1840	1173	82	37	14	-8
11	445.4	1983	1267	116	44	18	0
12	486.8	2012	1275	28	32	3	-3
13	491.2	1501	871	17	35	7	8
14	515.7	1899	1285	82	44	17	15
15	500.9	1888	1246	157	18	12	9
16	521.8	2104	1371	112	21	9	4
17	505.7	2097	1402	131	51	34	12
18	482.6	2011	1341	10	45	25	8
19	---	1920	1241	---	24	2	---
				Average	34	13	5

Table 5-6
Catawba Unit-2 Boron Comparisons

Cycle	Cycle Length at end of HFP, 0 ppm = EOC	Measured Boron (ppm)			Calculated – Measured Boron (ppm)		
		HZP BOC	HFP		HZP BOC	HFP	
			BOC	EOFP		BOC	EOC
8	451.5	1869	1186	69	46	35	12
9	472.0	2082	1352	49	38	30	9
10	490.9	1906	1164	222	64	37	4
11	495.6	1797	1153	15	44	32	20
12	483.1	1781	1153	49	51	27	16
13	527.3	1889	1256	30	32	18	22
14	501.2	1871	1195	103	30	20	16
15	498.5	1967	1253	58	52	43	16
16	464.4	1828	1106	42	37	27	15
17	499.0	1750	1054	---	35	25	9
				Average	43	30	14

5.5 Flux Map Summary Results

Measured flux map data for each unit was taken at intervals of about 30 EFPD throughout the cycles. Each flux map has been analyzed with SIMULATE-3, and a summary of comparisons with measured data is displayed in Table 5-7. It can be seen that the SIMULATE-3 radial fission rate distributions (axial integrals over each of the detector positions) are predicted with a mean difference slightly above 1 percent. 3D node-by-node (24 axial nodes) fission rates are predicted with a mean difference of less than 3 percent.

Accurate predictions of fission rate distributions are very important as a starting point for subsequent application of the burnup reactivity decrement methodology because the analytical tools must be capable of accurately predicting fission rate distributions when provided accurate fuel assembly reactivities.

Table 5-7
Comparison of SIMULATE-3 and Measured Fission Rates

Reactor	# of Flux Maps	Mean Radial (2D) r.m.s. Difference (%)	Mean Axial r.m.s. Difference (%)	Mean Nodal (3D) r.m.s. Difference (%)
McGuire-1	161	1.15	1.64	2.64
McGuire-2	171	1.20	1.70	2.67
Catawba-1	179	1.22	1.46	2.50
Catawba-2	169	1.24	1.82	2.82
Un-weighted Average		1.20	1.66	2.66

The flux map measurement errors from reproducibility tests and symmetry measurements are generally observed to be about 0.5% for any individual radial flux map position (thimble). Since the observed deviation between computed and measured fission rates in Table 5-7 has an average r.m.s. difference of 1.2%, the 0.5% “uncertainty” from the measurement is so small that it does not affect the results of this study.

5.6 Reactor Model Summary

The CMS models for the Duke reactors have been developed by applying a production model to all reactor and fuel data supplied by Duke Energy. All four units employ consistent modeling techniques, which is important for combining cross-units results needed for the cumulative statistics in this project.

The agreement of the SIMULATE-3 core follow model with plant measured data demonstrates that both core reactivity and spatial distributions of fission rates are well-predicted throughout the cycles and across all units. Consequently, these models and measured reactor data form a well-qualified basis for the analysis presented in this report.

Section 6: Details of Analysis Implementation

For every reactor condition at which a flux map is available, a sequence of SIMULATE-3 calculations is performed to evaluate the error in sub-batch reactivity for all the sub-batches in the reactor core. Section 3 provided a brief overview of the analysis procedure used to quantify the computed reactivity decrement bias and uncertainty. However, in the overall iterative sequence described in Section 3, there are a number of details that are needed for practical implementation.

6.1 Super-batch Definitions

Since there are many sub-batches (e.g., 4-12) introduced in each cycle (as displayed in Table 5-2), it is important that there are enough assemblies in the core to make a search for the sub-batch reactivity meaningful. For instance, when there are eight or fewer assemblies in a sub-batch, the sub-batch would only occupy a single core location in an octant-symmetrically-loaded core. In such a case, the sensitivity of the r.m.s. differences in computed and measured fission rates would be very sensitive to measurement errors at that core location. In order to alleviate such sensitivities, we have chosen to lump any sub-batches having fewer than 12 assemblies into a super-batch with all corresponding enrichment sub-batches also having fewer than 12 assemblies. Consequently, this super-batch actually represents a number of different burnable poison configurations. All sub-batches with more than 12 assemblies are treated explicitly as their own sub-batch, since the sub-batch will occupy at least 2 different locations in an octant of the reactor core.

6.2 3D Versus 2D Searches

As was pointed out in Section 3, it is not obvious if the search to minimize differences between computed and measured fission rates should be performed with the radial (2D) or nodal (3D) fission rates. We have examined a large number of searches using both the radial and nodal differences to drive the search. In general, little difference has been observed between the results of either type of search, but individual cases can be found in which one or the other seems more effective. Since the nodal search is intuitively more general, we have chosen to base the searches in this report on minimizing the r.m.s. differences in the nodal (3D) fission rates.

In all cases, this search for optimal sub-batch burnup multipliers is guaranteed to reduce the deviation between computed and measured fission rates. Typical reductions in nodal r.m.s. values and corresponding radial r.m.s. values are displayed in Figures 6-1 and 6-2. In such cases, one observes that even though the search minimizes the nodal r.m.s. differences, the radial r.m.s. differences are also all reduced. In fact, it is not uncommon for the magnitude of the reduction in radial r.m.s. differences to exceed that of the nodal r.m.s. differences.

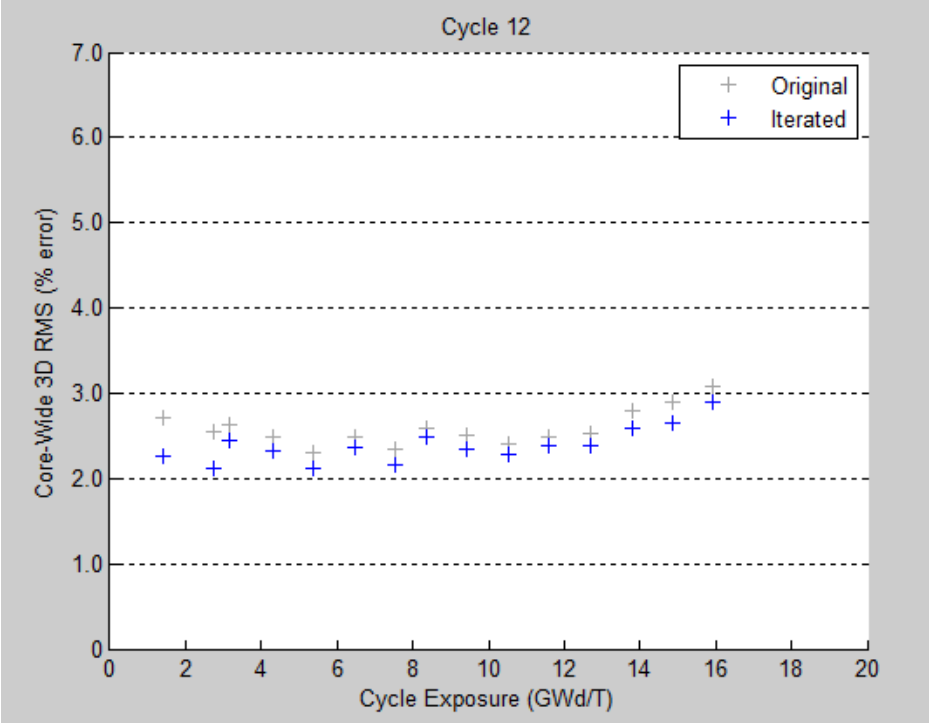

Figure 6-1
Cycle 12 – Nodal r.m.s. Fission Rates

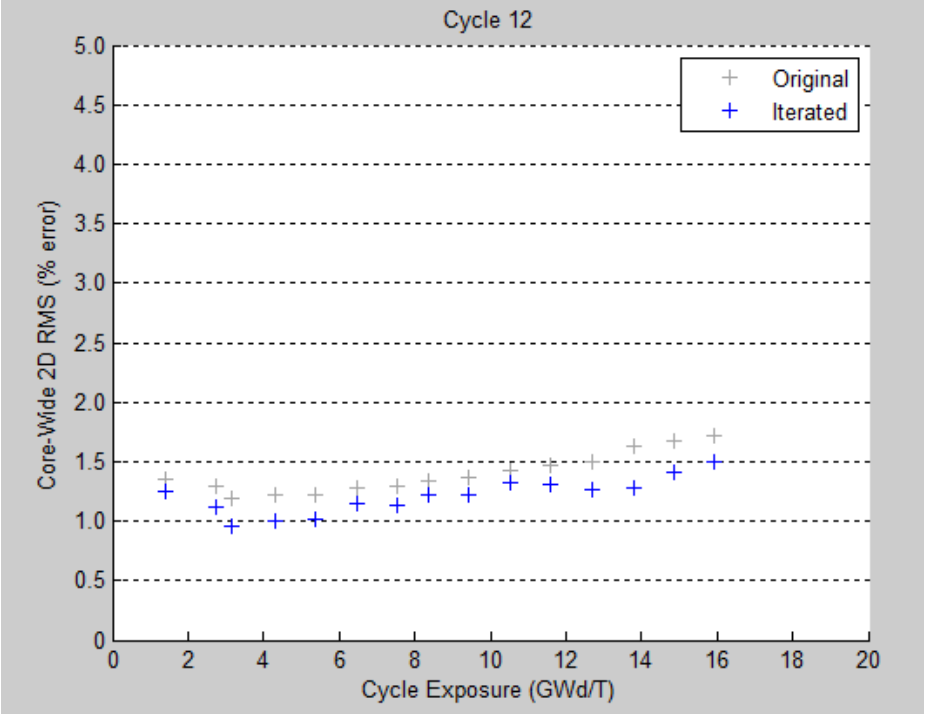

Figure 6-2
Cycle 12 – Radial r.m.s. Fission Rates

However, there is nothing inherent in the search process to guarantee that the radial r.m.s. differences will actually be reduced. By examining a great number of cycles of data, some instances have been found in which iterative reduction of the nodal r.m.s differences actually increases the radial r.m.s differences, as displayed in Figures 6-3 (consistent improvement in core-wide 3D r.m.s.) and 6-4 (inconsistent improvement in core-wide 2D r.m.s.). This behavior has only been observed when initial radial r.m.s. differences are very small (less than 1%), and the increases in the iterative r.m.s. differences are also very small.

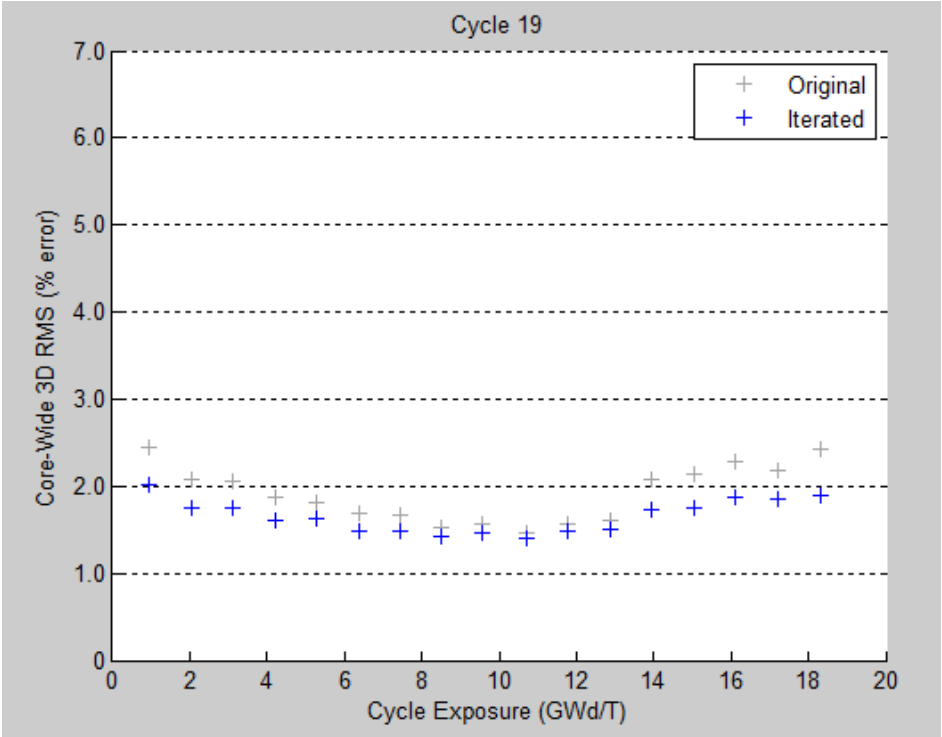

Figure 6-3
Cycle 19 – Nodal r.m.s. Fission Rates

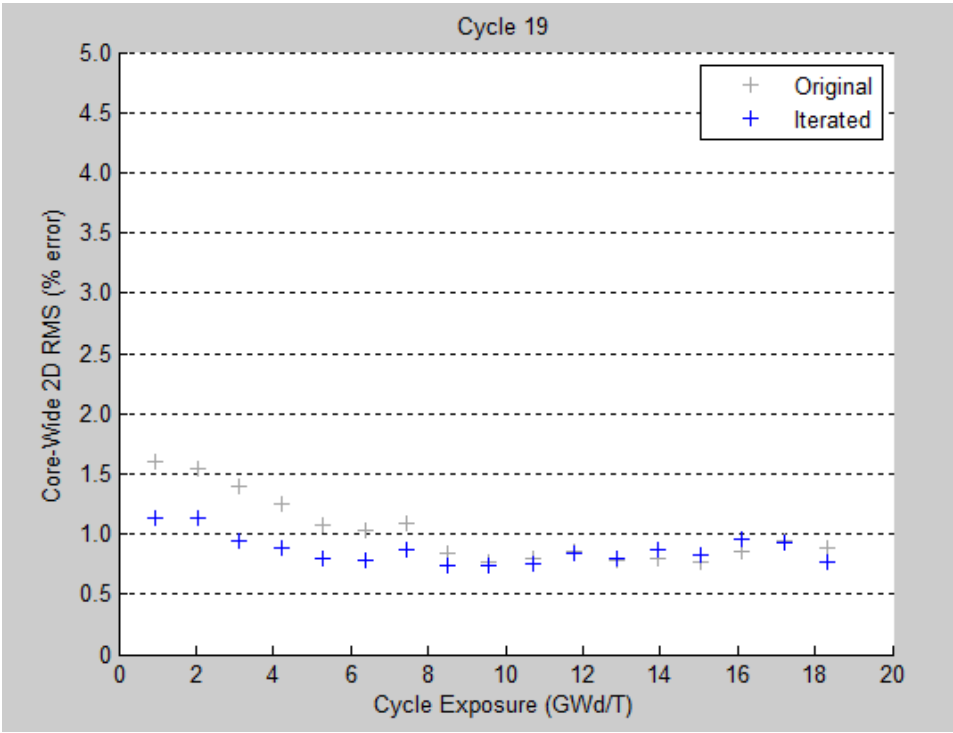

Figure 6-4
Cycle 19 – Radial r.m.s. Fission Rates

6.3 Sub-batch Sensitivities

In order for the search to determine the sub-batch burnup multipliers that minimize r.m.s. differences between the calculation and the measurement, it is important that the sub-batch actually display a significant sensitivity to the sub-batch reactivity multiplier. There are several instances in which this sensitivity does not exist. One such case occurs when a sub-batch is located in core positions of little reactivity worth relative to the locations of in-core detectors – such as when it is placed in extreme peripheral core locations for the sub-batch's last cycle in the core (for example, very low-leakage core loading patterns). When a search for the sub-batch multiplier is performed, one observes a very flat r.m.s. difference as the sub-batch multiplier is changed – as depicted in Figure 6-5 for the Cycle 18 cases. In such cases, the sub-batch multipliers are very sensitive to the iteration, and converged sub-batch multipliers often display large fluctuations at successive flux maps – which is clearly unphysical.

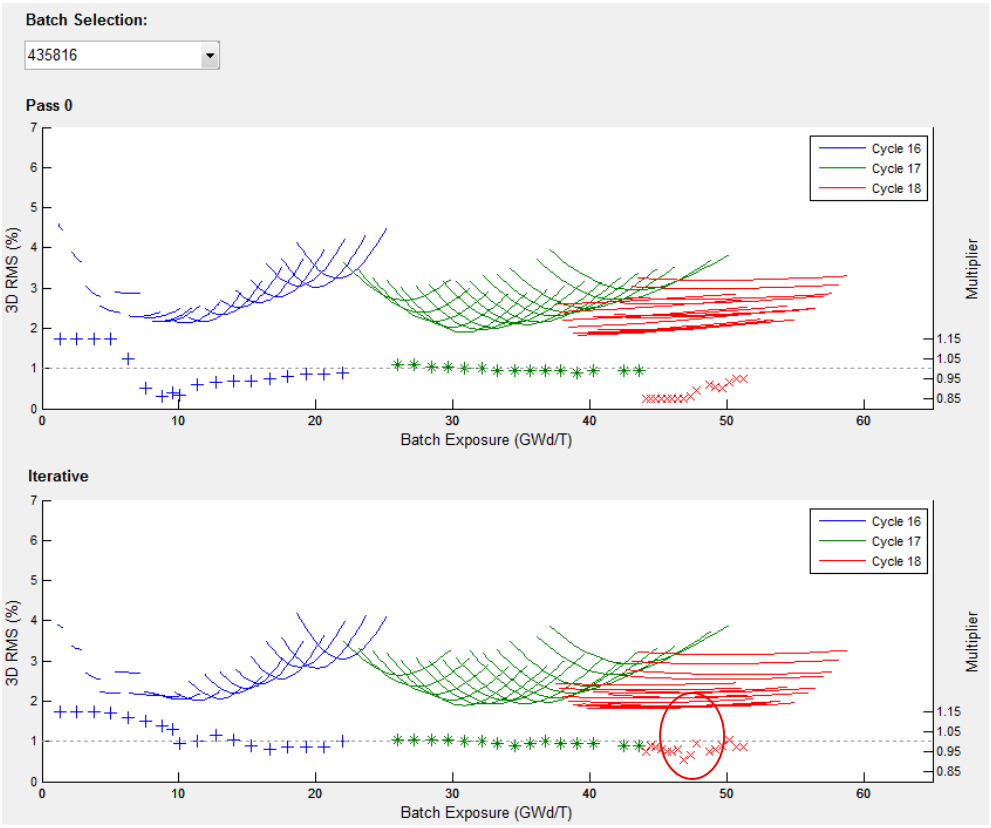

Figure 6-5
Multi-cycle Sub-batch Minimization

Another instance of very low sensitivity can be observed in Figure 6-6 for the data from the first half of Cycle 18. In these cases, the large amount of burnable absorbers makes the k-infinity curve versus burnup almost flat. As a result, there is little sensitivity to the sub-batch burnup - until the burnable absorber is significantly depleted (e.g., 10-15 GWd/T).

Another situation that can lead to small sensitivities occurs when only a few assemblies from a sub-batch are used in a cycle. This often occurs when fuel is inserted into the core for its fourth cycle, as depicted in Figure 6-6. Here for Cycle 21, only a few assemblies of the sub-batch are re-used and there is very little sensitivity to this sub-batch – as evidenced by the flat r.m.s. differences, as the sub-batch multiplier is changed. Note also that the initial and iterative results for this case (the large blue dots) are dramatically different and very uncertain for such low sensitivity cases.

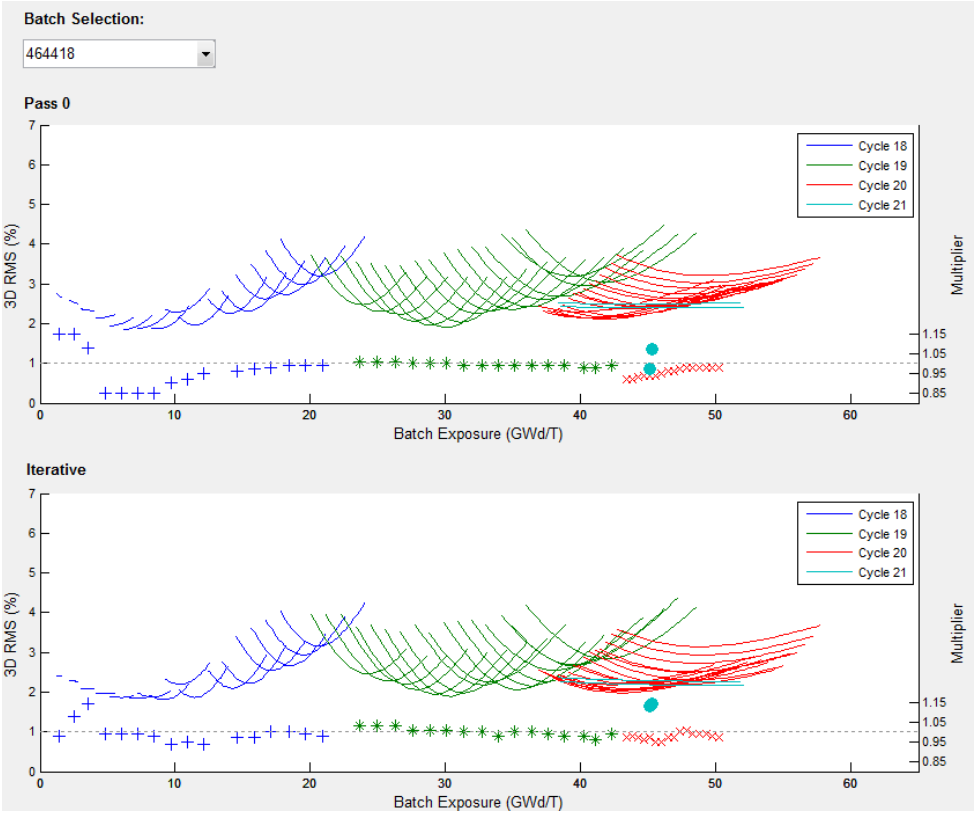

Figure 6-6
Multi-cycle Sub-batch Minimization, Split Batch

Cases that have such low sensitivities are easy to eliminate from the overall search space by simply performing the calculation and monitoring the sensitivity. All such low sensitivity cases are eliminated from the search space – as is explained in the following section.

6.4 Iteration Implementation

The final computational sequence implemented for the analysis in this report can be broken down into a number of discrete steps. For each reactor state at which flux map data is available, the following sequence of steps is performed:

1. Perform standard flux map analysis and compute the initial r.m.s deviation between computed and measured 3D fission rates

2. Start loop over all sub-batches in the core and over all values of the sub-batch burnup multipliers, M_b, from 0.85 to 1.15
    a. For each sub-batch, determine the sub-batch sensitivity, defined as the minimum of the 2D r.m.s with 0.85 and 1.15 multipliers minus the minimum 2D r.m.s.
3. End loop over sub-batches
4. Set all active sub-batch burnup multipliers, M_b^{use}=1.0
5. Start iterative loop for 8 sequential passes
6. Start loop over all sub-batches in the core from maximum to minimum sub-batch sensitivity and over all values of sub-batch burnup multipliers from 0.85 to 1.15
    a. update the active value of M_b^{use} with the value of M_b corresponding to the minimum 3D r.m.s. (subject to the constraint that M_b^{use} not change by more than +/- an input value (0.02) in any single pass)
    b. If the current sub-batch sensitivity is less than an input value (0.3%) or if the number of assemblies in the sub-batch is less than an input value (12) set the active value of the sub-batch multiplier M_b^{use} to 1.0
7. End loop over sub-batches
8. End iterative loop over sequential passes
9. For all sub-batches (not subject to the constraint of step 6b), compute the SIMULATE-3 reactivity error as the difference of sub-batch reactivities for $M_b = M_b^{use}$ and M_b=1.0

This iterative procedure constrains the change in sub-batch multipliers to be less than 0.02 at each pass so that small changes in sub-batch multipliers are made for all sub-batches before any sub-batch multiplier is changed by a large amount. The rationale for this choice is that the r.m.s differences are often sensitive to all sub-batch multipliers, and it is undesirable to complete a search for one sub-batch before examining the impacts of the other sub-batches in the core. In any case, it should be recognized that this search solves a local minimization problem and is not guaranteed to find the global minimum (which is nearly impossible to determine).

This analytical procedure is also performed for a fixed number of iterations rather than monitoring directly the convergence of results. The reason for this choice is that since sub-batch multipliers are changed in finite steps of 0.01, there are rare cases in which some sub-batches produce multipliers that oscillate by 0.01 in successive passes. This level of oscillation is certainly not important for determining the error in sub-batch reactivity (as explained in the following section), and it is far more straightforward to accept such oscillations as an additional uncertainty – rather than switching to a continuous variable search to find the true local minimum.

Figure 6-7 displays sub-batch multipliers for one sub-batch in Cycles 16 to 18, and it can be seen that the iteration produces values that are more consistent from cycle to cycle than the pass zero results. This is not only more physical (i.e., reactivity discrepancies should be smooth functions of sub-batch burnup across cycles), but also provides indirect indication that the simultaneous search across all sub-batches is effectively implemented in SIMULATE-3.

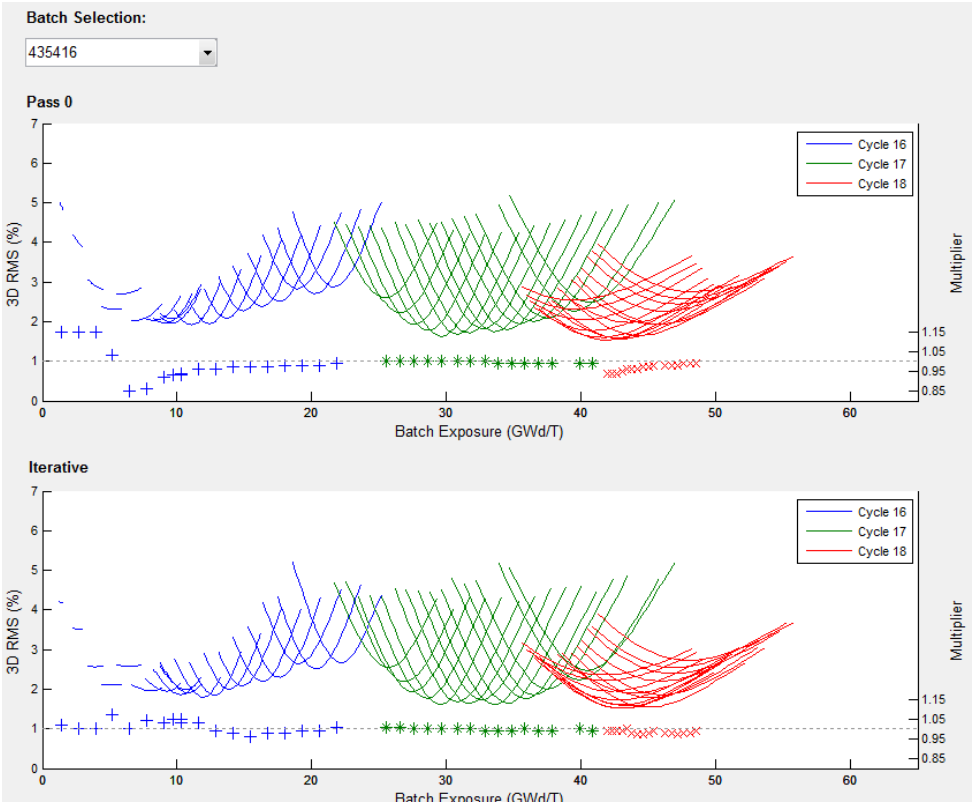

Figure 6-7
Effective Multi-cycle Sub-batch Minimization

For each flux map, this analytical procedure requires approximately 4000 SIMULATE-3 calculations (11 total passes x 31 sub-batch multipliers/sub-batch x ~12 sub-batches in the core). Consequently, analysis of the 44 Duke reactor cycles (680 flux maps) requires a total of approximately 2.7 million SIMULATE-3 cases to be executed. Coding changes have been made in SIMULATE-3 (Version 6.09.22_EPRI) so that this procedure is automatically invoked without need for human intervention, and search results are recorded in a special file that is post-processed to make plots and spreadsheets of results.

Section 7: Measured HFP Reactivity Bias and Uncertainty

The SIMULATE-3 flux map analysis procedure described in Section 6 was performed for all flux maps in the 44 cycles of Catawba Units 1 and 2 and McGuire Units 1 and 2 for which reactor power was above 95%. This analysis produces HFP measured reactivity errors for each sub-batch at each flux map. This section describes how the data from this analysis are used to infer biases in CASMO-5 sub-batch reactivities, and how these biases are translated into measured reactivity decrements and corresponding uncertainties.

7.1 Interpretation of Data

If one plots the estimated sub-batch reactivity biases (Δk in pcm) versus sub-batch burnup, the data appear as displayed in Figure 7-1. These 2856 measured sub-batch reactivities represent those points from the complete set of approximately 8000 data points (680 maps x ~12 sub-batches per map) that satisfied the two screening criteria of having 12 or more assemblies in a sub-batch and having a detector r.m.s. difference sensitivity greater than 0.3% – as fission rate differences were iteratively minimized.

The 0.3% minimum sensitivity criteria used in the iterative minimization of r.m.s. differences was necessary so that sub-batches with sensitivities that approach zero would not be interpreted as requiring near-infinite changes in assembly reactivity to minimize fission rate r.m.s. differences. An alternate interpretation of such sub-batches is that the variances of inferred reactivity biases approach infinity for sub-batches with near-zero sensitivity. Treatment of sub-batch sensitivities and variances of the retained 2856 measured sub-batch reactivities are explicitly addressed (in Section 7.2) where the use of WLS regressions is detailed.

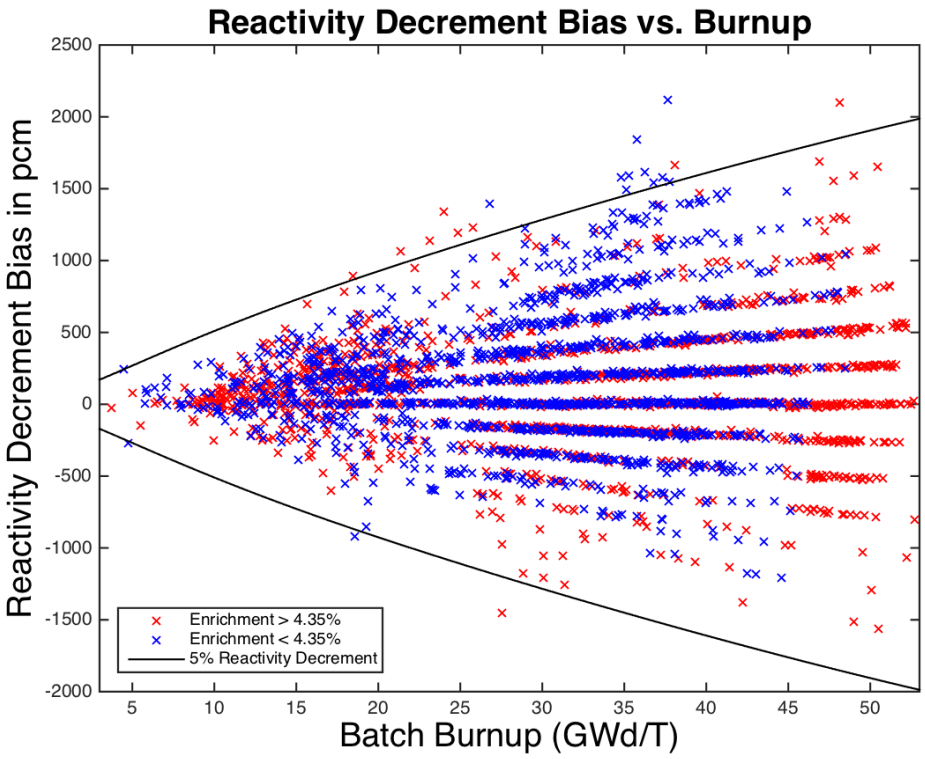

Figure 7-1
Casmo-5 Bias in Reactivity

For comparison purposes, the +/-5% reactivity decrement curves (as computed for a 4.75% enriched, no burnable poison Westinghouse RFA fuel lattice at 900 ppm boron) are plotted in this figure with the two black lines. These curves do not correspond directly to the most appropriate 5% reactivity decrement since reactivities in this plot are computed at HFP conditions with CASMO-5 – not at cold conditions with SFP criticality tools. Nonetheless, the curves provide useful insight to help interpret the scatter in individual data points.

There are a number of things that can be observed from this data. First, there are very few data points at less than 10 GWd/T burnup. This is a result of the fact that almost all sub-batches have large amounts of burnable absorber – which makes the k-infinity curve very flat in burnup, as observed from the boron letdown curve in Figure 5-1. Consequently, **no attempt will be made to quantify the reactivity decrement biases or uncertainties for burnups less than 10 GWd/T.** One should note that since reactivity decrement biases and uncertainties at zero burnup are by definition zero, it should be easy to estimate reactivity decrement biases and uncertainties in this range. Normally, interest focuses on much higher burnups for spent fuel criticality analyses.

One also observes that the data form distinct "lines," particularly at high burnup. This is a direct result of two facts: 1) the slopes of fuel reactivity vs. burnup are very similar for all fuel types (after burnable absorbers are depleted), and 2) the

search for sub-batch burnup multipliers was performed with a discrete 0.01 multiplier resolution. Consequently, the data behavior is expected, and one should simply interpret each data point as each having an intrinsic added "measurement" uncertainty proportional to burnup and having a magnitude of approximately +/-100 pcm at 50 GWd/T. Because there are so many data points in the composite set of data, this uncertainty has almost no impact on results deduced from the data.

At first glance, the data appear to be nearly equally distributed around 0 pcm decrement error, with a large spread in individual points. It is important to understand what influences this spread in data. Items known to contribute to the spread in the individual data points of Figure 7-1 include:

- Fission rate measurement errors or uncertainties
- Differences in sub-batch spectra vs. CASMO-5 lattice assumption (zero leakage)
- Differences in intra-assembly spatial flux distributions vs. lattice assumption
- Influences from super-batch lumping of multiple burnable poison loadings
- Imperfect knowledge of core configuration (fuel bowing, fuel elongation, crud)
- Errors in computed sub-batch burnups (used as the plot ordinate)
- Errors in SIMULATE-3 nodal and detector physics models
- Errors in SIMULATE-3 cross-section data fitting models
- ✓ Errors in CASMO-5 computed nuclide inventory vs. fuel burnup
- ✓ Errors in fundamental neutron cross-section data
- ✓ Imperfect knowledge of reactor operating power level

The items in this list have been divided into two sets, indicated by bullet type. The simple bulleted terms have two distinct characteristics: 1) because both measured and computed fission rates are normalized distributions, these effects are expected to be randomly distributed with little bias, and 2) these effects either do not enter into SFP/cask criticality analysis or are treated with their own uncertainties. For instance, errors in SIMULATE-3 models or lattice spectral assumptions are not relevant for SFP analysis because such analysis is performed directly by Monte Carlo in rack geometry.

The first two of the check-mark bulleted items in this list are the two terms we seek to measure in this project, and it is clear that the effects in this sub-list will not be random in nature – as one expects these errors to change systematically (in an as-yet unknown manner) as fuel assemblies are burned.

In the iterative analysis method, all categories of errors are treated as if they are errors in CASMO-5 sub-batch reactivities – which is the reason we expect the

spread in individual data points to be much larger than the actual CASMO-5 sub-batch reactivity errors. What remains to be shown is that one can use this set of data, with its inherent spread, to correctly deduce the errors in CASMO-5 lattice reactivities.

7.2 Sub-batch Sensitivities

The measured reactivity decrement bias data was plotted vs. sub-batch sensitivity, and a quadratic regression was performed to determine the 95% prediction interval for the reactivity decrement bias versus sub-batch sensitivity, as displayed in Figure 7-2. The 95% prediction interval was used to compute the normalized shape of 2-sigma variation versus sensitivity. The data was fitted only up to a sensitivity of 4.0%, as the data becomes exceedingly sparse at the higher sensitivity end of the data. The plus signs in this figure are variance points as determined using the MATLAB [21] VAR function for eight separate sub-batch sensitivity bins - to verify that the quadratic fit was reasonable.

The data in Figure 7-2 demonstrate that many sub-batches with low sensitivities have the largest measured reactivity decrement biases. This is not unexpected, because sub-batches that have very little influence on the computed fission rate distributions require a very large change in computed sub-batch reactivity (k-infinity) to change the computed fission rate distribution and minimize deviations from the measured fission rate distributions. The correlation between sub-batch sensitivity and reactivity decrement bias will become important later when regression analysis of the data is used to infer biases and uncertainties for the reactivity decrement biases as a function of sub-batch burnup.

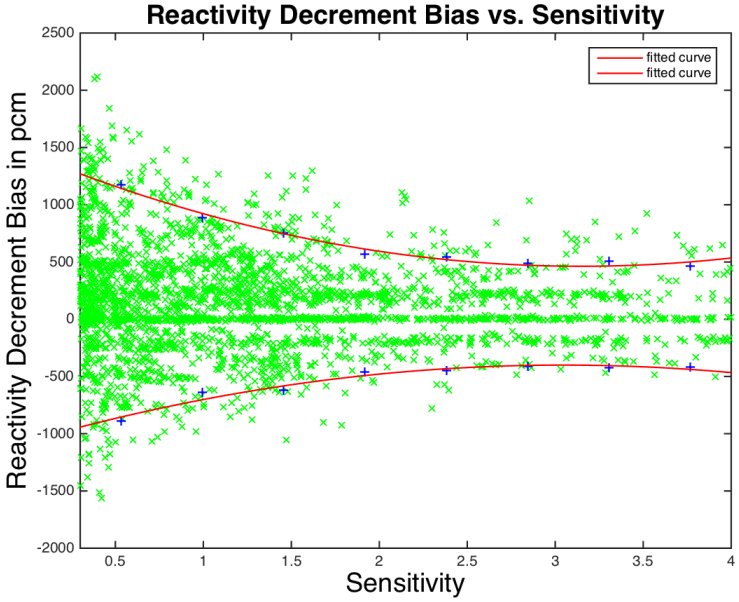

Figure 7-2
Reactivity Decrement Bias vs. Sub-batch Sensitivity

7.3 Sensitivities to Reactor Unit

If the data are examined separately for each of the four reactor units, the plots displayed in Figures 7-3 to 7-6 are obtained. The data in each plot show that there is very little difference between burnup reactivity decrement biases measured in one unit or another. Since all four units have fuels of similar range of enrichments and burnable absorbers, the lack of sensitivity to the reactor unit is not surprising. Consequently, for the analysis that follows in this report, data for all four units are treated as a single large data set in which measured sub-batch reactivity decrement biases do not depend on the reactor unit in which each fuel sub-batch was depleted.

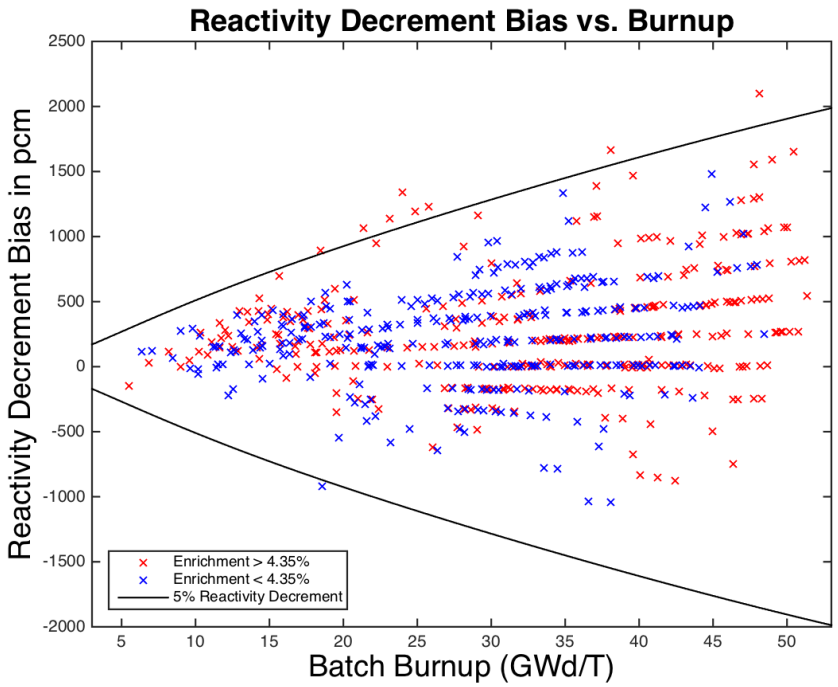

Figure 7-3
Bias in Reactivity Decrement – McGuire-1

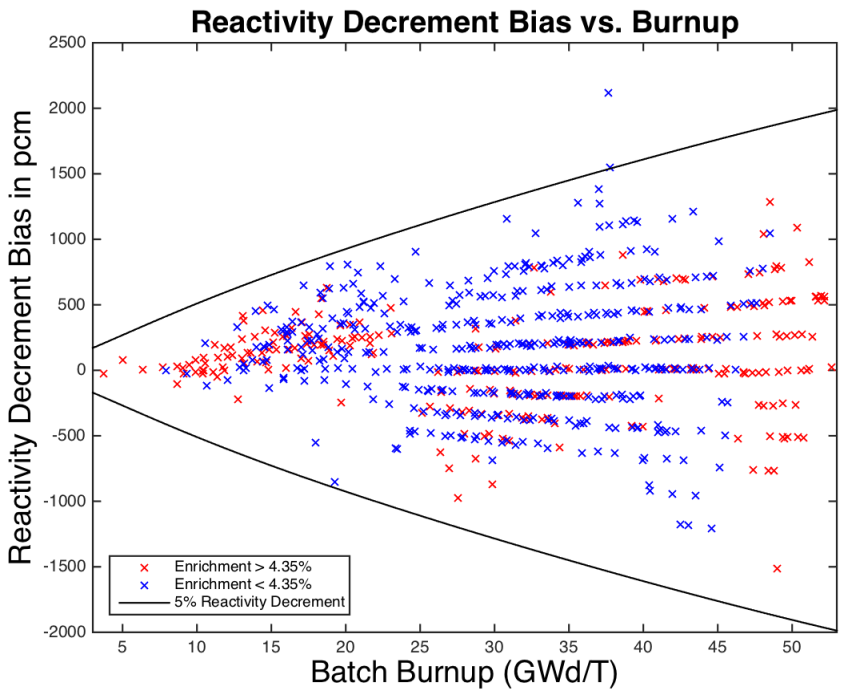

Figure 7-4
Bias in Reactivity Decrement – McGuire-2

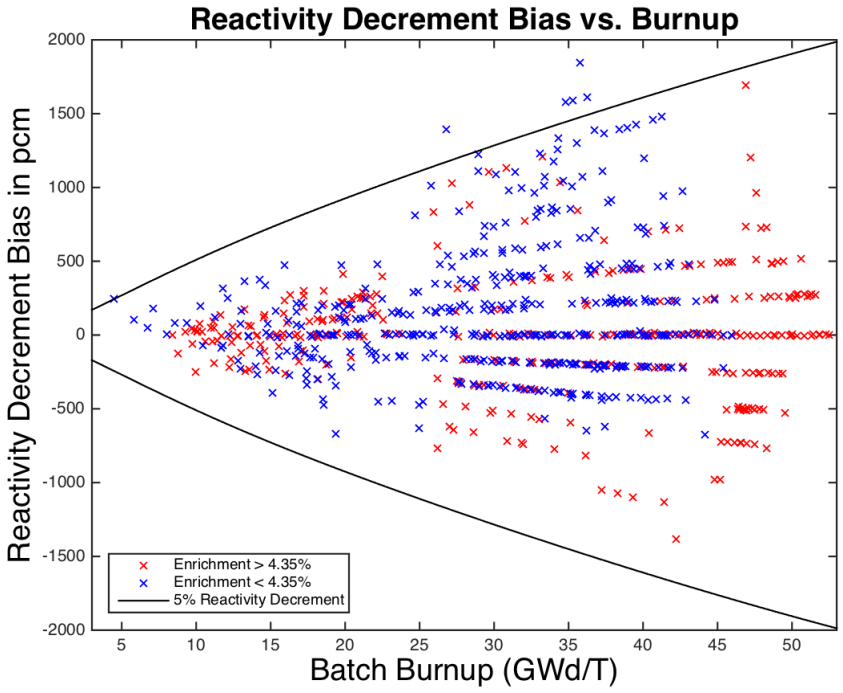

Figure 7-5
Bias in Reactivity Decrement – Catawba-1

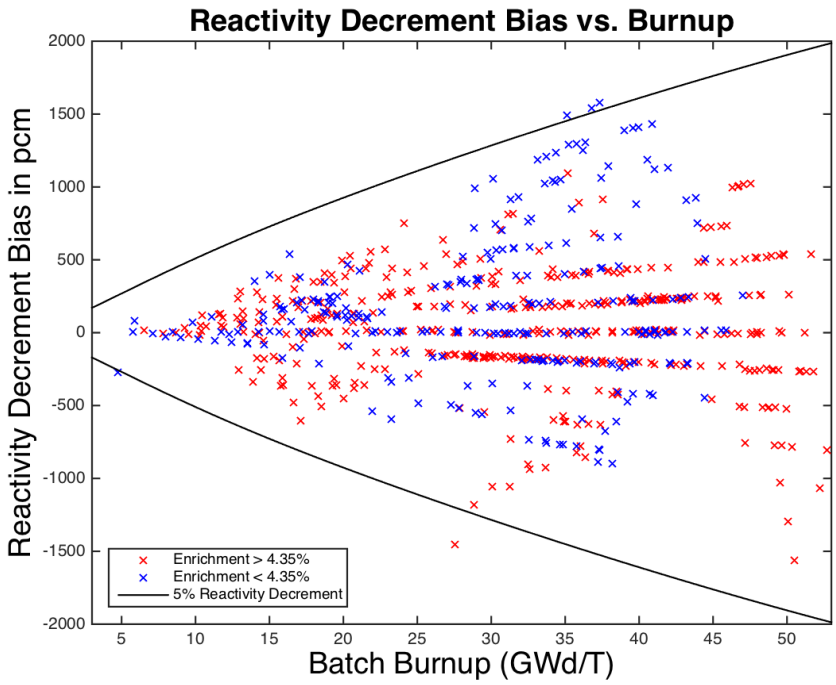

Figure 7-6
Bias in Reactivity Decrement – Catawba-2

Because the data for each of the four units are so similar, all data will be lumped together for the remainder of this report so that more data points are available to improve the statistics of measured reactivity decrements biases and uncertainties.

7.4 Sub-batch Enrichment Sensitivities

The fuel sub-batches for the Duke reactors span the range of enrichments from 3.4% to 4.9% enrichment in ^{235}U. The measured reactivity decrement biases plotted in Figures 7-1 and 7-2 to 7-6 are displayed in blue for the enrichment range of 3.4% to 4.35% and in red for the range from 4.35% to 4.90%.

There is no significant trend of the reactivity decrement bias with burnup, so all of the data will be treated as a single set without regard to sub-batch enrichment, so we can look more precisely at the burnup dependence of the reactivity decrement bias.

7.5 Burnup Reactivity Decrement Biases and Prediction Intervals

With all units, enrichments, and sub-batches lumped into one data set we can perform regression analysis of the data to determine the burnup dependence of CASMO-5 bias and uncertainty of reactivity decrements. Figure 7-7 displays results of MATLAB's ordinary least squares (OLS) quadratic regression

constrained to zero bias at zero burnup (i.e., since burnup reactivity decrement is 0.0 at zero burnup by definition, then the bias must also be 0.0 at zero burnup).

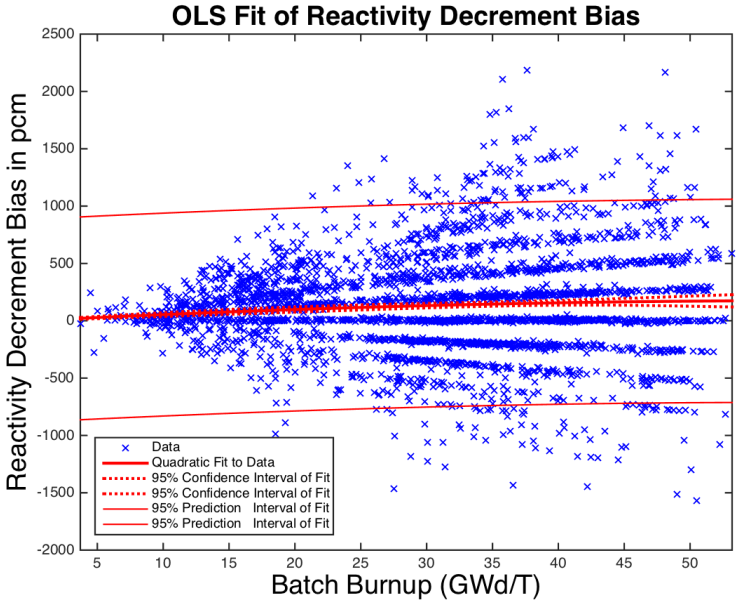

Figure 7-7
CASMO-5 Decrement Bias Fit – Quadratic Regression

From this plot it can be seen that the regression fit to the bias has a shape that grows from 0.0 to about 200 pcm at 50 GWd/T burnup. The prediction interval width has the same shape in burnup as the bias, with a half-width of about 900 pcm. In order for the prediction intervals derived from the OLS regression analysis to be strictly applicable, the data should satisfy certain criteria:

- The ordinate values must be known exactly (the sub-batch burnups)
- The variance of each data point must be independent of the ordinate
- Every data point must be independent from all other points
- The residuals (differences between the individual points and the regression fit at that ordinate) must have normal distributions for all ordinate values

Unfortunately, none of these points are satisfied by the regression data in Figure 7-7:

1. the ordinates are not known exactly - since they are computed not measured burnups,
2. the data is heteroscedastic, as the variance grows with burnup and this variation cannot be known precisely,
3. the data at successive flux maps are correlated - since core power distributions evolve slowly, results from one flux map and the next are highly correlated,
4. the residuals here are clearly not normally distributed.

The fact that the sub-batch burnups are not known exactly (burnups are a SIMULATE-3 computed parameter) is not a very important limitation for the regression, because uncertainty in the sub-batch burnup merely affects the abscissa positioning (horizontal) of data and not the data ordinate (vertical) value. Consequently, it is easy to surmise that the impact on the regression fit from misplacing of sub-batch burnups will be very small. However, the OLS assumption that the variance is independent of burnup is clearly not valid. This is, in fact, the reason that bounds were historically expressed in terms of a percentage of burnup reactivity decrement, so the bounds would grow with burnup.

We can plot the absolute value of decrement bias data vs. sub-batch burnup and use a quadratic regression to determine the 95% prediction interval for the reactivity decrement bias versus sub-batch burnup, as displayed in Figure 7-8. The fitted 95% prediction interval was used to compute the shape of 2-sigma data variation versus burnup, and the square of this variation (the variance) was fit to a quadratic polynomial and renormalized as displayed in Figure 7-9. This figure also contains variance points, as determined using the MATLAB VAR function for fifteen separate sub-batch burnup bins - to verify that the quadratic fit was reasonable.

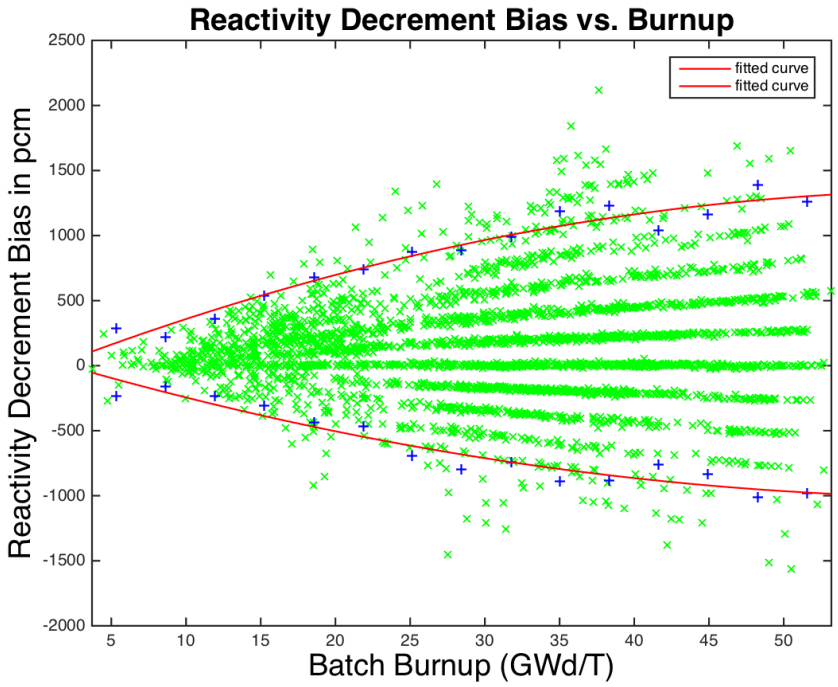

Figure 7-8
Decrement Bias Prediction Interval vs. Sub-batch Burnup

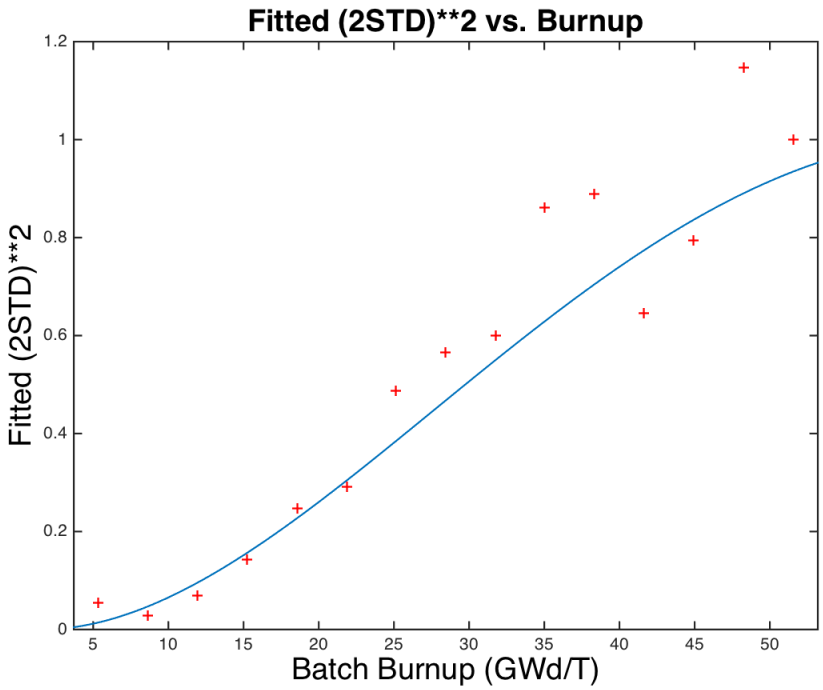

Figure 7-9
Decrement Bias Variance Shape vs. Sub-batch Burnup

Having an estimate of the burnup dependence of the variance for the heteroscedastic data, we can now perform weighted least square (WLS) regression and derive non-constant prediction intervals for the regression data. Regression fits versus burnup were performed using the MATLAB *nlinfit* function with the '*weight*' option to use the individual data weights, computed as described above. Confidence intervals corresponding to each data point were computed using the MATLAB *nlpredci* function with *'Covar'*, and '*weight*' options. Confidence interval curves as a function of burnup were computed using MATLAB *polyfit* function to fit individual confidence interval data to 6-th order polynomials (since the confidence interval has more shape than the quadratic regression). Prediction intervals corresponding to each data point were computed using the MATLAB *nlpredci* function with *'Covar'*, *'predopt' 'observation'*, and '*weight*' options. Prediction interval curves as a function of burnup were computed using MATLAB *nlinfit* function to fit individual prediction interval data to quadratic polynomials - constrained to a value of 0.0 at 0.0 GWd/T burnup.

Applying linear and quadratic WLS regressions to the decrement bias data using a weight function for sub-batch *i* as a function of sub-batch burnup,

$$W_i = \frac{1}{\sigma^2(B_i)},$$

the regression results displayed in Figure 7-10 and 7-11 are obtained.

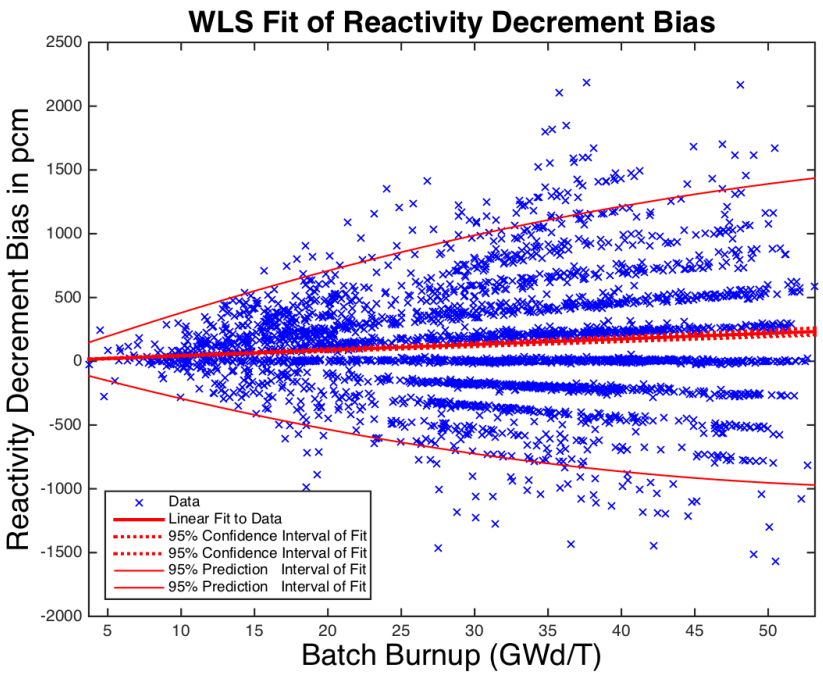

Figure 7-10
*Decrement Bias WLS **Linear** Regression vs. Burnup*

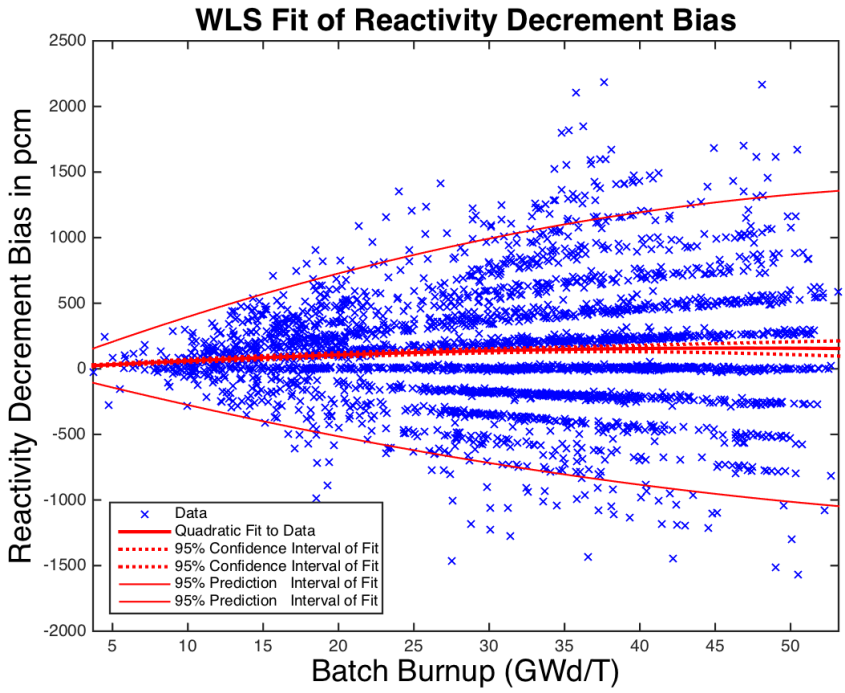

Figure 7-11
*Decrement Bias WLS **Quadratic** Regression vs. Burnup*

These prediction intervals now accurately capture the heteroscedastic nature of the data variances, and these prediction intervals follow the traditional bounding shape. The differences between the linear and the quadratic regressions are not very large, but the quadratic regression prediction interval is narrower than the linear regression. The quadratic reactivity decrement bias at large burnup is considerably flatter at high burnup, and this shape is closer to that might be expected from the physics of lattice depletions - where any bias introduced in computational models from the misprediction of higher actinide effects might be expected to saturate at high burnup. Regression performed in subsequent analysis of this report use quadratic regressions, so the fits can become flatter at high burnup – if the data support such a shape.

The reactivity decrement data are heteroscedastic in not only sub-batch burnup, but also in sub-batch sensitivity. This dependence was displayed in Figure 7-2, which is repeated here as Figure 7-12. The 95% prediction interval width was used to compute the normalized shape of 2-sigma variation versus sensitivity. The square of this variation (the variance) was fit to a quadratic polynomial and normalized as displayed in Figure 7-13. The 2856 data points were fit only up to a sensitivity of 4.0%, as the data become exceedingly sparse at the higher sensitivity end of the data. The plus signs in this figure are variance points as determined using the MATLAB VAR function for eight separate sub-batch sensitivity bins - to verify that the quadratic fit was reasonable.

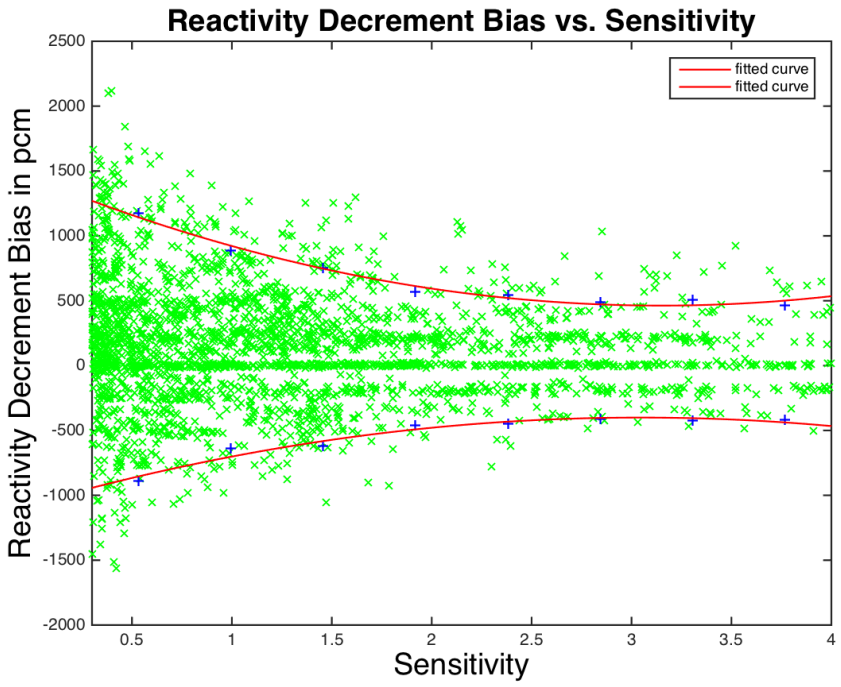

Figure 7-12
Decrement Bias Standard Deviation vs. Sub-batch Sensitivity

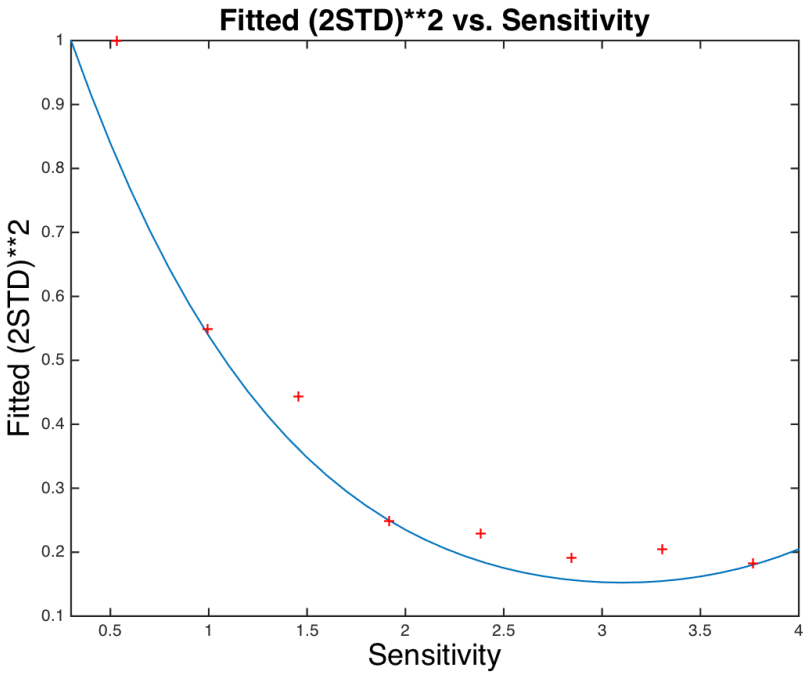

Figure 7-13
Decrement Bias Variance Shape vs. Sub-batch Sensitivity

MATLAB WLS quadratic regressions to the decrement bias data were performed using weight functions for sub-batch *i*, incorporating both sub-batch burnup and sub-batch sensitivity using two different variants of the weight function,

$$W_i = \frac{1}{\sigma^2(B_i)} + \frac{1}{\sigma^2(S_i)} \quad \textit{and} \quad W_i = \frac{1}{\sigma^2(B_i)} \cdot \frac{1}{\sigma^2(S_i)}.$$

There was little difference between regression fits and prediction intervals computed using these two variance estimation procedures. However, the product formulation was selected for all subsequent regression analysis based on the fact that it correctly produces zero weight should either the sensitivity or burnup variances go to infinity, and the additive formulation does not have this property.

The quadratic regression fits and prediction intervals obtained using both heteroscedastic terms (sub-batch burnup and sensitivity) are displayed in Figure 7-14. The prediction interval width is narrower than that previously displayed in Figure 7-11 where heteroscedastic sensitivities were not treated.

The narrower prediction interval fits with one's intuition from observing the strong correlation between reactivity decrement bias and sensitivity, as shown in Figure 7-12. All subsequent results in this report treat the heteroscedastic nature of both the sub-batch sensitivity and sub-batch burnup.

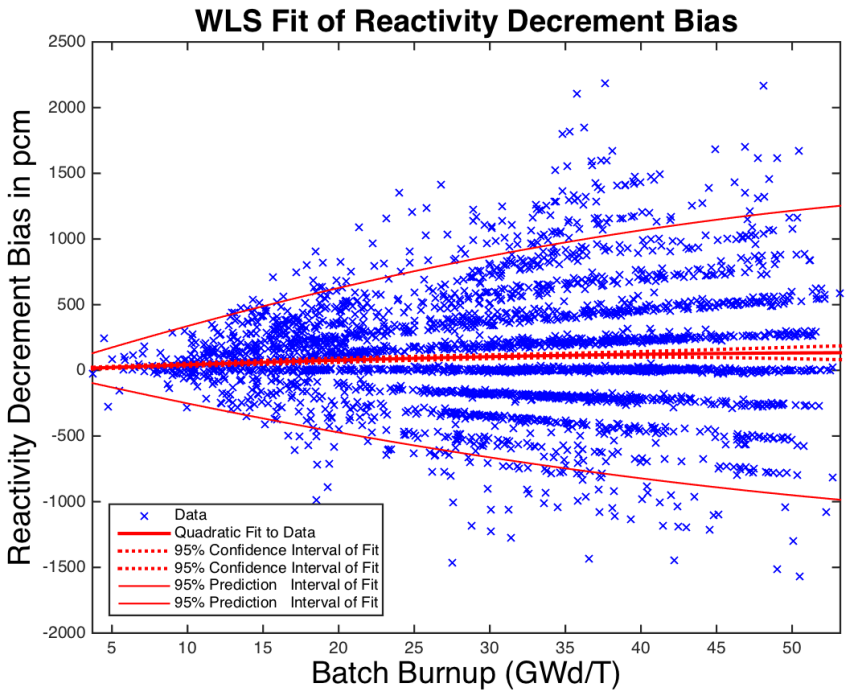

Figure 7-14
Decrement Bias WLS Quadratic Regression vs. Burnup

7.6 Further Refinements of Burnup Reactivity Decrement Biases and Prediction Intervals

There are a few additional refinements of the regression analysis that are required to account for other small deficiencies of the experimental measured reactivity decrement bias data.

The first of these refinements arises from the fact that the sub-batch decrement burnup multipliers that were used to compute sub-batch reactivity bias (in pcm) made the assumption that all fuel within a sub-batch could be represented by a single sub-batch-average burnup. A conservative correction for computing reactivity decrement biases from batch-averaged burnups can be implemented by:

1. evaluating the maximum value of the second derivative of reactivity within each sub-batch/cycle burnup range,

2. multiplying this second derivative by the maximum difference of any assembly burnup from the sub-batch average burnup, and

3. multiplying this result by the sub-batch average burnup change ($E_M - E_{ave}$) determined in the ^{235}U fission distribution r.m.s. minimization.

The sub-batch bias and sub-batch bias additions are depicted schematically in Figure 7-15 for a hypothetical sub-batch of three assemblies having burnup E_1, E_2, and E_3.

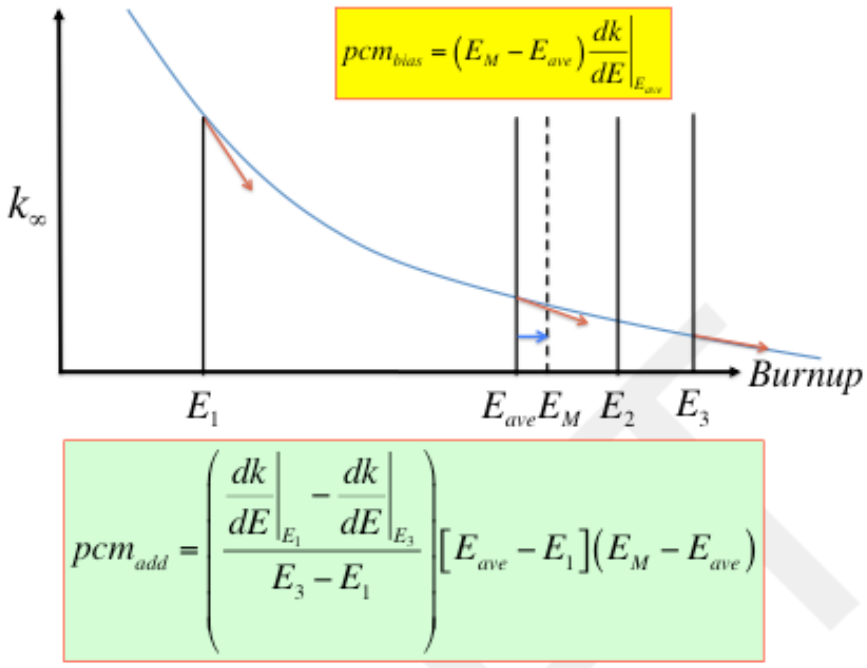

Figure 7-15
Correction for Sub-Batch Burnup Distributions

These reactivity decrement bias additions for all data points are displayed in Figure 7-16. The magnitude of these corrections is very small for most data points because either the slope of reactivity is nearly constant within the range of batch burnup within a cycle, or because the range of intra-batch burnup is very small. (Note that if the derivative of k-infinity were independent of burnup, the intra-sub-batch burnup distribution would require no additional correction to the bias.) When considering all sub-batch data points, the average of the maximum deviation of intra-batch burnup from the sub-batch average burnup is 2.0 GWd/T in absolute units and 6.6% in relative terms – not very large. The implementation of this correction includes three additional conservatisms:

1. The second derivative of reactivity is evaluated at its maximum anywhere in the sub-batch/cycle.
2. The intra-batch burnup difference is taken as the maximum value within the sub-batch – even when it corresponds to only a single assembly of all the assemblies within the sub-batch.
3. The intra-batch burnup distribution correction is explicitly added to each sub-batch's measured reactivity decrement bias, and the sign of the addition

is selected to maximize the absolute value of reactivity decrement bias (for example, positive biases are increased and negative biases are decreased).

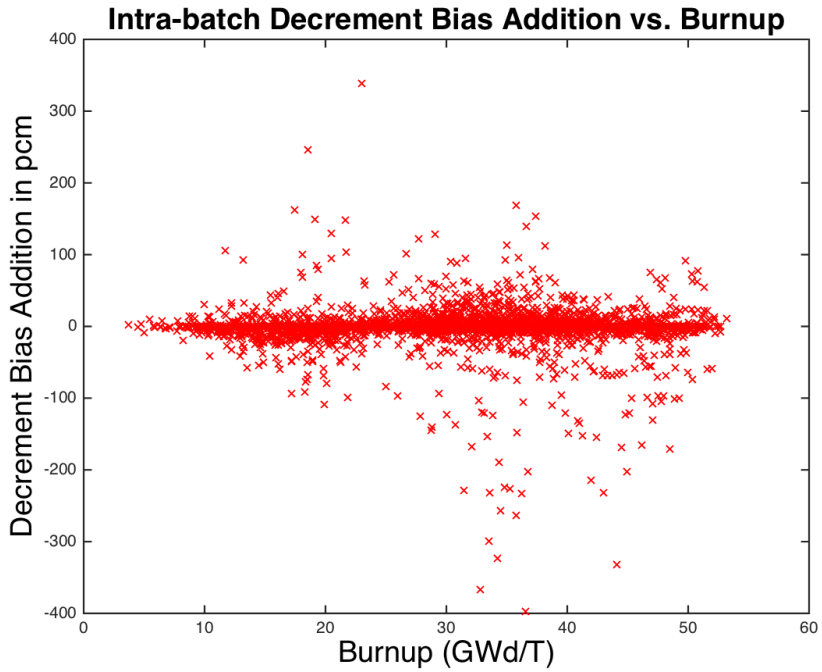

Figure 7-16
Intra-batch Reactivity Decrement Bias Addition vs. Sub-batch Burnup

Another limitation of the experimentally measured burnup reactivity decrement bias data mentioned previously in Section 7.5 was that every data point must be independent from every other point. We know that the data at successive flux maps are highly correlated - since core power distributions evolve slowly, results from one flux map and the next are very highly correlated. Rather than treating this correlation directly, we have chosen to make the approximation that all data for one sub-batch within each reactor cycle are fully correlated. We can then collapse all data within individual sub-batch/cycles to one average value per cycle by statistically combining individual reactivity decrement biases and burnups with their respective weights (i.e., the reciprocal variance product). This is the assumption of 100% correlation of data within each sub-batch/cycle which is necessary so regression fit confidence intervals can be applied correctly (given that we do not know the precise intra-cycle correlation of data that would be needed to use individual data point regressions). When collapsed over each cycle, there are 270 sub-batch/cycle reactivity decrement bias points available for the subsequent analysis.

Two different methods for collapsing the sub-batch/cycle decrement bias data were examined:

1. un-weighted collapsing and

2. collapsing with individual data weights.

Figure 7-17 displays un-collapsed and collapsed reactivity decrement bias data for nine typical sub-batch/cycles. In this figure:

- **The diamond** symbols represent burnup points of **un-collapsed data**,
- the **square** symbols represent **un-weighted** collapsed points, and
- the **circle** symbols represent the **weighted** collapsed points.

By examining data for separate colors (i.e., sub-batches) it can be seen that weighted and un-weighed collapsed data differ very little in reactivity decrement bias and only slightly more in collapsed burnup. As might be expected, regression analysis was shown to be extremely insensitive to the collapsing method employed, so the more intuitive **weighted collapse** was selected for all subsequent regression analysis.

A WLS quadratic regression fit of the sub-batch/cycle-collapsed data is displayed in Figure 7-18. Note that the data tend to separate into three clusters that represent the fresh, once-burned, and twice-burned fuel sub-batches. Note the prediction intervals are still narrower than those obtained in the previous un-collapsed WLS regression of the 2856 individual data points, as displayed in Figure 7-14.

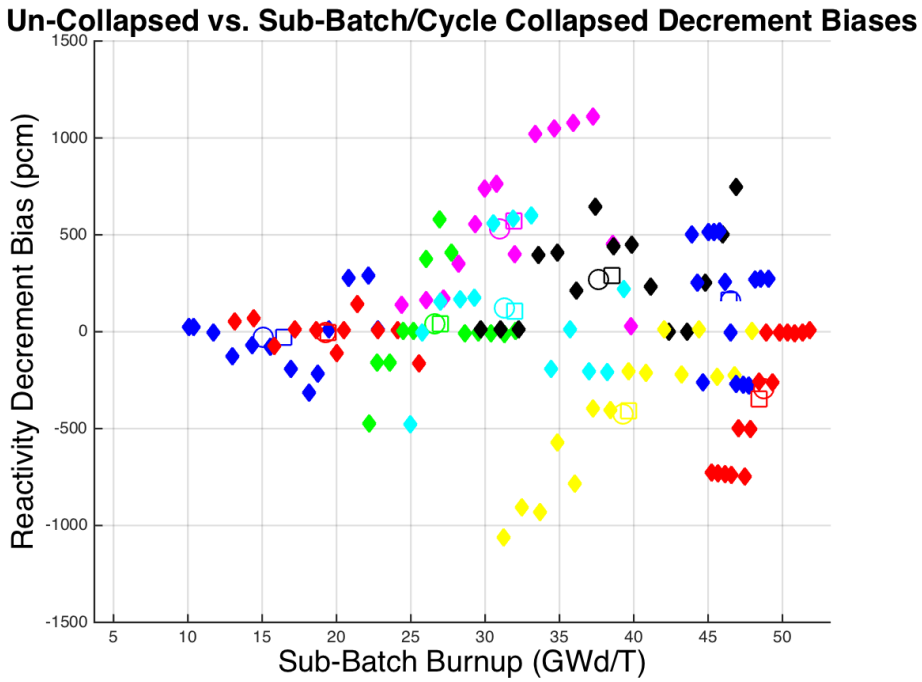

Figure 7-17
Cycle-collapsed Reactivity Decrement Data

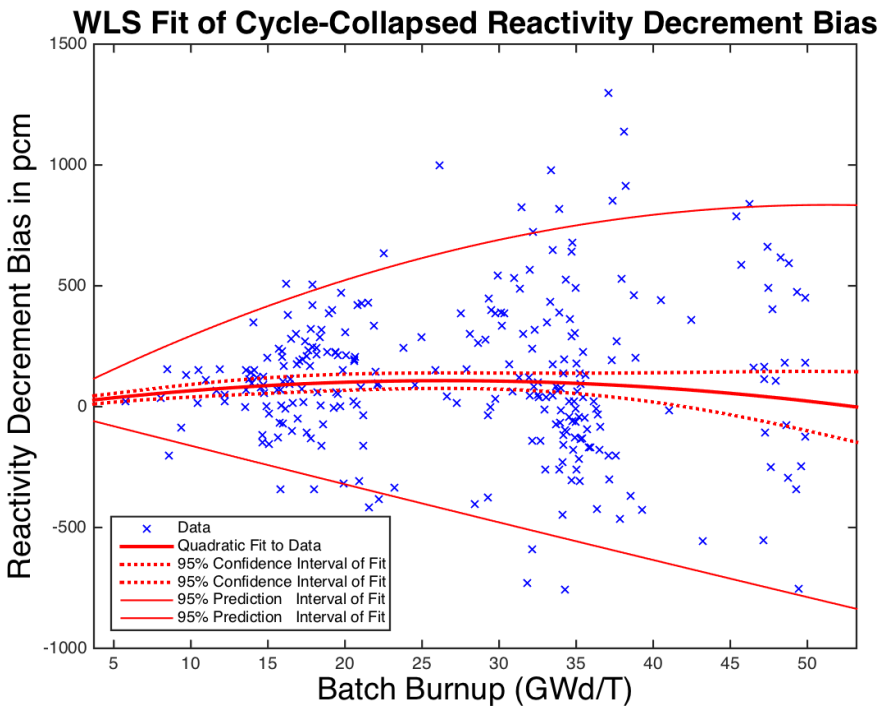

Figure 7-18
Reactivity Decrement Quadratic WLS Regression for Cycle-collapsed Data

The shape of the prediction interval bounds in Figure 7-18 appears to deviate from the "cone" shape of previous figures because of the parabolic shape of the regression fit, but the prediction interval width remains similar. This is clearer in Figure 7-19, where **linear** WLS regression results are displayed, and the prediction interval appears more conical. Note in the linear regression, the confidence interval is narrower than that of the quadratic regression of Figure 7-18. However, we still chose to use quadratic regressions because it is important to allow for a regression shape that could have an asymptotic value at large burnups - where isotopic inventories of the fuel assemblies become more constant (e.g., ^{235}U is nearly depleted and ^{239}Pu becomes nearly constant).

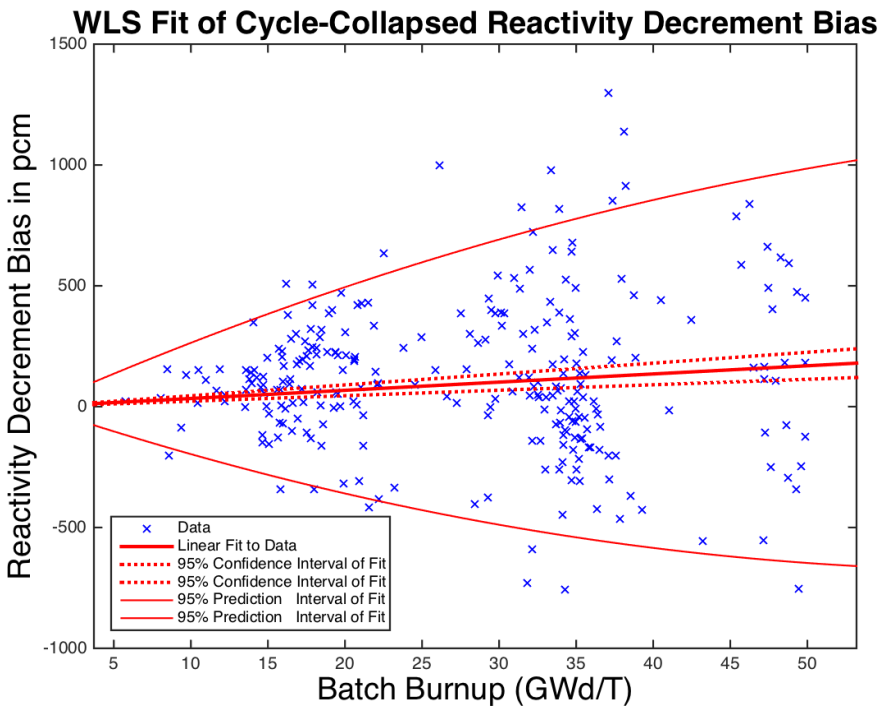

Figure 7-19
Reactivity Decrement Linear WLS Regression For Cycle-collapsed Data

The measured CASMO-5 biases in HFP reactivity decrement bias and 95% prediction interval half-width as a function of sub-batch burnup are presented in Table 7-1.

Table 7-1
Measured CASMO-5 HFP Reactivity Decrement Bias and Prediction Interval Half-Width

Burnup (GWd/T)	10.0	20.0	30.0	40.0	50.0	60.0
CASMO-5 Bias (pcm)	66	101	106	80	22	-64
Prediction Interval (pcm)	226	420	585	713	812	875

In order for the prediction interval data to be confidently used to construct a formal tolerance limit for the measured reactivity decrement biases, the regression residuals displayed in Figure 7-18 must be normally distributed. In order to test for normality, the standardized residuals (differences between the data points and the quadratic regression fit divided by the square root of the variance of each data point) were used in a Shapiro-Wilk test (using the StatPlus as add-on to Excel) to determine if the data "pass the normality test." As can be seen from the results in Figure 7-20, the residuals pass the Shapiro-Wilk normality test, as well as the Kolmogorov-Smirnov/Lilliefor and D'Agostino normality tests.

Normality Tests

Variable #1 (Reactivity Decrement Bias Residuals)

Sample Size	270	*Mean*	8.82425
Standard Deviation	225.28857	*Median*	0.
Skewness	0.01589	*Kurtosis*	2.74747
Skewness (Fisher's)	0.01598	*Kurtosis (Fisher's)*	-0.23471

	Test Statistics	*p-level*	*Conclusion: (5%)*
Kolmogorov-Smirnov/Lilliefor Test	0.02319	0.97833	*No evidence against normality*
Shapiro-Wilk W	0.99461	0.45792	*Accept Normality*
D'Agostino Skewness	0.10939	0.91289	*Accept Normality*
D'Agostino Kurtosis	-0.78382	0.43315	*Accept Normality*
D'Agostino Omnibus	0.62633	0.73113	*Accept Normality*

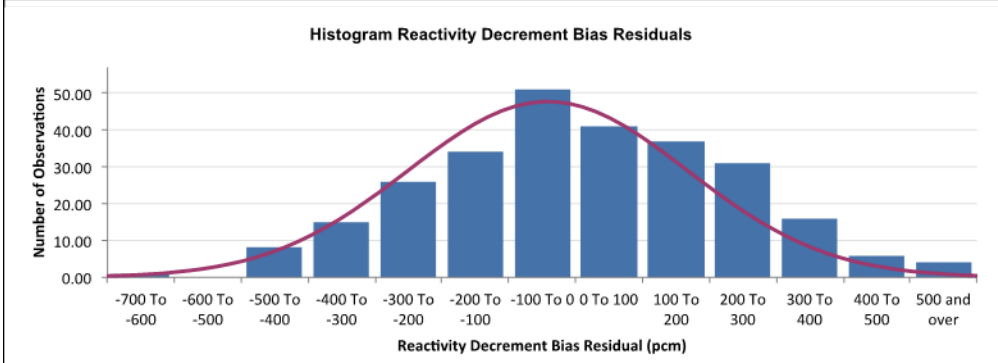

Figure 7-20
Normality Tests of Cycle-Collapsed WLS Regression Residuals

The important point to recall here is that because the sub-batch/cycle data points having been compressed to a single value, there are no correlation effects between successive flux map measurement points to be considered. Consequently, the regression prediction interval widths can be justifiably used - since the residuals correspond to a normal distribution, a condition that is needed for inferring the 95% prediction intervals for the regression fits.

The prediction interval is not the final quantity used to determine the HFP uncertainty of the measured reactivity decrement bias. Rather, we seek a 95/95 tolerance limit on the measured biases, and a tolerance limit factor must be applied to the prediction interval half-widths. With 270 data points in the regression fit, the 2-sided 95/95 tolerance limit factor is 1.074 (e.g. k_2=2.114) for a 95% Student's t-value of 1.969. However, for our intended application, it is more appropriate to use a 1-sided 95/95 tolerance limit because one need not be concerned with data outside the 95/95 band in the conservative direction. The 1-sided 95/95 tolerance limit factor for 270 data points is 0.918 (e.g. k_1=1.807). Table 7-2 displays the final HFP reactivity decrement bias tolerance limits which are ~8% less than the prediction interval half-widths.

Table 7-2
Measured CASMO-5 HFP Reactivity Decrement Bias and Tolerance Limit

Burnup (GWd/T)	10.0	20.0	30.0	40.0	50.0	60.0
CASMO-5 Bias (pcm)	66	101	106	80	22	-64
Prediction Interval two-sided (pcm)	226	420	585	713	812	875
95/95 Tolerance Limit one-sided (pcm)	207	386	537	655	745	803

7.7 Boron and Cycle Burnup Sensitivities

Another cross check of the accuracy of the decrement biases deduced from flux map data is to compare the BOC to EOC trends from the flux map data with the mean changes in measured boron bias from BOC to EOC. Such a comparison is presented in Table 7-3 for each of the four Duke Energy Plants - assuming a core-average burnup of 10 GWd/T at BOC and 30 GWd/T at EOC and a conversion from boron error to pcm using an assumed value of 9.0 pcm/ppm. These data show that the mean flux map reactivity decrements agree within 194 pcm (i.e., 234 pcm – 40 pcm) of the measured boron bias changes for each of the four reactors.

Table 7-3
Measured CASMO-5 BOC to EOC Reactivity Decrements

Unit	Reactor Boron Bias (pcm @ 9 pcm/ppm)			Flux Map Decrement Bias (pcm)		
	BOC (ppm)	EOC (ppm)	BOC-EOC (pcm)	10 GWd/T	30 GWd/T	30-10 GWd/T
McGuire 1	-4	-30	234	66	106	40
McGuire 2	-10	-32	198	66	106	40
Catawba 1	13	5	72	66	106	40
Catawba 2	30	14	144	66	106	40
		Mean	**162**			

All differences between measured boron reactivity decrement changes and measured flux map measured reactivity decrement changes are well within HFP reactivity decrement bias tolerance limits of Table 7-2.

7.8 Sensitivity to Lattice and Nodal Codes

Additional tests have been performed to demonstrate that CASMO-5 and SIMULATE-3 do not contribute significantly to the measured reactivity decrements. First, one should be able to use any modern lattice code/cross section library and core analysis tool to produce high quality measured reactivity

decrement benchmarks that are expected to lie within the range of assigned uncertainties of the EPRI benchmarks. There are several additional studies that have been done to add quantification to this argument. In their respective M.S. thesis, Gunow and Sykora [22-24] each used full-core multigroup neutron transport calculations to infer reactivity decrement biases for selected flux maps and sub-batches using the BEAVRS benchmark measured reactor data [25-26]. Both of these studies showed that the inferred reactivity decrements (see Table 6-2 in Reference 24, reproduced here as Table 7-4) were nearly the same when using SIMULATE-3 (two-group nodal diffusion calculations) and CASMO-5 (35-group, fine-mesh, transport calculations) to perform the core analysis. Thus, it is unlikely that any of the nodal model approximations have significantly influenced the inferred reactivity decrements of the original EPRI report [5]. These tests rule out any significant influence from core analysis approximations; such as lattice boundary conditions, two-group theory, assembly homogenization, macroscopic depletion, and pin power reconstruction.

Sykora's analysis [23] also showed that the burnup perturbation used to perform the k-infinity search in the EPRI methodology produced nearly identical reactivity decrements as using fuel temperature perturbations. This further substantiated the expectation that k-infinity itself dominates changes in core flux distribution, and the method by which the k-infinity perturbation is performed is not very important. Note from Table 7-4 results that the mean reactivity differences and 2-sigma deviations (for nodal diffusion vs. multi-group transport or burnup vs. temperature perturbation) are less than the tolerance limits assigned the measured reactivity decrements.

Another demonstration of the insensitivity of inferred reactivity decrement biases to the core analysis methods employed was obtained from studies done by R. D. Harrison in the UK [27-28]. This analysis followed the EPRI methodology, but used the JEF2.2 rather than the ENDF-B/VII nuclear data library and the WIMS/PANTHER codes rather than the CASMO-5/SIMULATE-3 codes of the EPRI report. These studies produced reactivity decrement biases and uncertainties that are very similar to those of the Sykora's study [23, 24], further substantiating that the data library and nodal codes do not contribute significantly to the decrement biases and uncertainties.

The original version of this report [5] also contained direct comparisons of reactivity decrement biases inferred using the CASMO-4 lattice code [8]. The CASMO-4 cross section library uses a combination of ENDF-B/V and JEF 2.0 nuclear cross section data, and yet the measured reactivity decrements biases are very close to those inferred using CASMO-5 data, and they are also well within the assigned measurement uncertainties.

These tests have all demonstrated that CASMO-5 lattice approximations and the SIMULATE-3 nodal approximations do not directly contribute significantly to the measured reactivity decrements or its uncertainty.

Table 7-4
Inferred CASMO-5 Fuel Batch Reactivity Biases

Fuel Assembly Reactivity Decrement Biases for BEAVRS Cycle 1 and Cycle 2 (CASMO-5 with ENDF-B/VII)								
Cycle	**Enrichment**	**Cycle Burnup**	**Fuel Burnup**	**SIMULATE Bias (burnup pert.) Δk**	**CASMO Bias (burnup pert.) Δk**	**CASMO Bias (temp. pert.) Δk**	**SIMULATE - CASMO Bias (burnup pert.)**	**Bias Difference (burnup pert. - temp. pert.)**
	%	GWd/T	GWd/T	pcm	pcm	pcm	pcm	pcm
1	2.4	2.16	2.44	-215	-251	-182	36	-69
1	2.4	6.49	7.39	66	66	90	0	-24
1	2.4	11.08	12.62	-50	-50	-63	0	13
2	2.4	3.20	18.10	90	119	-30	-29	149
2	2.4	6.52	20.88	-347	-230	-369	-117	139
2	2.4	9.36	23.29	-197	-167	-302	-30	135
1	3.1	2.16	1.87	60	222	198	-162	24
1	3.1	6.49	5.53	0	0	0	0	0
1	3.1	11.08	9.52	14	14	0	0	14
2	3.1	3.20	15.43	432	255	300	177	-45
2	3.1	6.52	19.09	160	72	132	88	-60
2	3.1	9.36	22.17	198	119	65	79	54
2	3.2 / 3.4	3.20	3.29	-328	-242	-243	-86	1
2	3.2 / 3.4	6.52	6.81	-54	0	-61	-54	61
2	3.2 / 3.4	9.36	9.85	-75	0	-62	-75	62
1	3.1 @ 2.4_{min}	2.16	2.15	0	182	66	-182	116
1	3.1 @ 2.4_{min}	6.49	6.46	100	70	0	30	70
1	3.1 @ 2.4_{min}	11.08	11.07	0	14	0	-14	14
			S.D. of Bias	188	152	169	88	67
			Mean Bias	-8	11	-26	-19	36

Section 8: Measured Cold Reactivity Bias and Uncertainty

The SIMULATE-3 flux map analysis procedure described in Sections 6 and 7 allowed quantification of the bias and uncertainty in CASMO-5 reactivity decrements at HFP conditions. However, for spent fuel pool and cask criticality analyses, biases and uncertainties are needed at cold conditions.

8.1 Overview

The biases and uncertainties at HFP include errors associated with both the assembly isotopics and cross-section data uncertainties. At cold conditions (before cooling) the isotopics do not change, but there are additional uncertainties from the altered conditions. Two such sources of added uncertainty arise because of:

1) imprecise knowledge of exact physical properties (for example, fuel temperature, coolant temperature, boron concentration) during fuel irradiation, and

2) spectrum-induced reactivity changes from HFP to cold conditions from cross-section data uncertainties.

8.2 Fuel Temperature Uncertainties

At SFP or cask conditions, coolant temperature, fuel temperature and boron concentrations are all well known. At HFP conditions coolant temperatures and boron concentrations are well known, and they do not depend in any direct way on sub-batch burnups. However, fuel temperatures are not as easy to compute accurately. Fuel conductivity decreases about 50% at high burnup, and pellet swelling and gap conductance changes cause fuel temperatures to change with pellet burnup. The net effect is that there is an added uncertainty in measured reactivity decrements because of imperfect knowledge of HFP fuel temperatures.

This situation is easiest to understand by assuming that one has a lattice code that computes HFP sub-batch reactivities with zero bias – for all burnups. If there are any errors in HFP fuel temperatures, the corresponding reactivity bias must be cancelled out by other biases in the lattice code reactivities at HFP conditions. Consequently, there are uncertainties in measured HFP reactivity decrements that arise from imperfect knowledge of fuel temperatures at operating

reactor conditions. In addition, even though SFP temperatures might be known exactly, the history (e.g., depletion) effects of fuel temperature errors also contribute additional uncertainties in lattice code reactivities at cold conditions.

There is no easy way to quantify precisely the fuel temperature reactivity decrement uncertainty change from HFP to cold conditions. The INTERPIN-4 plot of fuel temperature vs. burnup displayed in Figure 8-1 shows that predicted fuel temperatures decrease by about 50K as the pellet swells, the cladding creeps down, and as the pellet/cladding gap closes. At high burnup, the decrease in fuel conductivity overwhelms the gap conductance changes, and fuel temperatures increase significantly.

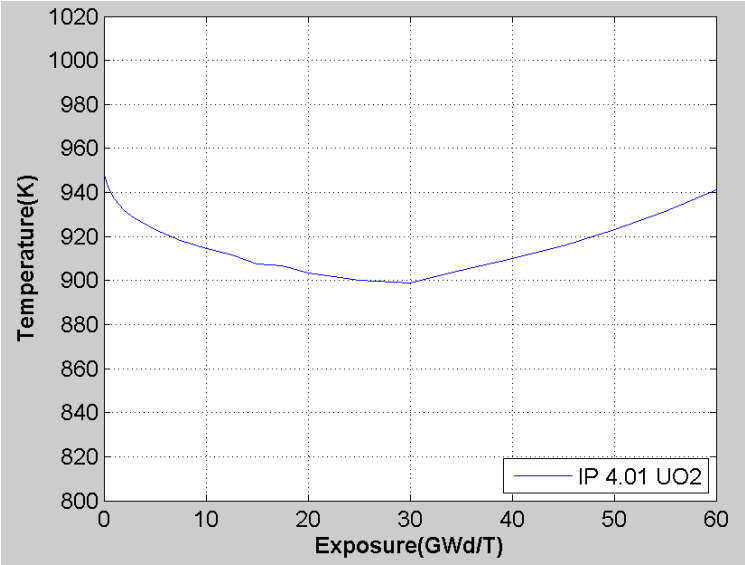

Figure 8-1
Typical INTERPIN-4 Fuel Temperature Change With Burnup

One way to conservatively treat uncertainties in fuel temperatures on HFP and cold reactivities is to treat the entire reactivity effect as additional uncertainties. By taking the highest and lowest fuel temperatures that occur anywhere in the nominal INTERPIN-4 predictions (4.75% enriched Westinghouse RFA fuel) and performing CASMO-5 calculations with these fixed temperatures, one obtains the table of reactivity differences presented in Table 8-1. These results show that at hot conditions, the instantaneous decrease in reactivity for the higher fuel temperature is partially compensated at high burnup by the production of additional plutonium, with the cumulative effect being almost zero at 55 GWd/T. However, in the branch cases to cold conditions, the higher HFP fuel temperature leads to a monotonic increase in lattice reactivity. These results show that the maximum difference reactivities are -150 pcm at HFP conditions and +206 pcm at cold conditions.

In the initial version of this EPRI report [5] a very conservative approach to the fuel temperature uncertainty was taken by statistically combining the maximum instantaneous fuel temperature difference (150 pcm) and the maximum historical

fuel temperature difference (206 pcm) to arrive at a combined fuel temperature uncertainty of 255 pcm – that was then applied independent of burnup. This approach leads to an extremely conservative uncertainty for low burnups, because the reactivity decrement uncertainty must physically go to 0.0 pcm at zero burnup. Consequently, it is more appropriate to statistically combine the two fuel temperature uncertainties at each burnup to obtain a more realistic uncertainty as a function of burnup. The right-most column of Table 8-1 displays the combined fuel temperature **uncertainty as a function of burnup** expressed in pcm. At 10.0 GWd/T, the uncertainty is reduced to 146 pcm rather than the conservative 255 pcm previously used in the initial EPRI report [5].

Table 8-1
Fuel Temperature Effect on Hot and Cold Lattice Reactivity

Burnup (GWd/T)	Hot Depletion (HFP)			Branch to Cold (Bor=0, Xen=0, 293K)			Statistically Combined Uncertainty (pcm)
	k-infinity (946K)	k-infinity (897K)	Difference 946K-897K	k-infinity (946K)	k-infinity (897K)	Difference 946K-897K	
0.0	1.07712	1.07848	-0.00136	1.15285	1.15285	+0.00000	136
10.0	1.13346	1.13492	-0.00146	1.20192	1.20189	+0.00003	146
20.0	1.13467	1.13617	-0.00150	1.21248	1.21229	+0.00019	151
30.0	1.08533	1.08650	-0.00117	1.16481	1.16421	+0.00060	131
40.0	1.02515	1.02586	-0.00071	1.09975	1.09866	+0.00109	130
50.0	0.96862	0.96887	-0.00025	1.03605	1.03445	+0.00160	162
60.0	0.91905	0.91888	+0.00017	0.97875	0.97669	+0.00206	207

8.3 Cold Uncertainty Change From Cross-Section Uncertainties

The TSUNAMI-3D sequence in ORNL's SCALE 6 [29] code system can be used in conjunction with CASMO-5 to characterize uncertainties in hot to cold reactivity changes due to cross-section uncertainty at various burnup points. The goal of the analysis is to establish the multiplication factor uncertainty between various fuel assemblies at different conditions in a quantifiable manner and to obtain a bound on the hot-to-cold reactivity uncertainty over the various assembly types and burnups – attributed to cross-section data uncertainties.

The TSUNAMI analysis sequences are capable of estimating the impact of cross-section uncertainties in a critical system's multiplication factor k by propagating uncertainties through the use of sensitivity coefficients and first-order perturbation theory. The sensitivity coefficients represent a change in the system's response due to a change in the input parameters. In particular, TSUNAMI approach uses explicit $(S_{k,\Sigma x,g})$ and implicit $(S_{\Sigma x,g,\omega_i})$ sensitivity coefficients, which are defined in the following manner.

$$S_{k,\Sigma_{x,g}} = \frac{\Sigma_{x,g}}{k}\frac{\partial k}{\partial \Sigma_{x,g}}$$

$$S_{\Sigma_{x,g},\omega_i} = \frac{\omega_i}{\Sigma_{x,g}} \frac{\partial \Sigma_{x,g}}{\partial \omega_i},$$

where $\Sigma_{x,g}$ is the macroscopic cross-section for reaction *x* and group *g*, and ω_i is the nuclear data component of some isotope *i*. The implicit sensitivity coefficient is propagated to *k* or explicit sensitivity through the use of the chain rule for derivatives. The sensitivity coefficients are summed so that they account for the fact that changes in one cross section may affect another cross section via self-shielding perturbations. Finally, the response uncertainty is obtained by summing all the contributions to the system response from the uncertainties through the sensitivity coefficients and covariance data.

In addition to computing uncertainties in the multiplication factor, the SCALE 6 code system is capable of computing a correlation coefficient, which is representative of the similarity (in terms of uncertainty) between two critical systems. The computation of the correlation coefficient is performed by the TSUNAMI-IP sequence in SCALE 6, which uses the sensitivity data generated by TSUNAMI, along with nuclear covariance data to assess the similarity between the two systems.

8.4 TSUNAMI Uncertainty Analysis

CASMO-5 was used to perform the lattice depletion and branch calculations for a variety of fuel assemblies. In order to obtain the burnup-dependent isotopic compositions in each fuel and burnable rod for the TSUNAMI-3D calculation, a script was developed which used the CASMO-5 lattice geometry, temperature, and region-wise isotopic composition to generate suitable SCALE 6 input files. This process was applied to all lattice types and branch conditions for selected burnup points.

A 17 x 17 Westinghouse RFA fuel assembly with 5% enrichment, 104 IFBA, and 20 WABA was selected as a base case. A case matrix was constructed for different enrichments (3.5 % and 4.25 %), number of burnable absorbers (128 IFBA, 24 WABA), and fuel pin radius (smaller than nominal) for a total of five lattice cases. All five lattice cases were depleted with CASMO-5 to 60 GWd/T and "branched" from HFP to six other conditions (HFP No Xenon, Hot Zero Power, Cold 1000 ppm boron, Cold no boron, Cold no boron with 100-hour decay, and simplified rack geometry) at eight burnup points (0.0, 0.5, 10, 20, 30, 40, 50, and 60 GWd/T).

Since the covariance library in SCALE-6 is in multi-group format, the TSUNAMI-3D sequence uses the unresolved (BONAMIST) and resolved resonance self-shielding modules (NITAWLST or CENTRMST) to produce problem-specific multi-group cross-section and sensitivity libraries for the multi-group transport calculation. Cross-sections in each fuel pin region (with unique isotopic number densities) were self-shielded in the TSUNAMI calculation. In order to reduce the run-time, the NITAWLST module was used to perform the resolved resonance self-shielding calculation that necessitated the use of the 238-

group ENDF/B-V library. Forward and adjoint multi-group transport calculations in TSUNAMI-3D are performed by the KENO multi-group Monte Carlo code. Finally, the TSUNAMI-3D KENO-VI sequence was chosen to take advantage of the ¼ assembly geometry symmetry. Once forward and adjoint transport computations were completed, the SAMS module was used to generate problem-specific uncertainty data and a sensitivity library to be used for post-processing. This library is read by TSUNAMI-IP to generate correlation coefficients. The specific versions of SCALE-6 that were used in this analysis were:

- tsunami-3d_k6 6.0.34 p07_jan_2009
- bonamist 6.0.21 p09_jan_2009
- nitawlst 6.0.16 p30_dec_2008
- kenovi 6.0.24 p07_jan_2009
- sams6 6.0.29 p07_jan_2009
- tsunami-ip 6.0.13 p30_dec_2008

8.5 TSUNAMI Analysis Results

TSUNAMI can compute cross-section uncertainties for lattice multiplication factors as a function of various lattices, conditions, and burnups. The uncertainty results for the base lattice at HFP and cold conditions as a function of burnup are shown in Table 8-2.

Table 8-2
Multiplication Factor Uncertainty (2-sigma) as Function of Burnup

Burnup (GWd/T)	0.5	10.	20.	30.	40.	50.	60.
k-infinity Hot	1.02068	1.08597	1.08298	1.03600	0.97772	0.92176	0.87200
Uncertainty (pcm)	1034	1104	1211	1265	1295	1311	1323
k-infinity Cold	1.16103	1.23579	1.25419	1.21057	1.14557	1.07995	1.01883
Uncertainty (pcm)	1015	1087	1209	1281	1326	1361	1388

The hot-to-cold reactivity uncertainties can be obtained from the data shown above and the correlation coefficient obtained from evaluation of the covariance matrix between the two states. The results from this analysis are shown in Table 8-3. The propagation of uncertainties as independent variables (without correlation) is also shown to illustrate the importance of the correlation between hot-to-cold conditions on the uncertainty.

Table 8-3
HFP to Cold Reactivity Uncertainty (2-sigma) as Function of Burnup

Burnup (GWd/T)	0	0.5	10.	20.	30.	40.	50.	60.
Uncertainty (pcm)	347	427	459	508	527	530	521	509
Uncertainty (pcm)*	1479	1476	1580	1748	1840	1893	1926	1949
* Propagation of uncertainty such that the covariance (k-hot, k-cold)=0								

The inclusion of the correlation reduces the uncertainty by about a factor of four. The two states are expected to be highly correlated due to the fact that there is no burnup difference, and isotopic compositions remain the same.

For any lattice and depletion point, the similarity between different physical conditions can be quantified by the use of the correlation coefficient. A correlation coefficient of unity indicates perfect similarity (identical systems) while a correlation of zero indicates negligible similarity. In this analysis, the correlation factor shows the similarity between different states and lattice types at a fixed burnup step.

A summary of the correlation coefficients is shown in Table 8-4 for the five lattice types between nominal (HFP) and branch conditions. The first row in each lattice type is unity because HFP is the base case. **All lattices show a very high degree of similarity between HFP and various cold conditions, at all burnup points** – even though xenon, fuel temperature, coolant temperature, boron concentration, and local rack conditions change dramatically. (For the rack case, a simplified uniform rack has been assumed with a pitch of 22.5 cm, a 0.1-cm thick stainless steel can, a 0.0625-cm thick borated aluminum poison sheet having a width of 19 cm, and a ^{10}B areal density of 0.006 gm/cm^2.)

A second comparison between different lattice types was performed at HFP, cold (no boron, 100-hour decay), and cold rack conditions, and results are presented in Tables 8-5 and 8-6. In Table 8-5, all correlation coefficients are computed relative to the base case at zero burnup. It can be seen that the similarity changes significantly with burnup as the isotopics of the fuel change from fresh uranium to the higher actinides and fission products. Table 8-6 displays the correlation coefficients for the same cases measured relative to the base case at each burnup state. These results indicate **an extremely high degree of similarity exists between all lattice types – at each burnup point**. This is important for this project, as biases in reactivity decrement as a function of burnup are derived directly from reactor measurements, and only the uncertainty of going from HFP reactor conditions to cold spent fuel pool/cask conditions is needed from the TSUNAMI analysis.

Finally, the quantities of direct interest in this study, reactivity and reactivity uncertainty between HFP and cold (no boron, 100-hour decay) are displayed in Table 8-7, for all lattice types. The data in Table 8-7 are not taken directly from TSUNAMI outputs, but rather they are based on the eigenvalue and uncertainty calculated by TSUNAMI at Hot Full Power (HFP) and cold conditions. The

state or condition eigenvalue and uncertainty are taken directly from the TSUNAMI output files. In order to obtain the 2-sigma uncertainties in Report Tables 8-7, the variance of the reactivity is obtained by computing the relative variance of the eigenvalue difference (see Eq. (41) paper in Reference [30]). The relative standard deviation of the hot-to-cold reactivity is obtained from the following equation, which is based on Eq. (41) of the referenced paper after some manipulations,

$$\sigma_\rho = \frac{1}{\rho_{h\to c}}\sqrt{\left(\frac{\sigma_{k_h}}{k_h}\right)^2 + \left(\frac{\sigma_{k_c}}{k_c}\right)^2 - 2C_{h,c}\frac{\sigma_{k_h}\sigma_{k_c}}{k_h k_c}},$$

where k and σ_k are the eigenvalue and standard deviation, respectively, $C_{h,c}$ is the correlation coefficient, and $\rho_{h\to c}$ is the reactivity, defined as follows

$$\rho_{h\to c} = \frac{1}{k_h} - \frac{1}{k_c}$$

Finally, the absolute two-sigma uncertainties are obtained by multiplying the relative standard deviation by the hot-to-cold reactivity and accounting for the fact that two standard deviations account for 95.45 % of values around a mean.

The maximum 2-sigma reactivity uncertainty (due to cross-section data uncertainties) over all lattice types and burnup points is 555 pcm. Table 8-8 displays the corresponding reactivity and reactivity uncertainty between HFP and cold simplified SFP rack conditions. The uncertainties displayed in Table 8-8 are uniformly lower than those in Table 8-7, indicating that the cross-section data uncertainties are less important in the SFP absorbing rack geometry. This is a reflection of the fact that the hardening of the spectrum caused by the SFP rack actually makes the spectrum closer to the lattice spectrum at HFP conditions than to the lattice spectrum at cold conditions. Consequently, the **impacts of cross section uncertainties on the reactivity changes from HFP-to-cold conditions are very similar in operating reactor conditions and cold rack geometry.**

Table 8-4
Correlation Coefficients, c_k, Between Reactor Conditions by Lattice and Burnup

		Burnup (GWd/T)							
		0.0	**0.5**	**10.0**	**20.0**	**30.0**	**40.0**	**50.0**	**60.0**
Base	HFP	1	1	1	1	1	1	1	1
	HFP No Xe	1	0.9843	0.9817	0.9831	0.9854	0.9878	0.9898	0.9914
	HZP	0.9992	0.9992	0.9992	0.9995	0.9994	0.9994	0.9995	0.9995
	Cold 1000 ppm	0.9807	0.9609	0.9608	0.9646	0.9678	0.9702	0.9723	0.9734
	Cold 0 ppm	0.9694	0.9506	0.9514	0.9560	0.9592	0.9611	0.9634	0.9640
	Decay 100 hr	0.9705	0.9512	0.9519	0.9558	0.9591	0.9613	0.9633	0.9643
	SNF Rack	0.9717	0.9543	0.9510	0.9543	0.9582	0.9605	0.9623	0.9641
128 IFBA 24 WABA	HFP	1	1	1	1	1	1	1	1
	HFP No Xe	1	0.9863	0.9829	0.9835	0.9856	0.9879	0.9899	0.9914
	HZP	0.9993	0.9993	0.9992	0.9993	0.9994	0.9994	0.9995	0.9994
	Cold 1000 ppm	0.9799	0.9638	0.9616	0.9648	0.9677	0.9703	0.9724	0.9734
	Cold 0 ppm	0.9708	0.9526	0.9525	0.9558	0.9587	0.9617	0.9638	0.9643
	Decay 100 hr	0.9702	0.9548	0.9531	0.9559	0.9585	0.9614	0.9634	0.9641
	SNF Rack	0.9725	0.9559	0.9518	0.9547	0.9572	0.9611	0.9630	0.9638
3.5% Enrichment	HFP	1	1	1	1	1	1	1	1
	HFP No Xe	1	0.9851	0.9828	0.9853	0.9884	0.9907	0.9923	0.9934
	HZP	0.9994	0.9992	0.9993	0.9984	0.9996	0.9995	0.9994	0.9995
	Cold 1000 ppm	0.9799	0.9617	0.9637	0.9675	0.9714	0.9726	0.9738	0.9744
	Cold 0 ppm	0.9670	0.9482	0.9521	0.9569	0.9603	0.9622	0.9631	0.9641
	Decay 100 hr	0.9669	0.9482	0.9526	0.9566	0.9608	0.9622	0.9632	0.9639
	SNF Rack	0.9734	0.9565	0.9538	0.9572	0.9612	0.9630	0.9641	0.9649

Table 8-4 (continued)
Correlation Coefficients, c_k, Between Reactor Conditions by Lattice and Burnup

		Burnup (GWd/T)							
		0.0	**0.5**	**10.0**	**20.0**	**30.0**	**40.0**	**50.0**	**60.0**
4.25% Enrichment	HFP	1	1	1	1	1	1	1	1
	HFP No Xe	1	0.9842	0.9818	0.9838	0.9867	0.9891	0.9910	0.9924
	HZP	0.9994	0.9993	0.9995	0.9995	0.9995	0.9995	0.9995	0.9995
	Cold 1000 ppm	0.9808	0.9617	0.9618	0.9659	0.9698	0.9718	0.9734	0.9740
	Cold 0 ppm	0.9700	0.9504	0.9512	0.9558	0.9598	0.9625	0.9636	0.9641
	Decay 100 hr	0.9696	0.9490	0.9524	0.9565	0.9602	0.9622	0.9636	0.9639
	SNF Rack	0.9730	0.9547	0.9517	0.9560	0.9596	0.9624	0.9640	0.9645
Small Fuel Pin	HFP	1	1	1	1	1	1	1	1
	HFP No Xe	1	0.9816	0.9781	0.9797	0.9827	0.9857	0.9882	0.9904
	HZP	0.9992	0.9992	0.9994	0.9995	0.9995	0.9996	0.9996	0.9996
	Cold 1000 ppm	0.9814	0.9608	0.9589	0.9618	0.9652	0.9690	0.9712	0.9728
	Cold 0 ppm	0.9709	0.9498	0.9488	0.9521	0.9556	0.9591	0.9616	0.9628
	Decay 100 hr	0.9709	0.9510	0.9497	0.9530	0.9555	0.9596	0.9614	0.9630
	SNF Rack	0.9743	0.9536	0.9486	0.9513	0.9548	0.9590	0.9615	0.9632

Table 8-5
Correlation Coefficients, c_k, Between Lattice Types (Relative to 0 GWd/T)

		Burnup (GWd/T)							
		0.0	**0.5**	**10.0**	**20.0**	**30.0**	**40.0**	**50.0**	**60.0**
HFP	Base	1	0.9837	0.8321	0.6849	0.5867	0.5149	0.4567	0.4100
	128 I 24 W	0.9989	0.9838	0.8292	0.6827	0.5869	0.5147	0.4571	0.4115
	3.5 % Enrich.	0.9927	0.9754	0.7323	0.5779	0.4879	0.4265	0.3817	0.3490
	4.25 % Enrich.	0.9985	0.9812	0.7886	0.6346	0.5390	0.4705	0.4176	0.3777
	Small Fuel Rad.	0.9976	0.9797	0.8280	0.6804	0.5827	0.5062	0.4461	0.3964
Cold 0 ppm Decay 100 hr	Base	1	0.9991	0.8569	0.7016	0.5857	0.4936	0.4177	0.3554
	128 I 24 W	0.9988	0.9977	0.8509	0.6959	0.5823	0.4916	0.4168	0.3556
	3.5 % Enrich.	0.9941	0.9920	0.7562	0.5798	0.4648	0.3805	0.3186	0.2738
	4.25 % Enrich.	0.9988	0.9974	0.8149	0.6468	0.5293	0.4386	0.3675	0.3123
	Small Fuel Rad.	0.9979	0.9976	0.8661	0.7172	0.6015	0.5070	0.4266	0.3594
SNF Rack Geometry	Base	1	0.9992	0.8505	0.6890	0.5716	0.4792	0.4032	0.3422
	128 I 24 W	0.9988	0.9981	0.8446	0.6836	0.5675	0.4780	0.4034	0.3424
	3.5 % Enrich.	0.9940	0.9920	0.7466	0.5643	0.4488	0.3650	0.3037	0.2599
	4.25 % Enrich.	0.9988	0.9975	0.8065	0.6326	0.5138	0.4241	0.3534	0.2989
	Small Fuel Rad.	0.9984	0.9976	0.8582	0.7022	0.5854	0.4906	0.4112	0.3444

Table 8-6
Correlation Coefficients, c_k, Between Lattice Types (By Individual Burnup State)

		Burnup (GWd/T)							
		0.0	**0.5**	**10.0**	**20.0**	**30.0**	**40.0**	**50.0**	**60.0**
HFP	Base	1	1	1	1	1	1	1	1
	128 I 24 W	0.9989	0.9990	0.9998	0.9999	0.9999	1	1	1
	3.5 % Enrich.	0.9927	0.9931	0.9831	0.9870	0.9898	0.9919	0.9939	0.9958
	4.25 % Enrich.	0.9985	0.9984	0.9963	0.9969	0.9976	0.9980	0.9984	0.9988
	Small Fuel Rad.	0.9976	0.9975	0.9971	0.9977	0.9983	0.9979	0.9981	0.9982
Cold 0 ppm Decay 100 hr	Base	1	1	1	1	1	1	1	1
	128 I 24 W	0.9988	0.9986	0.9997	0.9999	1	1	1	1
	3.5 % Enrich.	0.9941	0.9939	0.9818	0.9836	0.9860	0.9885	0.9912	0.9937
	4.25 % Enrich.	0.9988	0.9987	0.9962	0.9963	0.9968	0.9972	0.9977	0.9983
	Small Fuel Rad.	0.9979	0.9982	0.9978	0.9981	0.9982	0.9984	0.9984	0.9985
SNF Rack Geometry	Base	1	1	1	1	1	1	1	1
	128 I 24 W	0.9988	0.9992	0.9997	0.9999	1	1	1	1
	3.5 % Enrich.	0.9940	0.9941	0.9817	0.9835	0.9860	0.9884	0.9910	0.9936
	4.25 % Enrich.	0.9988	0.9988	0.9961	0.9963	0.9968	0.9972	0.9977	0.9982
	Small Fuel Rad.	0.9984	0.9980	0.9977	0.9979	0.9982	0.9983	0.9986	0.9985

Table 8-7
HFP to Cold Uncertainty Matrix (2-sigma) at Cold Conditions

		Burnup (GWd/T)							
		0.0	**0.5**	**10.0**	**20.0**	**30.0**	**40.0**	**50.0**	**60.0**
Base	Reactivity (pcm)	9867	11843	11425	12605	13919	14986	15891	16527
	Uncertainty	347	427	459	508	527	530	521	509
128 IFBA 24 WABA	Reactivity (pcm)	9977	11927	11367	12556	13916	15009	15888	16612
	Uncertainty	337	403	450	508	533	531	521	512
3.50% Enrichment	Reactivity (pcm)	12703	14810	13078	14402	15525	16266	16734	17034
	Uncertainty	365	437	498	555	550	537	518	500
4.25% Enrichment	Reactivity (pcm)	11069	13112	12209	13469	14747	15699	16415	16931
	Uncertainty	350	434	473	529	540	534	520	508
Small Fuel Pin	Reactivity (pcm)	10205	12262	11602	12658	13981	14991	15849	16473
	Uncertainty	322	402	442	497	524	518	509	492

Table 8-8
HFP to Cold Uncertainty Matrix (2-sigma) in Rack Geometry

		Burnup (GWd/T)							
		0.0	**0.5**	**10.0**	**20.0**	**30.0**	**40.0**	**50.0**	**60.0**
Base	Reactivity (pcm)	-10145	-8018	-6291	-4658	-4002	-4097	-4601	-5344
	Uncertainty	222	287	324	353	358	356	349	339
128 IFBA 24 WABA	Reactivity (pcm)	-10405	-8323	-6684	-4858	-4094	-4130	-4626	-5347
	Uncertainty	212	274	317	352	364	354	346	341
3.50% Enrichment	Reactivity (pcm)	-12437	-9905	-7382	-5715	-5839	-6687	-7688	-8688
	Uncertainty	204	266	330	364	357	349	343	337
4.25% Enrichment	Reactivity (pcm)	-11101	-8772	-6740	-5028	-4684	-5123	-5916	-6873
	Uncertainty	211	279	327	357	359	350	342	337
Small Fuel Pin	Reactivity (pcm)	-10594	-8366	-6705	-5185	-4676	-5046	-5851	-7075
	Uncertainty	201	274	315	348	356	345	336	327

8.6 HFP to Cold Reactivity Decrement Uncertainty

Since the uncertainty changes in Table 8-8 may be dependent on the actual rack design, it is conservative to use the uncertainties computed directly at cold conditions - without taking any credit for reduction in uncertainty that would arise in SFP or cask geometry.

However, the uncertainty for fresh fuel in cold SFP or cask conditions will actually be determined for specific applications through evaluation of a large set of cold criticals, and there is no reason to include reactivity uncertainty due to fresh fuel cross-section uncertainties. Consequently, statistically subtracting the smallest fresh fuel uncertainty (the green cell) from the other uncertainties in Table 8-7, one obtains the hot-to-cold reactivity uncertainties (due to cross-section uncertainties) as a function of fuel depletion as displayed in Table 8-9.

Table 8-9
HFP to Cold Additional Uncertainty Matrix (2-sigma in pcm) at Cold Conditions

	Burnup (GWd/T)							
	0.0	**0.5**	**10.0**	**20.0**	**30.0**	**40.0**	**50.0**	**60.0**
Base	0	249	300	371	397	401	389	372
128 IFBA/24 WABA	0	221	298	380	413	410	397	385
3.50% Enrichment	0	240	339	418	411	394	368	342
4.25% Enrichment	0	257	318	397	411	403	385	368
Small Fuel Pin	0	241	303	379	413	406	394	372

The top blue curve in Figure 8-2 displays a plot of the 128 IFBA/24 WABA lattice additional uncertainties as a function of burnup when referenced to zero burnup. The large jump from 0.0 to 0.5 GWd/T burnup occurs in part because of the ~3000 pcm reactivity arising from Xe^{135} in the HFP depleted lattices. Xenon must be present in both the hot and cold TSUNAMI cases to maintain consistency when computing Hot-to-Cold uncertainties. Note that the corresponding additional uncertainty curve does not approach 0.0 for low burnups as one expects from the definition of reactivity decrement.

An alternate interpretation of this data is to use the 0.5 GWd/T step as the reference for "zero" burnup, as displayed in the bottom red curve of Figure 8-2. This curve's shape trends towards 0.0 at zero burnup. With 0.5 GWd/T as the "zero" burnup reference, xenon is consistently represented in all data used to decompose the additional burnup uncertainty, as displayed in Table 8-10.

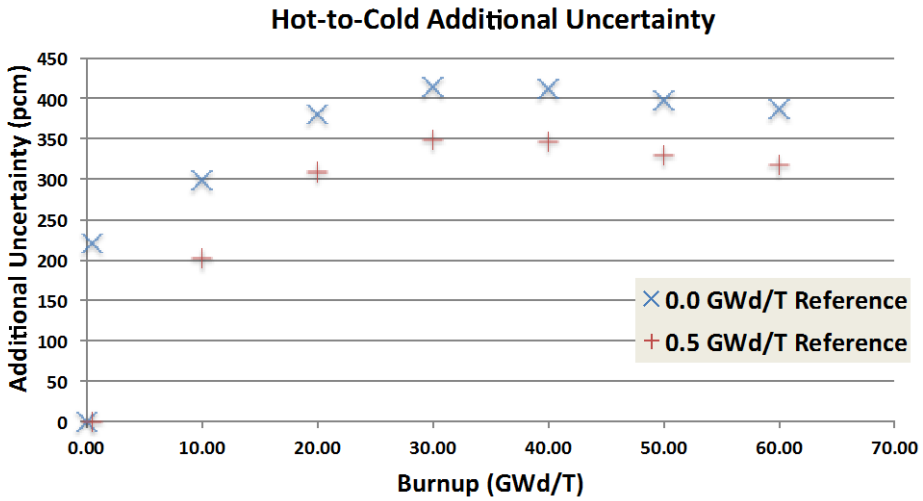

Figure 8-2
Hot-to-Cold Additional Uncertainty vs. Burnup

Table 8-10
HFP to Cold Additional Uncertainty Matrix (2-sigma in pcm) at Cold Conditions

	Burnup (GWd/T)							
	0.0	**0.5**	**10.0**	**20.0**	**30.0**	**40.0**	**50.0**	**60.0**
Base	-	0	168	275	309	314	299	277
128 IFBA/24 WABA	-	0	200	309	349	346	330	316
3.50% Enrichment	-	0	239	342	334	312	278	243
4.25% Enrichment	-	0	188	302	321	311	286	264
Small Fuel Pin	-	0	184	292	336	327	312	284

Consequently, we choose to use the maximum additional uncertainty from any of the five lattices of Table 8-10 (at each burnup step) as the appropriate hot-to-cold uncertainty versus burnup, as is displayed in the bottom row of Table 8-11.

Table 8-11
HFP to Cold Additional Uncertainty (2-sigma) vs. Burnup

Burnup (GWd/T)	0.0	10.0	20.0	30.0	40.0	50.0	60.0
Uncertainty (pcm)	0	239	342	349	346	330	316

8.7 Cold Reactivity Decrement Bias and Tolerance Limit

CASMO-5 does not have the ability to propagate nuclear cross section data uncertainties, so the SCALE 6 code system was used to perform such analyses. Fortunately both CASMO-5 and SCALE 6 employ the nuclear ENDF-B/VII cross section, and the cross section covariance and uncertainties from SCALE 6 are equally applicable to CASMO-5. Consequently, it is appropriate to assume that HFP-to-cold uncertainty changes computed with SCALE6 data are equally applicable to CASMO-5. Hence, one can statistically combine the HFP one-sided tolerance limits (from Table 7-2), the fuel temperature 2-sigma uncertainties (from Table 8-1), and the HFP to cold additional uncertainties (from Table 8-11) to obtain a one-sided total 95/95 tolerance limit. Appending this data to the bias data of Table 7-2 one obtains the measured CASMO-5 cold reactivity decrement biases and tolerance limits, as displayed in Table 8-12.

The last row of data in Table 8-12 adds the cold tolerance limit for fuel depleted at 150% of nominal power density; by assuming the fuel temperature uncertainty is linear in fuel temperature. The later data are appropriate for fuel that might be depleted at 150% of nominal power density, where the fuel temperature uncertainties are larger than those for fuel depleted at nominal power densities.

Table 8-12
Measured CASMO-5 Cold Reactivity Decrement Biases and Tolerance Limits

Burnup (GWd/T)	10.0	20.0	30.0	40.0	50.0	60.0
CASMO-5 Bias (pcm)	66	101	106	80	22	-64
Prediction Interval (pcm)	226	420	585	713	812	875
HFP Tolerance Limit (pcm)	207	386	537	655	745	803
Cold Tolerance Limit (pcm)	348	537	654	752	831	888
Cold Tolerance Limit (pcm)*	385	563	670	766	851	917

* Assuming 150% of nominal fuel temperature

Section 9: Experimental Reactivity Decrement Benchmarks

9.1 Experimental Benchmark Methodology

The analysis presented in Section 7 has quantified the measured CASMO-5 reactivity burnup decrement errors and has further demonstrated that these errors are essentially independent of sub-batch enrichment, boron concentrations, etc. Consequently, if one assumes the CASMO-5 biases in reactivity decrement are independent of fuel type (within the stated uncertainties), one can construct an experimental benchmark for HFP reactivity decrement by adding CASMO-5 biases to CASMO-5 computed reactivity decrements. **In such a benchmark, the net effect is that lattice physics depletion uncertainties, including nuclide concentration and reactivity uncertainties, are experimentally determined.**

Since nuclide inventories between HFP and cold (no cooling) conditions are identical, the only difference between HFP and cold arise from changes in fuel and coolant temperatures. The TSUNAMI analysis presented in Section 8 has demonstrated high similarity between all fuel types at HFP and cold conditions and has quantified the uncertainty changes from HFP-to-cold conditions. Thus, one obtains an experimental benchmark for cold reactivity decrement by adding the additional uncertainties that arise from HFP to cold conditions. Table 8-12 contains the CASMO-5 bias and tolerance limit data used to construct such experimental burnup reactivity decrement benchmarks.

9.2 Experimental Benchmark Specification

Eleven cases have been selected for experimental benchmarks, based on the Westinghouse RFA assembly. CASMO-5 calculations have been performed for each case in Table 9-1, covering a range of:

- enrichments
- burnable absorber loadings
- boron concentrations
- fuel and coolant temperatures
- decay times

Table 9-1
Benchmark Lattice Cases

1	3.25% Enrichment
2	5.00% Enrichment
3	4.25% Enrichment
4	Small Fuel Pin Depletion
5	20 WABA Depletion
6	104 IFBA Depletion
7	104 IFBA and 20 WABA Depletion
8	High Boron Depletion = 1500 ppm
9	Nominal Case Branch to SFP Hot Isothermal Temperatures = 150°F
10	Nominal Case Branched to SFP High Boron Concentration = 1500 ppm
11	High Power Depletion (power, coolant/fuel temp)

Case 3 with 4.25% enrichment and no burnable absorbers was chosen as the base case from which the lattice parameters were perturbed. For each case, the following calculations were performed:

- CASMO-5 was depleted to 60 GWd/T at the specified power density, temperatures, and boron concentrations.
- Cold cooling cases to 100 hours, 1 year, 5 years, and 15 years were performed for each branch case.
- Branch cases to cold were performed as restarts from the cooling cases at burnups of 10, 20, 30, 40, 50, and 60 GWd/T.

Since the anticipated application of these experimental benchmarks is for analysts to measure biases for their SFP or cask analysis tools (usually Monte Carlo), small simplifications of the standard CASMO-5 HFP depletion models were made to make subsequent analysis easier:

- Thermal expansion of materials is ignored (cold dimensions are used)
- Spacer grids are not modeled
- Water in guide tubes is modeled at the same temperature as the coolant
- Buckling search to critical is not used (since this is difficult for Monte Carlo methods)

None of these effects are important for the purposes of the experimental benchmark – it is only important that there be consistency between the CASMO-5 models and the models used with the SFP or cask tools.

The detailed descriptions of the eleven cases are contained in Appendix B.

9.3 Experimental Reactivity Decrement Tables

The k-infinity from each computed CASMO-5 cold case was used to construct reactivity decrement tables, to which the CASMO-5 experimental biases (from Table 8-12 were added to obtain cold experimental reactivity decrements and uncertainties – displayed in the tables of Appendix C.

The reactivity decrement uncertainties in the Appendix C tables make the assumption that decrement uncertainties are independent of the cooling time. This is a good approximation because the largest contributors to the change in reactivity decrement with cooling time are due to ^{135}Xe decay, ^{241}Pu decay (to ^{241}Am) and ^{155}Eu decay (to ^{155}Gd), and all these cross sections and decay constants have very small uncertainties.

9.4 End–Users Application of Experimental Reactivity Decrements

User's applications of experimental reactivity decrements for each case are anticipated to follow these steps:

1. Lattice depletions are performed with the user's lattice depletion tool to 60 GWd/T at the precise physical conditions specified in the Benchmarks.
2. Decay calculations for each cooling interval of interest (for example, 100-hour, 5-years, and 15-years) are performed with the user's lattice depletion tool from each depletion branch (10, 20, 30, 40, 50, 60 GWd/T) of Step 1.
3. Fuel number densities at each depletion/cooling branch from Step 2 are transferred to the user's criticality model (often Monte Carlo) of the lattice, and cold k-infinities are computed for each combination of lattice/burnup/cooling interval and lattice conditions.

   Note: SFP/cask criticality analysis may make modeling approximations that involve averaging of fuel pin number densities. In such cases, the averaging must also be performed at this Step of the Benchmark analysis.
4. Step 3 k-infinities are used to construct reactivity decrement tables as a function of lattice type, burnup, and cooling interval (analogous to those in Appendix C).
5. Step 4 reactivity decrement tables are differenced from the experimental reactivity decrement tables of Appendix C to construct biases for the user's methodology/tools as a function of lattice type, burnup, and cooling interval.
6. Reactivity decrement uncertainties are applied (Appendix C Table C-1) for each reactivity decrement of Step 5."
7. Biases from Step 5 and the uncertainties from Step 6 are combined with biases and uncertainties arising from other portions of the SFP/cask criticality analysis.

Section 10: Summary of Conclusions

10.1 Bias and Tolerance Limits in Percent of Depletion Reactivity Decrement

The CASMO-5 reactivity decrement biases and 95/95 tolerance limits from Section 8 were expressed in terms of pcm. The ultimate application of the depletion benchmarks uncertainties for SFP analysis are much more convenient if they are applied in terms of the **percentage of lattice depletion reactivity decrement**. As demonstrated by the data presented in Tables 8-7 and 8-8, the depletion reactivity is much lower for lattices in rack conditions than in the nominal reactor conditions. Consequently, it is appropriate to use reactivity decrements for the in-reactor conditions to convert the CASMO-5 measured bias and uncertainties into percentage terms. Table 10-1 displays the same data as Appendix C, Table C-2, converted to pcm for the seven nominal benchmark lattices of the Section 9 benchmarks with 100-hour cooling. The last row of Table 10-1 (the minimum absolute value of reactivity decrement from any of the seven lattices) is used to convert the bias and tolerance limit pcm values into percentage of absolute value of depletion reactivities as displayed in Table 10-2.

The Table 10-2 data support the conclusion that reactivity bias tolerance limits are less than 3.05% of the depletion reactivity for all fuel burnups.

Table 10-1
Measured Cold Reactivity Decrements (in pcm) for Nominal Benchmark Lattices

Lattice	Sub-batch Burnup (GWd/T)					
	10	20	30	40	50	60
1	-13244	-23339	-32084	-39600	-45698	-50324
2	-11414	-20159	-28034	-35490	-42538	-48974
3	-12184	-21519	-29874	-37620	-44608	-50594
4	-12024	-21709	-30724	39350	-47308	-54154
5	-20404	-23299	-29954	-37210	43878	-49624
6	-17314	22099	-29654	-37300	-44338	-50394
7	-25194	-24129	-29784	-36900	-43588	-49404
Minimum Abs. Value	11414	20159	28034	35490	42538	48974

Table 10-2
Measured CASMO-5 Cold Reactivity Decrement Biases and Tolerance Limits Expressed as Percentage of Absolute Value of Depletion Reactivity Decrement

Burnup (GWd/T)		10.0	20.0	30.0	40.0	50.0	60.0
CASMO-5 Bias	(pcm)	66	101	106	80	22	-64
Cold Tolerance Limit	(pcm)	348	537	654	752	831	888
CASMO-5 Bias	(% of depletion)	0.58	0.50	0.38	0.23	0.05	-0.13
Cold Tolerance Limit	(% of depletion)	3.05	2.66	2.33	2.12	1.95	1.81

10.2 General Conclusions

The flux map analysis methods developed and demonstrated in this report are capable of providing experimental determination of fuel reactivity burnup decrement biases and tolerance limits. The large amount of flux map data utilized in the 44 cycles of Duke Energy reactor analysis provided sufficient experimental sub-batch reactivity estimates (approximately 3000 points) such that resulting tolerance limits in measured HFP sub-batch reactivity decrement errors are less than 2.22% of the depletion reactivity decrement for burnups between 10.0 and 60.0 GWd/T.

TSUNAMI analysis demonstrated such a high degree of correlation between PWR fuel assemblies that nuclear data uncertainties are nearly independent of assembly design and enrichment. TSUNAMI analysis has demonstrated that extremely high correlation of reactivities between hot-to-cold conditions results in additional uncertainties for extending HFP reactivity decrement measurements to cold conditions of less than 350 pcm over the range of burnups from 0 to 60 GWd/T.

The combined HFP tolerance limits and the additional Hot-to-Cold uncertainties result in final tolerance limits for measured cold reactivity decrements that are less than 3.05% of the depletion reactivity for burnups between 10.0 and 60.0 GWd/T.

10.3 CASMO-5 Specific Conclusions

Reactivity decrement biases computed with CASMO-5 showed no enrichment dependence (within statistical uncertainties) over the range of 3.5 to 5.0% ^{235}U enrichment.

Results demonstrate that the historical 5% reactivity decrement uncertainty assumption, often applied in SFP criticality analyses, is conservative for cold SFP assembly reactivities with burnups between 10.0 and 60.0 GWd/T when computed with the CASMO-5 code.

Results provide a basis for supporting a smaller reactivity burnup decrement uncertainty for the historical 5% criterion, as displayed in the CASMO-5 biases and uncertainties of Table 10-2.

10.4 Related Conclusions

Reactivity decrement biases derived from flux map data have also been shown to be similar to those derived from the change in biases of reactor soluble boron concentrations from beginning of cycle (BOC) to end of cycle (EOC). This conclusion is based on the close agreement between changes in reactor boron biases and sub-batch reactivity decrement biases computed from flux map data with the CASMO-5 and SIMULATE-3 tools. These results add credibility to the more general assertion that changes in boron biases for other code systems should also be reliable indicators of fuel sub-batch reactivity decrement biases.

10.5 Experimental Benchmarks

The experimental biases derived for the CASMO-5 lattice physics code have been used to develop a series of experimental benchmarks that can be used to quantify reactivity decrement biases and uncertainties for other code systems used in lattice depletion and SFP/cask criticality analysis.

Specification of eleven experimental lattice benchmarks, covering a range of enrichments, burnable absorber loading, boron concentration, and lattice types have been documented in this report.

Interested parties can use these experimental benchmarks and their specific analysis tools to generate reactivity decrement biases and uncertainties that are unique to those tools.

Section 11: References

1. L. Kopp, NRC memorandum from L. Kopp to T. Collins, "Guidance on the Regulatory Requirements for Criticality Analysis of Fuel Storage at Light-Water Reactor Power Plants," dated August 19, 1998 (ADAMS Accession No. ML003728001).
2. J. Rhodes, et al., "CASMO-5 Development and Applications," PHYSOR-2006, Vancouver, BC, Canada. September 10-14, (2006).
3. J. Cronin, et al., "SIMULATE-3 Methodology Manual," STUDSVIK/SOA-95/18, Studsvik of America, Inc. (1995).
4. SCALE: A Comprehensive Modeling and Simulation Suite for Nuclear Safety Analysis and Design, ORNL/TM-2005/39, Version 6.1, June 2011. Available from Radiation Safety Information Computational Center at Oak Ridge National Laboratory as CCC-785.
5. *Benchmarks for Quantifying Fuel Reactivity Depletion Uncertainty*. EPRI, Palo Alto, CA: 2011. 1022909.
6. K. S. Smith, et al., "Depletion Reactivity Benchmarks – Part 1: Experimental Benchmarks for Quantifying PWR Fuel Reactivity Depletion Uncertainty," Nuclear Technology, Vol. 187, pp. 39-56 (January 2014).
7. D. Hagrman, et al., "INTERPIN-4 Model Improvements and Verification," SSP-07/445 Rev 0, Studsvik Scandpower, Inc. (2007).
8. D. Knott, et al., "CASMO-4 Methodology Manual," STUDSVIK/SOA-95/02, Studsvik of America, Inc. (1995).
9. T. Bahadir, et al., "CMSLINK User's Manual," STUDSVIK/SOA-97/04, Studsvik of America, Inc. (1997).
10. R. Lawrence, "Progress in Nodal Methods for the Solutions of the Neutron Diffusion and Transport Equations," Prog. Nucl. Energy, Vol. 17, No. 3, Pergamon Press, (1986).
11. K. Smith, et al., "QPANDA: An Advanced Nodal Method for LWR Analysis," Trans. Am. Nucl. Soc., Vol. 50, p 532, San Francisco, CA, (1985).
12. P. Esser and K. Smith, "A Semi-Analytic Two-group Nodal Model for SIMULATE-3," Trans. Am. Nucl. Soc., Vol. 68, p 220, San Diego, CA, (1993).

13. K. Smith, "Assembly Homogenization Techniques for Light Water Reactor Analysis," Prog. Nucl. Energy, Vol. 17, No. 3, Pergamon Press, (1986).
14. K. Smith and K. Rempe, "Mixed-Oxide and BWR Pin Power Reconstruction in SIMULATE-3," PHYSOR 90, Vol. 2, p. VIII-11, Marseille, France, (1990).
15. K. Rempe, et al., "SIMULATE-3 Pin Power Reconstruction: Methodology and Benchmarking," Proc. International Reactor Physics Conference, Vol. III, p. 19, Jackson, WY, (1988).
16. K. Smith, "MOX Analysis Methods in SIMULATE-3," Trans. Am. Nucl. Soc., Vol. 76, p 181, Orlando FL, (1997).
17. K. Smith and P. Esser, "Nodal Transport Model for SIMULATE," Proc. Spring Mtg., Kyoto, Japan, A49, Atomic Energy Society of Japan, (1993).
18. K. Smith, "Practical and Efficient Iterative Method for LWR Fuel Assembly Homogenization," Trans. Am. Nucl. Soc., Vol. 71, p 238, Washington, DC, (1994).
19. K. Smith, "Topical Report on Studsvik's Core Management System (CMS)," SSP-09/477-C, Rev 0, Studsvik Scandpower, Inc. (2010).
20. J. L. Eller, Letter, "Reference: Fuel, Core, and Operational Data to Support Core Physics Benchmark Analyses," DPC-1553.05.00.0222, Rev 0, March (2011).
21. Mathworks, "MATLAB 7 Data Analysis", Version 7.11.0 (R2010b), The Mathworks, Inc. (2010).
22. G.A. Gunow, "LWR Fuel Reactivity Depletion Verification Using 2D Full Core MOC and Flux Map Data," M.S. Thesis, MIT, https://dspace.mit.edu/handle/1721.1/97963, (2014).
23. E. Sykora, "Testing the EPRI Reactivity Depletion Decrement Uncertainty Methods," M.S. Thesis, MIT, https://dspace.mit.edu/handle/1721.1/103653, (2015).
24. *PWR Fuel Reactivity Depletion Uncertainty Quantification – Methods Validation Using BEAVRS Flux Map Data.* EPRI, Palo Alto, CA: 2015. 3002006432.
25. N. Horelik, B. Herman, B. Forget, and K. Smith. "Benchmark for Evaluation and Validation of Reactor Simulations (BEAVRS), v1.0.1," Proc. Int. Conf. Mathematics and Computational Methods Applied to Nuc. Sci. & Eng., Sun Valley, Idaho, (May 2013).
26. Benchmark for Evaluation and Validation of Reactor Simulations, Rev. 1.1.1, MIT Computational Reactor Physics Group (October 31, 2013). Available at the MIT website: http://crpg.mit.edu/research/beavrs
27. R. D. Harrison, et al., "Validation of WIMS/PANTHER PWR Fuel Reactivity Depletion Using the BEAVRS Benchmark Flux Map Data," PHYSOR 2016, Sun Valley, ID, May 1-5, (2016).

28. R. D. Harrison, et al., "PANTHER Benchmarking of Nuclear Reactor Burnup Data," Undergraduate Thesis, University of Cambridge, Cambridge, UK, (2015).

29. M. L. Williams, B. T. Rearden, "SCALE-6 Sensitivity/Uncertainty Methods and Covariance Data," Nuclear Data Sheets. 109. 2796-2800. 10.1016/j.nds.2008.11.012.

30. M. Williams, "Sensitivity and Uncertainty Analysis for Eigenvalue-Difference Response", *Nucl. Sci. Eng.* **155**, pp. 27 (2007).

31. R. MacFarlane, D. W. Muir, "NJOY99 -Code System for Producing Pointwise and Multigroup Neutron and Photon Cross Sections from ENDF/B Data," Los Alamos National Laboratory, RSICC PSR-480, (2000).

32. TVA Watts Bar FSAR, Amendment 98, Available from: *pbadupws.nrc.gov/docs/ML1013/ML101370696.pdf*

33. J. C. Wagner and C. V. Parks, *Parametric Study of the Effect of Burnable Poison Rods for PWR Burnup Credit*, NUREG/CR-6761 (ORNL/TM-2000/373), U.S. Nuclear Regulatory Commission, Oak Ridge National Laboratory, 2002.

34. R. Ellis, S*ystem Definition Document: Reactor Data Necessary for Modeling Plutonium Disposition in Catawba Nuclear Station Units 1 and 2*, ORNL/TM-1999/255, Oak Ridge National Laboratory, 2000.

35. C. Sanders and J. C. Wagner, *Study of the Effect of Integral Burnable Absorbers for PWR Burnup Credit*, NUREG/CR-6760 (ORNL/TM-2000-321), U.S. Nuclear Regulatory Commission, Oak Ridge National Laboratory, 2002.

36. B. D. Murphy, *Characteristics of Spent Fuel from Plutonium Disposition Reactors. Vol. 3: A Westinghouse Pressurized-Water Reactor Design*, ORNL/TM-13170/V3, Oak Ridge National Laboratory, 1997.

37. *Dissolution, Reactor, and Environmental Behavior of ZrO2-MgO Inert Fuel Matrix Neutronic Evaluation of MgO-ZrO2 Inert Fuels*, Department of Nuclear Engineering, Ben-Gurion University of the Negev, Beer-Sheva, Israel, February 2005. Available from: http://aaa.nevada.edu/paper/trp19_03.pdf)

Appendix A: Studsvik CMS Analysis Codes

The Studsvik Core Management System (CMS) is routinely used to perform the neutronic and thermal-hydraulic analysis needed for design, optimization, and safety analysis of nuclear reactor cores. While the CMS suite of codes is capable of performing steady-state and transient (dynamic) analysis of reactor cores, the methods described in this document are restricted to the CMS codes needed to perform steady-state and pseudo steady-state core analysis.

A.1 Code System Overview

The CMS code system consists of five separate codes, which are used as a package to perform reactor core analysis. The five codes are:

- **INTERPIN-4** [7] for analyzing the 1-D fuel temperatures for an individual fuel pin, as a function of:
  - Fuel pin design (e.g., enrichment, gas pressurization, etc.)
  - Linear heat loading
  - Fuel burnup
- **CASMO-4** [8] or **CASMO-5** [2] for analyzing the 2-D neutronic behavior of an individual fuel assembly, as a function of:
  - Lattice design (e.g., pin enrichment layout, burnable absorber design, etc.)
  - Local conditions (e.g., fuel temperature, coolant density, boron content, etc.)
  - Fuel burnup
  - Control rod insertion
- **CMSLINK** [9] for generating a library of tabularized CASMO-4 or CASMO-5 data for a collection of fuel assemblies and reflector types, as a function of:
  - Fuel burnup
  - Thermal hydraulic conditions
  - Control rod insertion
  - Fuel history effects
- **SIMULATE-3** [3] for analyzing the detailed 3-D reactor core neutronic and thermal-hydraulic behavior over the reactor core lifetime, as a function of:
  - Reactor power

- Coolant flow rate and inlet temperature
- Fuel burnup
- Control bank insertion

INTERPIN-4 and CMSLINK are often considered as auxiliary codes in the CMS suite, and they are described in this document only to the extent required to understand their interaction with CASMO-5 and SIMULATE-3. On the other hand, CASMO-5 and SIMULATE-3 are very large (many hundreds of thousands of lines of FORTRAN) codes that perform the bulk of the physics modeling in CMS.

This section details some of the more important physics models and methods that are important for understanding how CASMO-5 and SIMULATE-3 are used for this project.

A.2 INTERPIN-4

CASMO-5 and SIMULATE-3 need fuel temperature data as part of their respective physical models. CASMO-5 requires best-estimate average fuel pin temperature for each lattice type, and this temperature is typically assigned uniformly to all fuel pins in the lattice. Since the CASMO-5 case matrix includes lattice calculations (both branches and depletions) to off-nominal fuel temperatures, downstream SIMULATE-3 results are not very sensitive to the nominal CASMO-5 fuel temperatures. SIMULATE-3 results, however, are sensitive to the input fuel temperature tables – which provide the relationship between linear power density and the average fuel pin temperature. INTERPIN-4 is used to generate steady-state fuel temperature data that is provided to SIMULATE-3. INTERPIN-4 solves the 1-D radial heat conduction problem for an axial nodalized fuel pin, and temperatures are dependent on the physical models used to close the system of equations.

A.3 INTERPIN-4 Thermal Conductivities

The cladding thermal conductivity in INTERPIN-4 is from MATPRO:

$$k_{clad} = 7.51 + 2.09 \times 10^{-2} T - 1.45 \times 10^{-5} T^2 + 7.67 \times 10^{-9} T^3 \quad (W/m/K)$$

This oxide fuel conductivity model is taken from a recent NFI correlation that is plotted in Figure A-1 for UO_2 fuel at 4 different burnups. It can be seen that the conductivity degradation from fresh to 60 GWd/T burnup is between 40 and 60 percent, and this degradation has a very significant effect on fuel temperatures as a function of burnup.

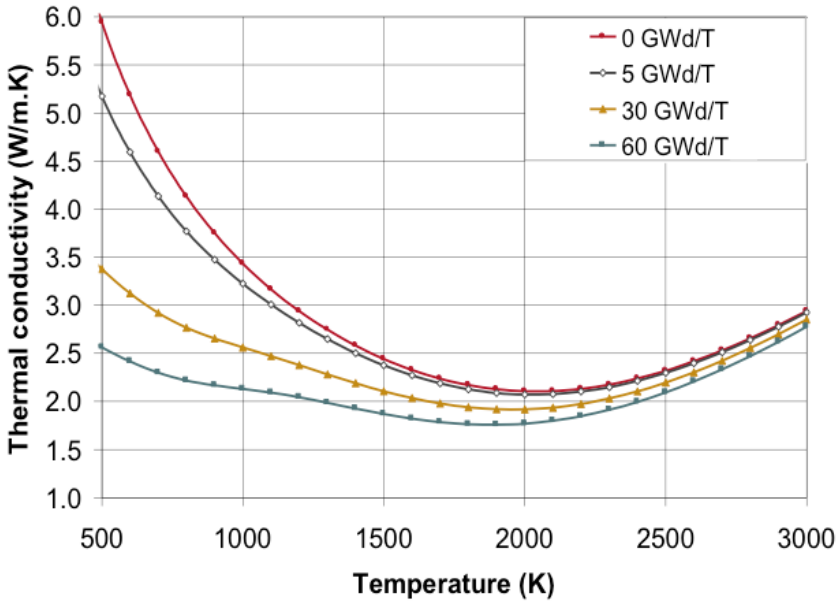

Figure A-1
UO_2 Conductivity as a Function of Burnup and Temperature

A.4 INTERPIN-4 Solid Pellet Swelling and Gap Conductance

As fuel pellets are irradiated, solid pellet swelling occurs because of the production of embedded gaseous fission products. This pellet swelling is modeled in INTERPIN-4 as a simple function of fuel burnup, E, in GWd/T

$$\left(\Delta V / V\right)_{fuel} = 0.7 \times 10^{-3} E$$

The fuel/clad gap conductance is modeled in INTERPIN-4 with two principal terms: a gaseous conductance term and a solid contact conductance term. The benchmark parameters of the Kjaerheim-Roldstad gaseous gap conductance sub-model (that accounts for the effect of fuel pellet surface and clad inner surface roughness) and the minimum residual gap of the Ross Stoute solid contact conductance model have both been calibrated to match measured centerline temperatures from pin irradiations in the Halden Reactor Project.

A.5 INTERPIN-4 Fuel Temperature Edits for SIMULATE-3

When INTERPIN-4 is used to generate SIMULATE-3 fuel temperature data, several calculations are automatically performed at different power levels, and results (similar to those of Figure A-2) are used to derive functional fits of the difference between average fuel temperature and the bulk coolant temperature. These data tables are then used directly in SIMULATE-3, and the lifetime-averaged fuel temperature is used as input to CASMO-5.

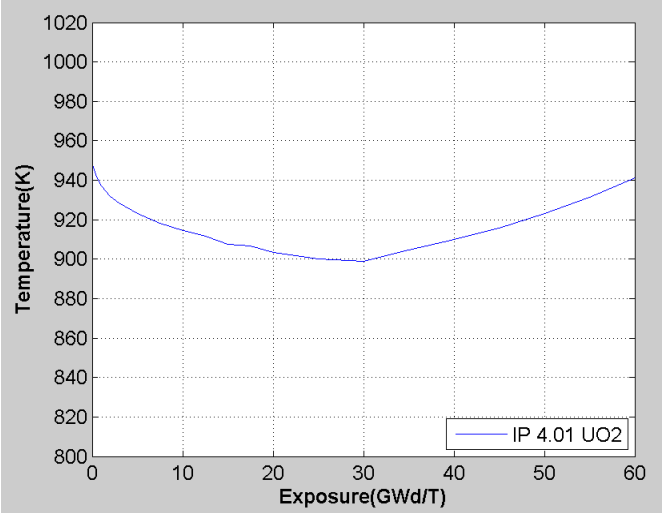

Figure A-2
Typical INTERPIN-4 Fuel Temperature Change with Burnup

A.6 CASMO-4 Lattice Physics Code

CASMO-4 is a two-dimensional transport theory lattice physics code used to analyze PWR and BWR fuel assemblies. CASMO-4 computes multi-group, multi-dimensional neutron flux distributions by solving the neutron transport eigenvalue problem. The resulting neutron flux solutions are used to compute coupled nuclide depletion, gamma production, and gamma transport within a fuel assembly. CASMO-4 can model fuel assemblies containing collections of cylindrical fuel rods, cylindrical burnable absorber rods, cluster control rods, and in-core instruments. CASMO-4's two-dimensional heterogeneous geometrical capabilities permit modeling of both single-assembly and Cartesian collections of assemblies. CASMO-4 is used to generate assembly neutronic data for the SIMULATE-3 nodal reactor analysis code. A flow diagram of a typical CASMO-4 calculation is displayed in Figure A-3.

A.7 CASMO-4 Cross Section Library

The CASMO-4 multi-group neutronic data library (N-Library) is the production neutronic data library used with CASMO-4, and it has been generated with the NJOY [31] data processing code that converts basic evaluated neutronic data (e.g., ENDF/B, JEF, etc.) from its continuous-energy form into multi-group neutronic data tables—as a function of material temperature and background cross sections. The CASMO-4 neutronic data library employs 70 neutron energy groups to cover the range from 0.0 to 10.0 MeV, consisting of 14 groups in the fast range (from 9.118 keV to 10.0 MeV), 13 groups in the resonance range (4.0 eV to 9.118 keV), and 43 groups in the thermal range (0.0 to 4.0 eV – with clustered groups around the 0.3 eV ^{235}Pu and 1.0 eV ^{240}Pu resonances).

The N-Library contains absorption, fission, nu-fission, transport, and scattering cross sections for 108 nuclides and materials, including; 18 important heavy metal isotopes (^{234}U to ^{246}Cm), 30 explicit and 2 lumped fission products (1 saturating and 1 non-saturating), 5 common LWR moderators, numerous LWR structural materials, and many common LWR burnable absorber isotopes. In addition to cross-section data, the library contains fission neutron emission spectra, fission product yields, and delayed neutron yields for all fissionable isotopes and decay constants for all radioactive isotopes. The starting point for the N-library was data produced in 1985 with NJOY from the ENDF/B-IV evaluated nuclear data files. When additional isotopes were added to the initial library or when deficiencies with ENDF/B-IV data were discovered, more recently-evaluated data was used to generate additional/replacement data.

As a result, the N-library contains data from JEF-1 for:

- Am-241 to Am-243
- Cm-242 to Cm-246
- Co-59, Ag-107, Ag-109, Cd-113, In-115
- Natural Hf, Hf-176 to Hf-180
- Pu-239 to Pu-242

from JEF-2.1 for:

- Er-162 to Er-171
- Tm-169 to Tm-171
- Gd-154 to Gd-158
- U-236

and from ENDF-B/VI, release 4 for:

- Mg, Zr, Nb, Mo, Sn
- Eu-154 and Eu-155

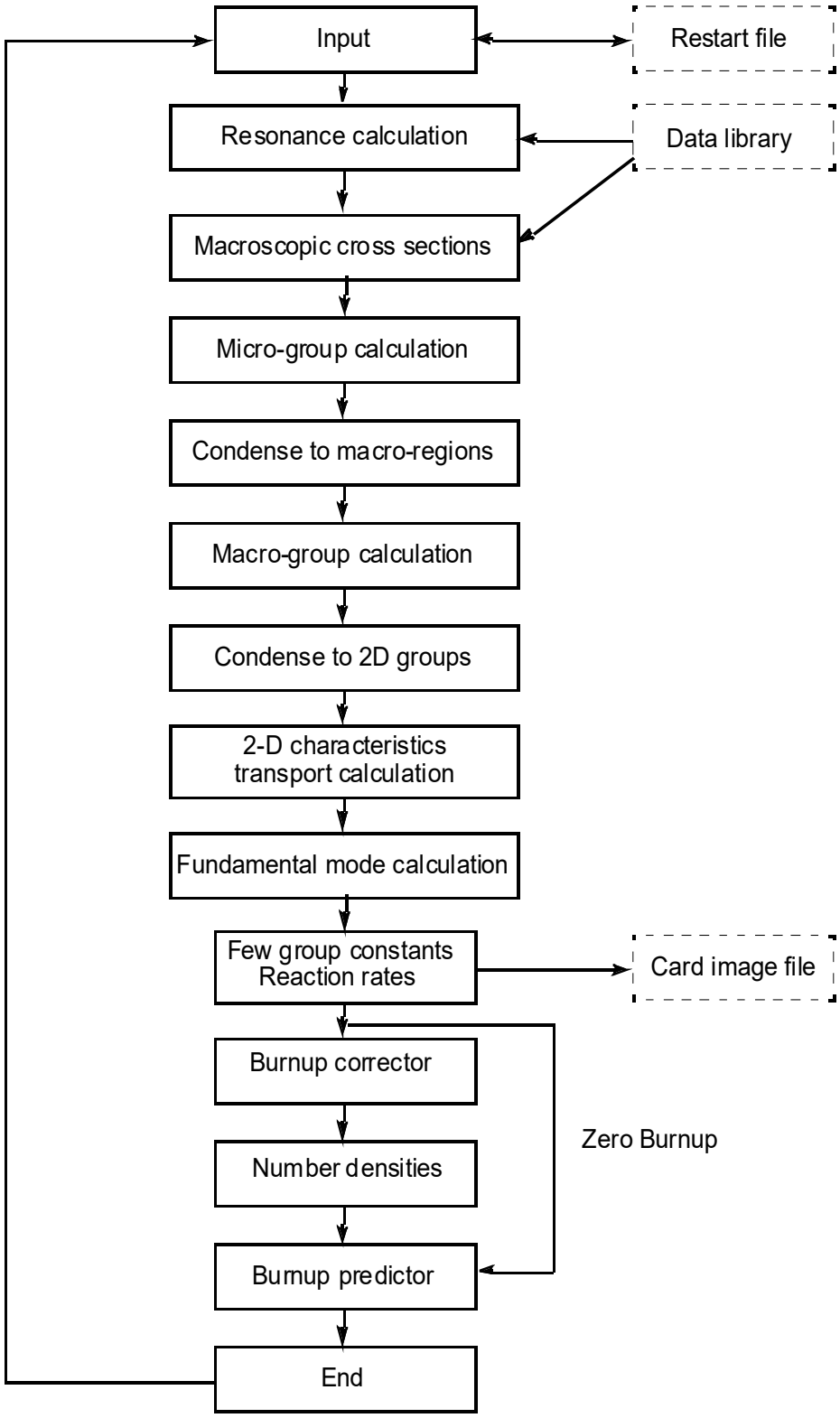

Figure A-3
Computational Flow Diagram of CASMO-4

A.8 CASMO-4 Isotopic Depletion Model

Once assembly flux distributions are known, reaction rates for each depletable nuclide are constructed so that the fuel depletion calculation can be performed. CASMO-4 makes the linearized chain approximation to decouple the depletion equations. The only approximation required in the linearized chain model is that "backward" transition rates (e.g., *n2n*, and alpha decay) in the middle of depletion chains be assumed constant over each time step.

When CASMO-4 detects the presence of gadolinia burnable absorbers in a lattice it automatically reduces burnup steps to 0.5 GWd/T until the gadolinia absorption is negligible, and then it reverts to large default depletion steps.

At each depletion step, CASMO-4 assumes that the power remains constant with depletion (rather than assuming that the flux remains constant). This is particularly important for accurate depletion, since the flux level and the average energy yield per fission change during a burnup step. The assumption necessitates a simple iterative calculation of the flux normalization so that the computed power at each depletion step remains constant.

A.9 CASMO-5 Lattice Physics Code

CASMO-5 is a significantly upgraded version from CASMO-4. The principal differences from CASMO-4 are:

- The "N" nuclear data library was replace with an ENDF/B-VII library
- The number of isotopes and materials in the library was increased from 108 to ~400
- The use of lumped fission products was eliminated
- The library group structure was changed from 70 to 586 energy groups
- Resonance models were upgraded to improve the two-term rational approximation
- The number of energy groups in the 2D transport (MOC) was increased from 8 to 19
- The ray spacing in the transport solver was reduced to 0.05 cm in all energy groups
- The polar angle quadrature was changed from Gauss-Legendre to the optimal T-Y quadrature
- The nuclide burnup model was changed from linearized chains to a partial matrix exponential

A.10 CASMO-5 Baffle/Reflector Models

PWR baffle and reflector data needed for SIMULATE-3 are generated directly with CASMO-5. CASMO-5 builds a 2-D transport model in which homogenous baffle and homogeneous reflector regions are appended to the side of the fuel assembly, as

depicted in Figure A-4. This 2-D transport problem is solved with reflecting boundary conditions on three sides and a vacuum boundary condition on the outer reflector surface. CASMO-5 provides direct edits of the baffle/reflector cross sections and homogenization data that are used by SIMULATE-3 for its nodal model of PWR cores. Similar models are also built for the top and bottom reflectors based on the users' specifications of the 1-D material representations above and below the fueled portion of the core.

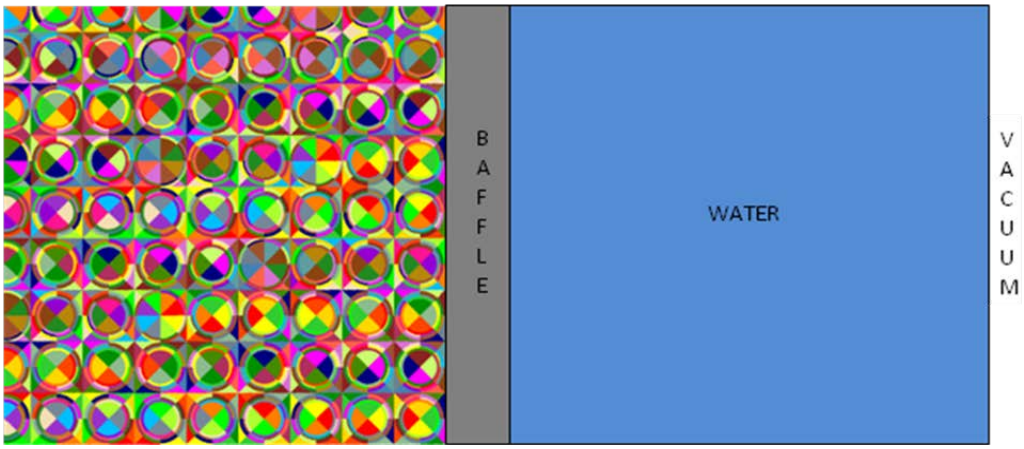

Figure A-4
CASMO-5 Baffle/Reflector Geometry

A.11 CMSLINK – CASMO-to-SIMULATE Linking Code

CMSLINK is a utility processing code used in CMS to gather and format all CASMO data needed in SIMULATE-3. CMSLINK reads the CASMO data files, evaluates the depletion and branch cases that are available, determines the most appropriate multi-dimensional table representation, and creates a binary data library that can be read by SIMULATE-3.

A.12 CMSLINK Multi-dimensional Data Tabulation

CMSLINK creates 1-D, 2-D and 3-D data tables for each of the assembly-averaged CASMO neutronic data, as a function of burnup (EXP), moderator temperature history (HTMO), boron history (HBOR), fuel temperature history (HTFU), moderator temperature (density, TMO), shut down cooling (SDC), boron concentration (BOR), control rod presence (CRD), and fuel temperature (TFU). For PWR lattices, the data tables and their secondary and tertiary dependencies consist are:

- Base 2-D table vs. (EXP, HTMO)
- Delta HBOR, 2-D table vs. (EXP, HBOR)
- Delta HTFU, 2-D table vs. (EXP, HTFU)
- Delta TMO, 2-D table vs. (EXP, TMO)
- Delta SDC, 2-D table vs. (EXP, SDC)

- Delta BOR, 3-D table vs. (EXP, BOR, TMO)
- Delta CRD, 3-D table vs. (EXP, CRD, TMO)
- Delta TFU, 3-D table vs. (EXP, TFU, TMO)

Since pin power reconstruction and detector fission rate data are very large (e.g., pin power form functions), a simplified data representation is used for this data. For PWR lattices, the data tables consist of:

- Base 1-D table vs. (EXP)
- Delta TMO, 1-D table vs. (EXP)
- Delta CRD, 2-D table vs. (EXP, CRD)
- Delta HBOR, 1-D table vs. (EXP)
- Delta SDC, 1-D table vs. (EXP)
- Delta BOR, 1-D table vs. (EXP)
- Delta TFU, 1-D table vs. (EXP)

CMSLINK creates a binary library containing data, for each CASMO lattice type, including the complete description of independent variables, table structure, and table values for every data table. In addition, QA file trail data (code version numbers, neutron library version numbers, executable creation dates, executing computers and run dates) are added to the library to provide a traceable data trail into SIMULATE-3.

A.13 SIMULATE-3 Nodal Code Overview

SIMULATE-3 is the three-dimensional advanced nodal diffusion code used in the CMS system for analyzing the pseudo steady-state behavior of PWR and BWR cores. SIMULATE-3 is a coupled nodal neutronics/thermal-hydraulic code capable of performing fuel depletion needed to model the reactor core throughout its lifetime. The flow of a typical SIMULATE-3 computational sequence is depicted in the Figure A-5. It can be seen from this figure that for each depletion step, SIMULATE-3 performs a nested iteration to synchronize thermal-hydraulic conditions, nuclear data, neutronics power distributions, and fuel assembly depletion. When all nonlinear fields are converged, SIMULATE-3 then performs pin power reconstruction to recover individual pin power distributions and detector fission rates. The details of each of the major modules in SIMULATE-3 are described in the following sections of this report.

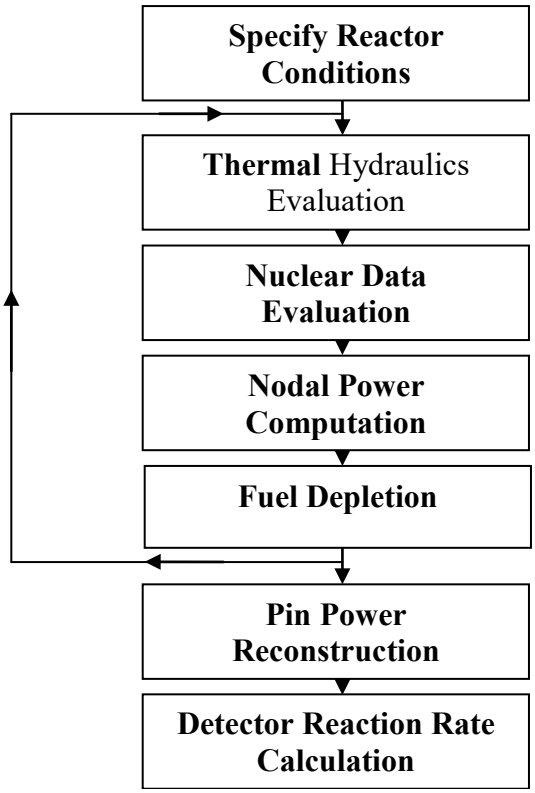

Figure A-5
SIMULATE-3 Flowchart

A.14 SIMULATE-3 PWR Thermal Hydraulics Model

The SIMULATE-3 PWR thermal hydraulics uses one characteristic hydraulic channel per fuel assembly (or four when using 4 node per assembly neutronics model) with the assumption of no radial cross-flow between assemblies. The axial nodalization of the thermal hydraulics is identical to that used in the neutronics, with 24 or more nodes in typical applications. Since SIMULATE-3 is a steady-state (not dynamic) code, these assumptions result in a thermal-hydraulic model that is basically a heat balance – with the following additional assumptions:

- Assembly inlet flows are uniform (or distributed with a user-specified distribution).
- Assembly inlet temperatures are uniform (or distributed with a user-specified distribution).
- All fluid properties are evaluated at the primary system pressure (default is 2250 psi).
- Direct energy deposition in coolant (neutron slowing down, gamma deposition, etc.) is a fixed fraction of the total power generated in a node (default is 2.5%).

Given these assumptions, the coolant enthalpy is computed by marching up each channel and adding the energy produced in each node to the enthalpy, and the coolant

density is evaluated from the enthalpy using water properties from the ASME steam tables.

In SIMULATE-3, the node-averaged fuel temperature for node n is computed from the node-averaged coolant temperature, a tabulated function of linear power density of each node, P_n, and a constant quadratic term having the form:

$$TFU_n = TMO_n + TFU_m(EXP, P)P_n + TFU_m^q P_n^2$$

The linear tables are constructed for each fuel type, m, and are constructed as a function of nodal fuel burnup and power density, while the quadratic term is constant for each fuel type. The linear term is a user-input table for SIMULATE-3, and within the CMS suite of codes, INTERPIN-4 is used to generate the fuel temperature data tables.

The neutronic feedback in SIMULATE-3 is based on node-averaged conditions (the rod-by-rod variation in temperatures is ignored), and consequently node-averaged coolant density and fuel temperature are the only thermal-hydraulic parameters needed for steady-state SIMULATE-3 PWR calculations.

A.15 SIMULATE-3 Nuclear Data Interpolation

Once thermal-hydraulic conditions are known (at each neutronic/hydraulic iteration), nuclear data is evaluated for each node of the core model. Values for all instantaneous library parameters (BOR, DEN, TFU, SDC, and CRD) and each historical parameter (EXP, HTMO, HBOR, and HTFU) are constructed for each node. Linear interpolations in the 2-D and 3-D CMSLINK data tables are then performed to evaluate the required node-by-node parameters.

These data provide the non-linear link between the thermal hydraulics, fuel depletion, and neutronics models of SIMULATE, and multiple iterations are required to obtain a converged solution of core conditions.

A.16 SIMULATE-3 Two-group Nodal Diffusion Model

Once the thermal-hydraulic conditions and cross sections are known for each node of the core model, a three-dimensional diffusion model for the core can be constructed, using standard notation, as

$$-\nabla \cdot D_g(r)\nabla\Phi_g(r) + \Sigma_{t,g}(r)\Phi_g(r) = \sum_{g'=1}^{2}\left[\frac{\chi_g}{k_{eff}}\nu\Sigma_{f,g'}(r) + \Sigma_{gg'}(r)\right]\Phi_{g'}(r) \quad .$$

Integrating this equation over the volume of each node in the core model, one obtains the nodal neutron balance equation

$$\sum_{s=1}^{6}\left[\frac{J_g^{m,s}}{h_s}\right]+\bar{\Sigma}_{t,g}^{m}\bar{\Phi}_g^{m}=\sum_{g'=1}^{2}\left[\frac{\chi_g}{k_{eff}}\overline{\nu\Sigma}_{f,g'}^{m}+\bar{\Sigma}_{gg'}^{m}\right]\bar{\Phi}_{g'}^{m},$$

where

$J_g^{m,s} \equiv$ average net neutron current on surface, *s*, of node *m*

$\bar{\Phi}_g^{m} \equiv \frac{1}{V^m}\int \Phi_g(r)dV$ is the average scalar neutron flux in node *m*

and

$V^m \equiv$ volume of node *m*.

The nodal balance equation simply expresses the fact that the net neutron production in node m equals the rate at which neutrons leak out of the six surfaces of node m. The nodal balance equation cannot be solved without additional relationships that relate the surface-averaged net currents to the node-averaged scalar fluxes. SIMULATE-3 uses the well known transverse-integration method to derive these required coupling relationships. For instance, by integrating the nodal diffusion equation over the y and z directions, one obtains a 1-D coupling expression as a function of x

$$-\tilde{D}_g^{m}(x)\frac{d^2}{dx^2}\tilde{\Phi}_g^{m}(x)+\tilde{\Sigma}_{t,g}^{m}(x)\tilde{\Phi}_g^{m}(x)=\sum_{g'=1}^{2}\left[\frac{\chi_g}{k_{eff}}\nu\tilde{\Sigma}_{f,g'}^{m}(x)+\tilde{\Sigma}_{gg'}^{m}(x)\right]\tilde{\Phi}_{g'}^{m}(x)+L_g^{m,x}(x)$$

where the transverse leakage for direction x in node m has been defined as

$$-L_g^{m,x}(x)\equiv\frac{1}{h_y h_z}\iint \tilde{D}_g^{m}(x)\left[\frac{d^2}{dy^2}+\frac{d^2}{dz^2}\right]\Phi_g(r)\,dy\,dz$$

This transverse leakage expression is a rigorous expression for the x-dependence of the flux in node m. If one makes the assumption that the diffusion coefficient is independent of position within node m, an expression that relates the shape of the x-directed net current in node m to the transverse-integrated scalar flux can be written as

$$J_g^{m,x}(x)=-\tilde{D}_g^{m}\frac{d}{dx}\tilde{\Phi}_g^{m}(x)$$

The principal assumption in the transverse-integrated nodal methods is that the *x*-shape of the transverse leakage in node *m* can be represented accurately by a quadratic fit (preserving the node-averaged net leakages) to the average transverse leakage in three neighboring nodes *m*-1, *m*, and *m*+1. This approach permits one to construct 1-D coupling equations for each of the *x*, *y*, and *z* directions, and the transverse leakage terms depend only on the face-averaged net currents – which become known as the nodal balance equations are iteratively solved.

In order to fully close this system of equations, one must specify how the transverse-integrated fluxes are to be represented. SIMULATE-3 has two different approximations for the transverse-integrated flux shapes for direction u within each node:

$$\tilde{\Phi}_g^m(u) = \bar{\Phi}_g^m + \phi_g^{1,m}u + \phi_g^{2,m}(3u^2 - \frac{1}{4}) + \phi_g^{3,m}(u^3 - \frac{u}{4}) + \phi_g^{4,m}(u^4 - \frac{3u^2}{10} + \frac{1}{80})$$

or

$$\tilde{\Phi}_g^m(u) = \bar{\Phi}_g^m + \phi_g^{1,m}u + \phi_g^{2,m}(3u^2 - \frac{1}{4}) + \phi_g^{3,m}(u^3 - \frac{u}{4}) + \phi_g^{4,m}(u^4 - \frac{3u^2}{10} + \frac{1}{80}) + \phi_g^{c,m}\left[\cosh(\kappa_g u) - \frac{2}{\kappa_g}\sinh(\kappa_g u)\right] + \phi_g^{s,m}\left[\sinh(\kappa_g u)\right]$$

where

$$\kappa_g = \sqrt{\tilde{\Sigma}_g^m / \tilde{D}_g^m} \quad .$$

For analysis of UO_2 cores, SIMULATE-3 uses the polynomial expansion to represent the scalar flux shapes for both the fast and thermal groups. When cores containing MOX fuel assemblies are detected in SIMULATE-3, the thermal flux expansions are automatically changed to use the transcendental functions so that more accurate flux shapes are obtained at the interfaces between UO_2 and MOX assemblies.

A.17 SIMULATE-3 Macroscopic Depletion Model

SIMULATE-3 performs fuel depletion throughout the life of the reactor core. Explicit nuclide concentrations for ^{135}I, ^{135}Xe, ^{149}Pm and ^{149}Sm are tracked directly in SIMULATE-3 by solving the nuclide depletion chains and using CASMO-5 generated data for: 1) fission yields, 2) capture cross sections, and 3) decay constants. All other isotopes are treated indirectly in SIMULATE-3 with a macroscopic depletion model. In SIMULATE-3's macroscopic depletion model, CASMO-5 data has been tabulated as a function of fuel burnup (EXP). Consequently, SIMULATE-3 needs only compute the fuel burnup – all other isotopic depletion effects are treated indirectly by interpolating in the CMSLINK data tables to the appropriate burnup point.

Actual fuel isotopic concentrations depend on the local conditions that the fuel assembly experiences during its lifetime. In order to approximate these "history effects", SIMULATE-3 treats water density, fuel temperature, and boron concentration as history variables. For instance, nodes at the top of the core have been depleted with less coolant density that those nodes at the bottom of the core. The resulting harder spectrum leads to production of more plutonium (per GWd/T) at the top of the core.

SIMULATE-3 models this dependence on water density history by interpolating in the CMSLINK data tables with the historical density of coolant and interpolates in the CMSLINK history data tables. Each node in the core experiences a time-varying fuel temperature, coolant density, and boron, and consequently, historical variables must be integrated in time to yield appropriate history values. In SIMULATE-3 a weighted history model is used to accumulate the history variables. As an example, when the burnup, in node *m*, advances from E^m to $E^m + \Delta E^m$ the boron history in node *m* is accumulated as

$$HBOR^m(E^m + \Delta E^m) \equiv \frac{HBOR^m(E^m) + w \cdot BOR^m(E^m)\Delta E^m}{E^m + w \cdot \Delta E^m}$$

This weighted history formulation is motivated by the fact that when conditions change significantly, the most recent history tends to "burn in" more quickly than would be modeled by unity history weighting. The weighting parameter, w, is computed for each fuel type and history variable from the build-up rates in the CMSLINK library data. Typically the history weighting parameter is in the range of 2.0 to 2.5. This history treatment allows SIMULATE-3 to model depletion effect more accurately than if only fuel burnup was used.

SIMULATE-3 also treats the burnup shape within each core node. Homogenized cross-section terms are represented as functions of position in the radial direction. If the spatial shape of the cross section is known, it directly impacts the algebraic relationship for the nodal coupling parameters. The intra-nodal spatial shape of burnup in SIMULATE-3 is modeled by tracking the node surface-averaged burnups as well as the node-averaged burnup. A quadratic polynomial shape for the burnup is constructed for each direction using the two surface-averaged burnups for that direction and the node-averaged burnup. The quadratic burnup shape is then transformed into a quadratic cross-section shape and these shapes are used when solving for nodal coupling parameters. Treatment of the spatial variation of burnup within each node improves the accuracy of computed reactor core flux and power distributions.

A.18 SIMULATE-3 Detector Fission Rate Computation

The SIMULATE-3 nodal method provides transverse-integrated flux shapes in each of the three directions. The nodal flux at each radial corner points of the assembly are evaluated by constructing a 2-D distribution from the x- and y-directed transverse-integrated fluxes and evaluating these distributions at each of the 4 corners as:

$$\tilde{\Phi}_g^{cp} = \left. \frac{\tilde{\Phi}_g^m(x) \cdot \tilde{\Phi}_g^m(y)}{\bar{\Phi}_g^m} \right|_{cp}.$$

Since each of the four nodes that meet at a corner can be used to approximate the corner point flux, one can combine the four homogeneous flux estimates, together with the four CASMO-5 corner point form functions (analogous to the surface discontinuity factors) to obtain a single estimate for the corner point flux:

$$\Phi_g^{cp} = \frac{\tilde{\Phi}_{g,i,j}^{cp}\left[\frac{\Phi_g^{cp,CASMO}}{\bar{\Phi}_g^{CASMO}}\right]_1 + \tilde{\Phi}_{g,i+1,j}^{cp}\left[\frac{\Phi_g^{cp,CASMO}}{\bar{\Phi}_g^{CASMO}}\right]_2 + \tilde{\Phi}_{g,i,j+1}^{cp}\left[\frac{\Phi_g^{cp,CASMO}}{\bar{\Phi}_g^{CASMO}}\right]_3 + \tilde{\Phi}_{g,i+1,j+1}^{cp}\left[\frac{\Phi_g^{cp,CASMO}}{\bar{\Phi}_g^{CASMO}}\right]_4}{4}.$$

Detector reaction rates for movable in-core detectors are computed directly in SIMULATE-3 from the two-group fluxes at the detector location (the heterogeneous corner point fluxes). The reaction rates for isotope *i* and interaction type α are computed using detector cross sections from the CMSLINK library and reconstructed fluxes as:

$$RR_\alpha^i = \Phi_1^{CP}\sigma_{\alpha 1}^i + \Phi_2^{CP}\sigma_{\alpha 2}^i.$$

Appendix B: Reactivity Benchmark Specifications

Eleven experimental benchmarks, based on simplifications of publically available data for the Westinghouse RFA and OFA assemblies, are described here. They cover a range of

- enrichments,
- burnable absorber ladings,
- boron concentrations,
- fuel and coolant temperatures, and
- decay times.

For each case in Table B-1, a complete geometrical and material description follows, and the experimental reactivity decrement tables are presented in Appendix C.

The sources for non-proprietary are listed below:

- RFA-like lattice and pin dimensions, taken from Reference [32].
- OFA-like lattice/pin dimensions, taken from Reference [33].
- WABA pin dimensions, taken from Reference [33].
- IFBA and WABA burnable absorber loading patterns, taken from Reference [34].
- IFBA ^{10}B boron loading, taken from Reference [35].
- WABA boron loading, taken from Reference [36].
- IFBA modeling thickness and inert materials density, taken from Reference [37].

Note that all lattices are depleted with a power density of 104.5 W/cc (38.1 W/gm heavy metal) – except for case 11 that is depleted at 156.75 W/cc (150% of nominal power density). **All temperatures are in K and nuclide number densities are expressed in atoms/cc**. For lattices that do not explicitly include the "Structural Material Description and the "Coolant Description," the nominal lattice values are applicable.

Table B-1
Benchmark Lattice Cases

1	3.25% Enrichment
2	5.00% Enrichment
3	4.25% Enrichment
4	Small Fuel Pin Depletion
5	20 WABA Depletion
6	104 IFBA Depletion
7	104 IFBA and 20 WABA Depletion
8	High Boron Depletion = 1500 ppm
9	Nominal Case Branch to SFP Hot Isothermal Temperatures = 150°F
10	Nominal Case Branched to SFP High Boron Concentration = 1500 ppm
11	High Power Depletion (power, coolant/fuel temp)

B.1 Nominal Fuel Assembly

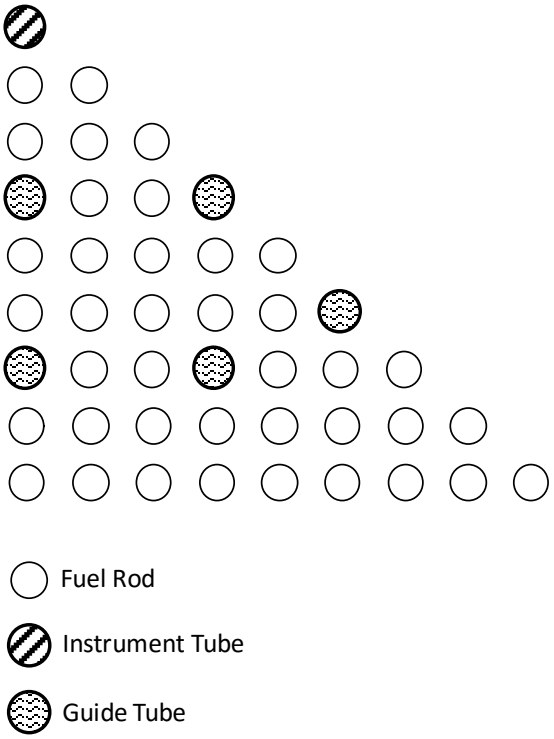

Physical Description

Number of pins along side	17
Pin pitch	1.2598 cm
Inter-assembly spacing	21.5036 cm
Fuel pellet OR	0.4096 cm
Clad IR	0.4180 cm
Clad OR	0.4750 cm
Guide/instrument tube IR	0.5610 cm
Guide/instrument tube OR	0.6120 cm

Structural Material Description

Material (Zr-4)Density	6.55 (g/cm3)
Temp., unheated	580K
Temp., heated	$0.12*T_{fuel}+0.88*T_{coolant}$
Nuclide	**Number Density**
Zr-4	4.32444E+22

Coolant Description, Depletion (Nominal)

Boron Concentration	900 ppm
Temperature	580 K
Nuclide	**Number Density**
H	4.75756E+22
O	2.37894E+22
B	3.56773E+19

Coolant Description, Cold

Boron Concentration	0 ppm
Temperature	293 K
Nuclide	**Number Density**
H	6.67431E+22
O	3.33738E+22

B.2 CASE 1: 3.25% Enriched - No Burnable Absorbers

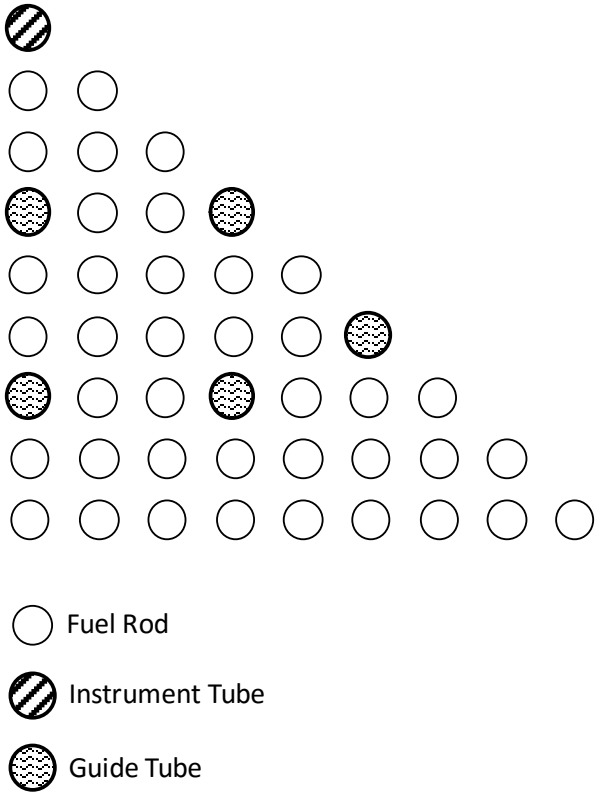

Fuel Rod

Instrument Tube

Guide Tube

Fuel Material Description

Material Density	10.340 (g/cm3)
Fuel Temperature	900 K
Nuclide	**Number Density**
U-235	7.59010E+20
U-234	6.09917E+18
U-238	2.23037E+22
O	4.61377E+22

B.3 CASE 2: 5.00% Enriched - No Burnable Absorbers

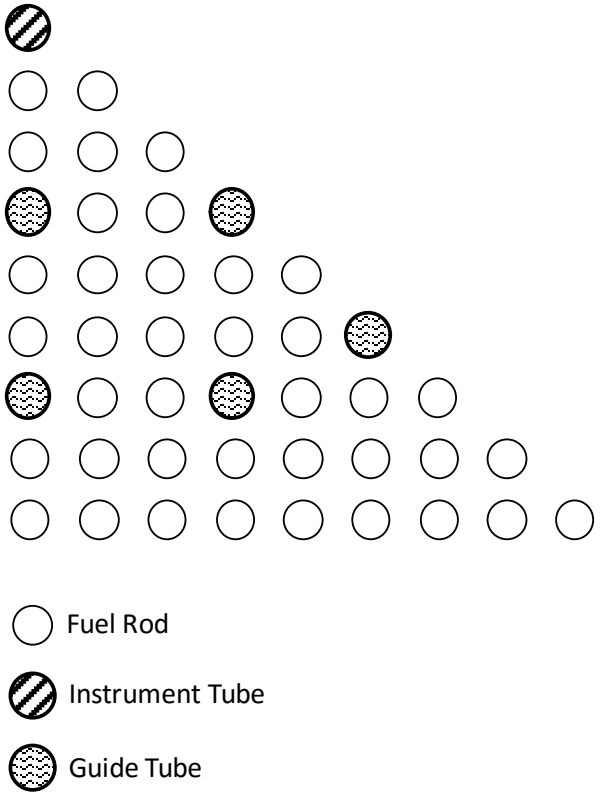

Fuel Rod

Instrument Tube

Guide Tube

Fuel Material Description

Material Density	10.340 (g/cm3)
Fuel Temperature	900 K
Nuclide	**Number Density**
U-235	1.16768E+21
U-234	9.38308E+18
U-238	2.18964E+22
O	4.61469E+22

B.4 CASE 3: 4.25% Enriched - No Burnable Absorbers

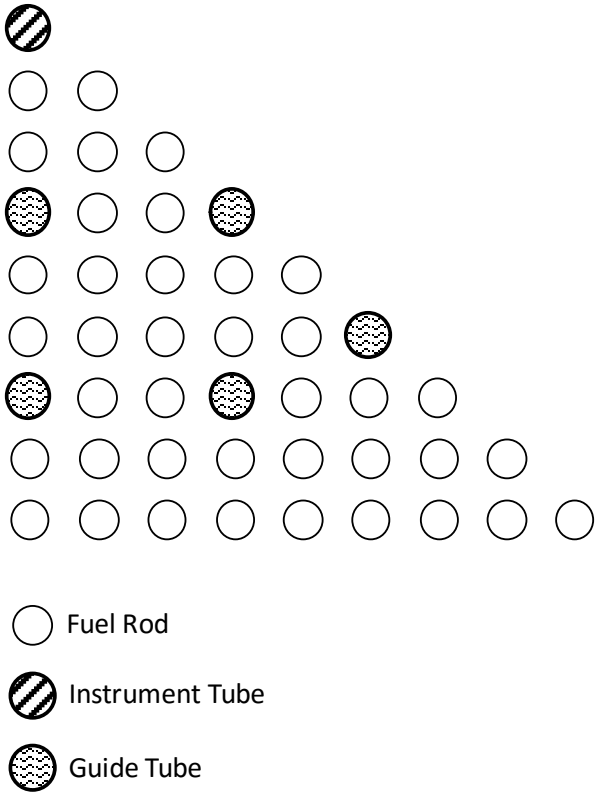

Fuel Rod

Instrument Tube

Guide Tube

Fuel Material Description

Material Density	10.340 (g/cm3)
Fuel Temperature	900 K
Nuclide	**Number Density**
U-235	9.92536E+20
U-234	7.97571E+18
U-238	2.20709E+22
O	4.61429E+22

B.5 CASE 4: Small Fuel Pin

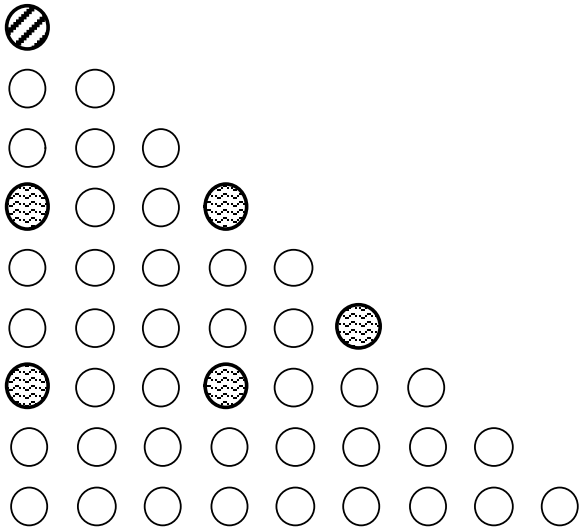

Fuel Rod

Instrument Tube

Guide Tube

Physical Description

Number of pins along side	17
Pin pitch	1.2598 cm
Inter-assembly spacing	21.5036 cm
Fuel pellet OR	0.3922 cm
Clad IR	0.4000 cm
Clad OR	0.4572 cm
Guide/instrument tube IR	0.5610 cm
Guide/instrument tube OR	0.6120 cm

Structural Material Description

Material (Zr-4)Density	6.55 (g/cm3)
Temp., unheated	580K
Temp., heated	$0.12*T_{fuel}+0.88*T_{coolant}$
Nuclide	**Number Density**
Zr-4	4.32444E+22

Fuel Material Description

Material Density	10.340 (g/cm3)
Fuel Temperature	900 K
Nuclide	**Number Density**
U-235	9.92536E+20
U-234	7.97571E+18
U-238	2.20709E+22
O	4.61429E+22

B.6 CASE 5: 20 Lumped Burnable Poison (WABA) Pins

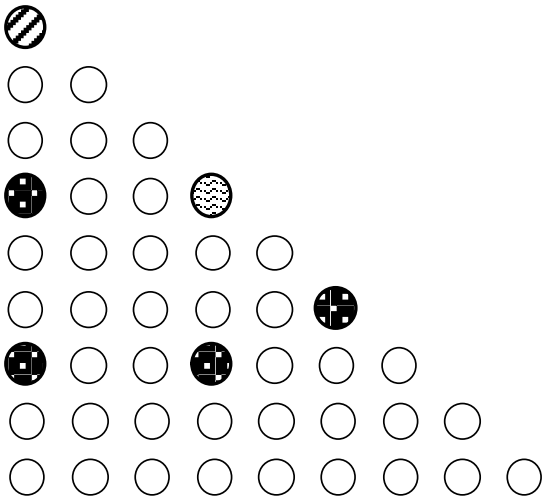

Fuel Rod

Instrument Tube

Guide Tube

LBP

Fuel Material Description

Material Density	10.340 (g/cm3)
Fuel Temperature	900 K
Nuclide	**Number Density**
U-235	9.92536E+20
U-234	7.97571E+18
U-238	2.20709E+22
O	4.61429E+22

Lumped Burnable Poison (WABA)

Annular clad IR	0.2860 cm
Annular clad OR	0.3390 cm
Active region IR	0.3530 cm
Active region OR	0.4040 cm
Inner clad IR	0.4180 cm
Inner clad OR	0.4840 cm
Outer clad IR	0.5610 cm
Outer clad OR	0.6120 cm

Active Region

Material Density	3.65 (g/cm3)
Boron Loading	6.03 mg/cm B-10
Nuclide	**Number Density**
C	1.40923E+21
O	6.23784E+22
Al	4.15904E+22
B-10	2.99030E+21

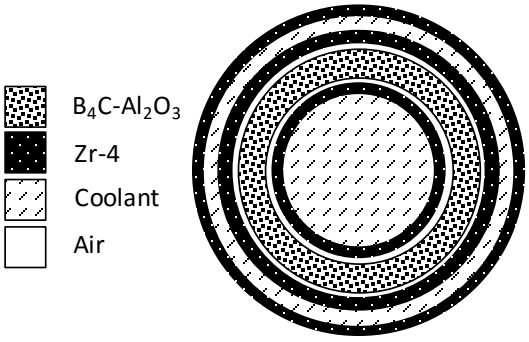

B.7 CASE 6: 104 Integral Fuel Burnable Absorbers (IFBA) Pins

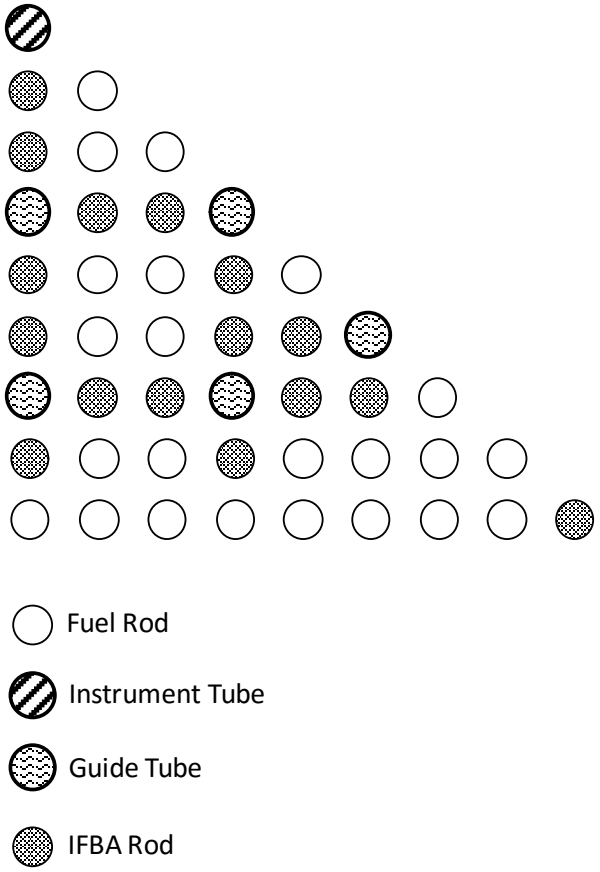

Fuel Material Description	
Material Density	10.340 (g/cm3)
Fuel Temperature	900 K
IFBA Description	
Material Density	6.100 (g/cm3)
Coating Density	0.925 mg/cm B-10
Coating Thickness	0.01 mm
Nuclide	**Number Density**
U-235	9.92536E+20
U-234	7.97571E+18
U-238	2.20709E+22
O	4.61429E+22
Zr-4	3.22187E+22
B-10	2.15913E+22

B.8 CASE 7: 104 IFBA and 20 WABA Pins

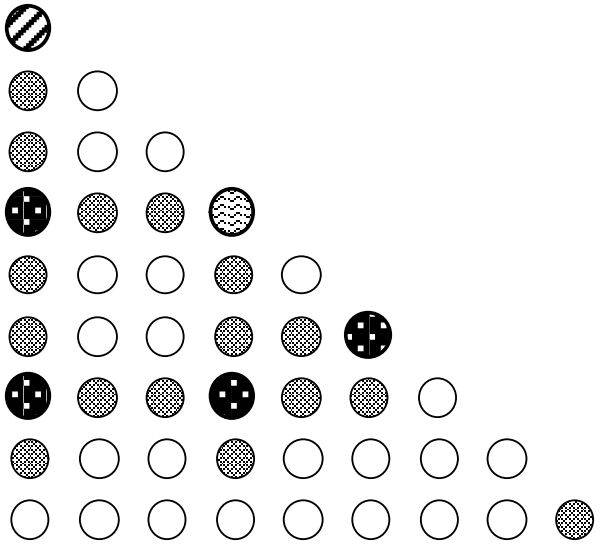

Fuel Rod

Instrument Tube

Guide Tube

IFBA Rod

LBP

Fuel Material Description

Material Density	10.340 (g/cm3)
Fuel Temperature	900 K

IFBA Description

Material Density	6.100 (g/cm3)
Coating Density	0.925 mg/cm B-10
Coating Thickness	0.01 mm

Nuclide	**Number Density**
U-235	9.92536E+20
U-234	7.97571E+18
U-238	2.20709E+22
O	4.61429E+22
Zr-4	3.22187E+22
B-10	2.15913E+22

Lumped Burnable Poison (WABA)

Material Density	3.65 (g/cm3)
Boron Loading	6.03 mg/cm B-10

Nuclide	**Number Density**
C	1.40923E+21
O	6.23784E+22
Al	4.15904E+22
B-10	2.99030E+21

B.9 CASE 8: High Boron Depletion

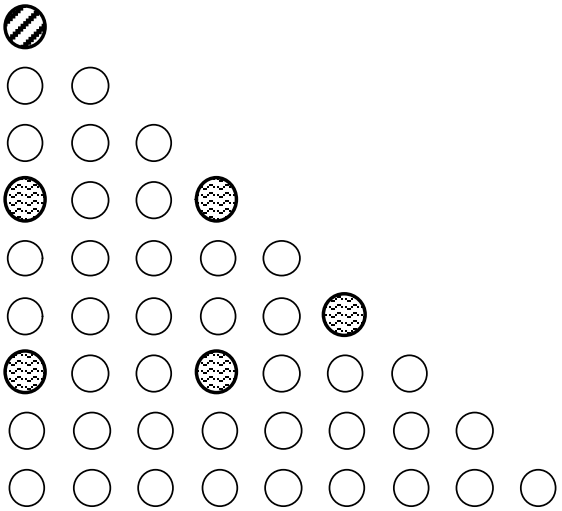

Fuel Rod

Instrument Tube

Guide Tube

Fuel Material Description

Material Density	10.340 (g/cm3)
Fuel Temperature	900 K
Nuclide	**Number Density**
U-235	9.92536E+20
U-234	7.97571E+18
U-238	2.20709E+22
O	4.61429E+22

Coolant Description, Depletion

Boron Concentration	1500 ppm
Temperature	580 K
Nuclide	**Number Density**
H	4.75756E+22
O	2.37894E+22
B	5.94621E+19

B.10 CASE 9: Nominal Case Branched to SFP Hot Isothermal Temperatures = 150F

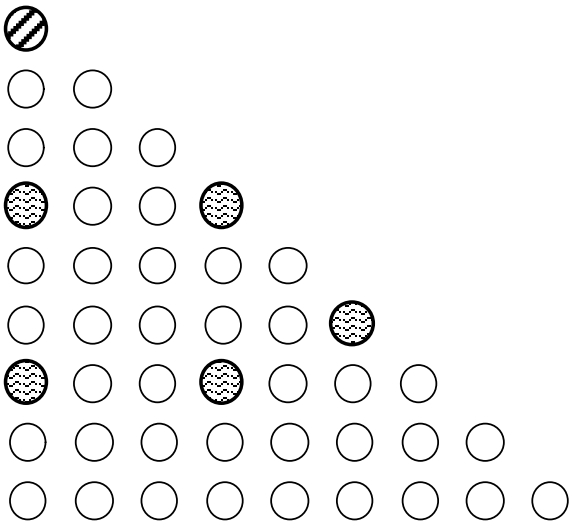

Fuel Rod

Instrument Tube

Guide Tube

Fuel Material Description

Material Density	10.340 (g/cm3)
Fuel Temperature	900 K
Nuclide	**Number Density**
U-235	9.92536E+20
U-234	7.97571E+18
U-238	2.20709E+22
O	4.61429E+22

Coolant Description, Cold

Boron Concentration	0 ppm
Temperature	338.7 K
Nuclide	**Number Density**
H	6.55262E+22
O	3.27653E+22

B.11 CASE 10: Nominal Case Branched to SFP High Rack Boron Concentration = 1500 ppm

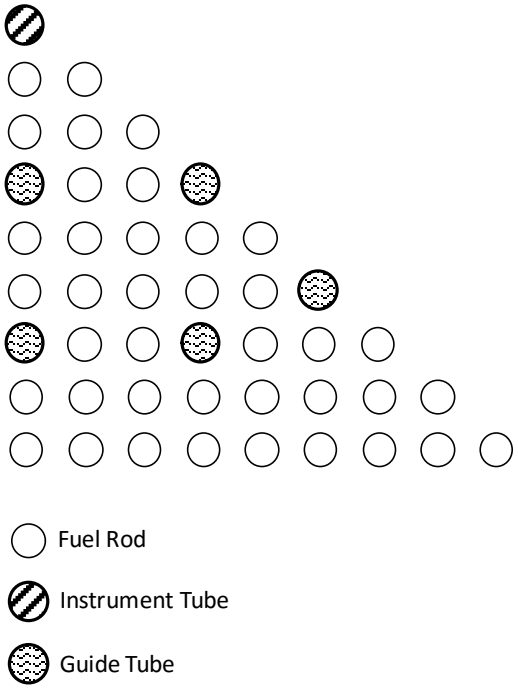

Fuel Rod

Instrument Tube

Guide Tube

Fuel Material Description

Material Density	10.340 (g/cm3)
Fuel Temperature	900 K
Nuclide	**Number Density**
U-235	9.92536E+20
U-234	7.97571E+18
U-238	2.20709E+22
O	4.61429E+22

Coolant Description, Cold

Boron Concentration	1500 ppm
Temperature	293 K
Nuclide	**Number Density**
H	6.67431E+22
O	3.33738E+22
B	8.34184E+19

B.12 CASE 11: High Power (150% of Nominal) Depletion

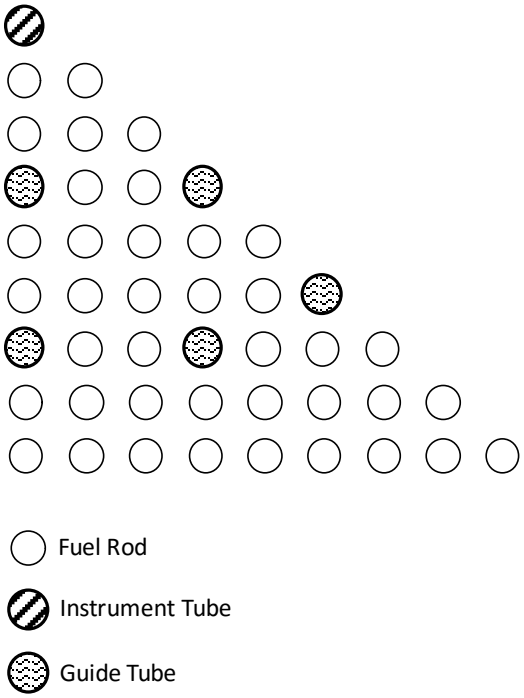

Fuel Rod

Instrument Tube

Guide Tube

Fuel Material Description

Material Density	10.340 (g/cm3)
Fuel Temperature	1072.5 K
Nuclide	**Number Density**
U-235	9.92536E+20
U-234	7.97571E+18
U-238	2.20709E+22
O	4.61429E+22

Coolant Description, Depletion

Boron Concentration	900 ppm
Temperature	592.5 K
Nuclide	**Number Density**
H	4.55525E+22
O	2.27778E+22
B	3.41601E+19

Appendix C: Reactivity Benchmark Specifications

Tables of experimental reactivity decrements for the 11 cases of Appendix B are presented in the following set of tables. The four sets represent cooling intervals of 0 hours, 100 hours, 5 years, and 15 years.

The definition of cold reactivity decrement as a function of lattice burnup, B, is defined as: $k_{inf}(B) - k_{ref}$, where k_{ref} is taken as $k_{inf}(B=0)$ for lattices without burnable absorbers. **Thus, $k_{inf}(B)$ for cases 5, 6, and 7 is computed with burnable absorbers still in the lattice**, while k_{ref} is taken from case 3 without burnable absorbers. This definition is used so that high-burnup reactivity decrement does not depend directly on the initial burnable absorber loading. This definition is consistent with reactor data used to generate the measured decrement biases – which include burnable absorbers. Since k_{ref} does not include burnable absorbers, the reported reactivity decrements include the combined reactivity change of both fuel and burnable absorbers. At high burnup, the reactivity of the burnable absorber approaches zero, and the reactivity decrement is dominated by the change in reactivity of the fuel.

The assigned uncertainties are independent of benchmark case (except for the high fuel temperature case), and uncertainties are displayed for each of the eleven Benchmark Cases in Table C-1.

The data used in this report are taken directly from a proprietary Studsvik report bearing the same title (report number, **SSP-11/409-C Rev. 0)** for which all work has been performed under the approved Studsvik QA Programs. If subsequent applications of data contained in this report require quality assurance, the proprietary QA version of this report can be obtained directly from Studsvik Scandpower, Inc.

Table C-1
Reactivity Decrement 95/95 Tolerance Limits (in Δk)

Case	Sub-batch Burnup (GWd/T)					
	10	20	30	40	50	60
1	0.00348	0.00537	0.00654	0.00752	0.00831	0.00888
2	0.00348	0.00537	0.00654	0.00752	0.00831	0.00888
3	0.00348	0.00537	0.00654	0.00752	0.00831	0.00888
4	0.00348	0.00537	0.00654	0.00752	0.00831	0.00888
5	0.00348	0.00537	0.00654	0.00752	0.00831	0.00888
6	0.00348	0.00537	0.00654	0.00752	0.00831	0.00888
7	0.00348	0.00537	0.00654	0.00752	0.00831	0.00888
8	0.00348	0.00537	0.00654	0.00752	0.00831	0.00888
9	0.00348	0.00537	0.00654	0.00752	0.00831	0.00888
10	0.00348	0.00537	0.00654	0.00752	0.00831	0.00888
11	0.00385	0.00563	0.00670	0.00766	0.00851	0.00917

Note that the WABA burnable absorbers are not removed in these calculations.

C.1 Burnup Reactivity Decrements: Cold, No Cooling

Table C-2
Measured Reactivity Decrement – No Cooling (in Δk)

Case	Sub-batch Burnup (GWd/T)					
	10	20	30	40	50	60
1	-0.1774	-0.2749	-0.3586	-0.4306	-0.4889	-0.5330
2	-0.1601	-0.2452	-0.3215	-0.3935	-0.4613	-0.5230
3	-0.1678	-0.2584	-0.3390	-0.4134	-0.4804	-0.5377
4	-0.1672	-0.2610	-0.3477	-0.4304	-0.5066	-0.5720
5	-0.2457	-0.2752	-0.3397	-0.4095	-0.4735	-0.5285
6	-0.2160	-0.2638	-0.3368	-0.4104	-0.4778	-0.5358
7	-0.2906	-0.2829	-0.3380	-0.4065	-0.4707	-0.5263
8	-0.1679	-0.2564	-0.3340	-0.4048	-0.4681	-0.5221
9	-0.1693	-0.2597	-0.3395	-0.4129	-0.4788	-0.5350
10	-0.1284	-0.2077	-0.2800	-0.3470	-0.4069	-0.4573
11	-0.1745	-0.2626	-0.3389	-0.4082	-0.4698	-0.5224

C.2 Burnup Reactivity Decrements: Cold, 100-hour Cooling

Table C-3
Measured Reactivity Decrement – 100-Hour Cooling (in Δk)

Case	Sub-batch Burnup (GWd/T)					
	10	20	30	40	50	60
1	-0.1324	-0.2334	-0.3208	-0.3960	-0.4570	-0.5032
2	-0.1141	-0.2016	-0.2803	-0.3549	-0.4254	-0.4897
3	-0.1218	-0.2152	-0.2987	-0.3762	-0.4461	-0.5059
4	-0.1202	-0.2171	-0.3072	-0.3935	-0.4731	-0.5415
5	-0.2040	-0.2330	-0.2995	-0.3721	-0.4388	-0.4962
6	-0.1731	-0.2210	-0.2965	-0.3730	-0.4434	-0.5039
7	-0.2519	-0.2413	-0.2978	-0.3690	-0.4359	-0.4940
8	-0.1211	-0.2124	-0.2929	-0.3666	-0.4326	-0.4890
9	-0.1232	-0.2166	-0.2995	-0.3760	-0.4448	-0.5035
10	-0.0962	-0.1779	-0.2527	-0.3221	-0.3842	-0.4365
11	-0.1230	-0.2144	-0.2942	-0.3668	-0.4315	-0.4868

C.3 Burnup Reactivity Decrements: Cold, 5-Year Cooling

Table C-4
Measured Reactivity Decrement – 5-Year Cooling (in Δk)

Case	Sub-batch Burnup (GWd/T)					
	10	20	30	40	50	60
1	-0.1365	-0.2466	-0.3444	-0.4288	-0.4967	-0.5475
2	-0.1158	-0.2081	-0.2940	-0.3765	-0.4545	-0.5252
3	-0.1242	-0.2240	-0.3161	-0.4022	-0.4797	-0.5455
4	-0.1227	-0.2258	-0.3247	-0.4201	-0.5079	-0.5827
5	-0.2064	-0.2419	-0.3168	-0.3978	-0.4719	-0.5351
6	-0.1755	-0.2299	-0.3137	-0.3988	-0.4767	-0.5433
7	-0.2542	-0.2502	-0.3151	-0.3945	-0.4688	-0.5326
8	-0.1236	-0.2213	-0.3103	-0.3926	-0.4661	-0.5284
9	-0.1256	-0.2252	-0.3165	-0.4013	-0.4775	-0.5420
10	-0.0981	-0.1853	-0.2672	-0.3434	-0.4112	-0.4677
11	-0.1263	-0.2240	-0.3122	-0.3932	-0.4652	-0.5262

C.4 Burnup Reactivity Decrements: Cold, 15-Year Cooling

Table C-5
Measured Reactivity Decrement – 15-Year Cooling (in Δk)

Case	Sub-batch Burnup (GWd/T)					
	10	20	30	40	50	60
1	-0.1417	-0.2650	-0.3765	-0.4724	-0.5487	-0.6051
2	-0.1179	-0.2179	-0.3137	-0.4062	-0.4934	-0.5720
3	-0.1272	-0.2367	-0.3402	-0.4373	-0.5242	-0.5972
4	-0.1255	-0.2380	-0.3485	-0.4555	-0.5532	-0.6355
5	-0.2097	-0.2550	-0.3412	-0.4329	-0.5161	-0.5863
6	-0.1787	-0.2427	-0.3379	-0.4338	-0.5210	-0.5947
7	-0.2576	-0.2634	-0.3395	-0.4295	-0.5127	-0.5836
8	-0.1268	-0.2343	-0.3348	-0.4280	-0.5108	-0.5803
9	-0.1286	-0.2379	-0.3405	-0.4361	-0.5214	-0.5930
10	-0.1009	-0.1966	-0.2882	-0.3733	-0.4484	-0.5104
11	-0.1295	-0.2372	-0.3370	-0.4288	-0.5100	-0.5782

Export Control Restrictions

Access to and use of EPRI Intellectual Property is granted with the specific understanding and requirement that responsibility for ensuring full compliance with all applicable U.S. and foreign export laws and regulations is being undertaken by you and your company. This includes an obligation to ensure that any individual receiving access hereunder who is not a U.S. citizen or permanent U.S. resident is permitted access under applicable U.S. and foreign export laws and regulations. In the event you are uncertain whether you or your company may lawfully obtain access to this EPRI Intellectual Property, you acknowledge that it is your obligation to consult with your company's legal counsel to determine whether this access is lawful. Although EPRI may make available on a case-by-case basis an informal assessment of the applicable U.S. export classification for specific EPRI Intellectual Property, you and your company acknowledge that this assessment is solely for informational purposes and not for reliance purposes. You and your company acknowledge that it is still the obligation of you and your company to make your own assessment of the applicable U.S. export classification and ensure compliance accordingly. You and your company understand and acknowledge your obligations to make a prompt report to EPRI and the appropriate authorities regarding any access to or use of EPRI Intellectual Property hereunder that may be in violation of applicable U.S. or foreign export laws or regulations.

The Electric Power Research Institute, Inc. (EPRI, www.epri.com) conducts research and development relating to the generation, delivery and use of electricity for the benefit of the public. An independent, nonprofit organization, EPRI brings together its scientists and engineers as well as experts from academia and industry to help address challenges in electricity, including reliability, efficiency, affordability, health, safety and the environment. EPRI members represent 90% of the electric utility revenue in the United States with international participation in 35 countries. EPRI's principal offices and laboratories are located in Palo Alto, Calif.; Charlotte, N.C.; Knoxville, Tenn.; and Lenox, Mass.

Together...Shaping the Future of Electricity

Program:

Used Fuel and High-Level Waste Management

3002010613

Electric Power Research Institute
3420 Hillview Avenue, Palo Alto, California 94304-1338 • PO Box 10412, Palo Alto, California 94303-0813 USA
800.313.3774 • 650.855.2121 • askepri@epri.com • www.epri.com